8-2018

Computer Modeling of Close-to-Ground Tornado Wind-Fields for Different Tornado Widths

Mohammadhossein Kashefizadeh
University of Arkansas, Fayetteville

Computer Modeling of Close-to-Ground Tornado Wind-Fields for Different Tornado Widths

A thesis submitted in partial fulfillment
of the requirements for the degree of
Master of Science in Civil Engineering

by

Mohammad Hossein Kashefizadeh
Iran Azad University
Bachelor of Science in Civil Engineering, 2010
UTM University of Malaysia
Master of Science in Civil Engineering, 2012

August 2018
University of Arkansas

This thesis is approved for recommendation to the Graduate Council.

R. Panneer Selvam, Ph. D
Thesis Director

Ernie Heymsfield, Ph. D
Committee Member

W. Micah Hale, Ph. D.
Committee Member

ABSTRACT

Tornadoes induce different wind forces on buildings than straight-line (SL) winds. The tangential velocity (V_θ) of tornados is the main parameter that causes damage to the buildings. In-field tornado measurements cannot evaluate the tornado's V_θ at less than 20m above ground level (AGL). The laboratory tornado simulators suggest that the Swirl ratio (S) and the radius (r_o) are the most influential factors affecting V_θ. However, due to scaling problems, laboratory simulators cannot report the V_θ for elevations less than 10m AGL. Well refined computational fluid dynamics (CFD) models can evaluate the V_θ at less than 10m AGL. However, the CFD models are limited to tornado radius r_o=1.0km whereas observation of actual tornados by National Weather Service (NWS) shows that significant tornados in USA have width in the range of 0.7km to 2.3km. Thus, effect of r_o on the V_θ is not investigated. Therefore, the aim of this study is to investigate the maximum V_θ ($V_{\theta,max}$) for different tornado radii at elevations above and below 10m AGL. Simulation results show that by increasing the r_o, the S parameter producing the $V_{\theta,max}$ will increase accordingly. In addition, results show that by increasing r_o, the $V_{\theta,max}$ gradually reduces with respect to reference radial velocity $V_{r\infty}$. In this respect, for 0.7km$\leq r_o \leq$2.3km the $V_{\theta,max}$ is in the range of 6.5$V_{r\infty}$ to 3.0$V_{r\infty}$. Moreover, by increasing r_o, the elevation of occurrence (z_{max}) of the $V_{\theta,max}$ will increase; However for all tornado radii, the z_{max} is always between 21m to 64m AGL. In addition, simulations show that for $r_o\leq$1.6km the radial V_θ profiles above 10m of the ground resemble the Rankine Combined Vortex Model (RCVM) flows, whereas at less than 10m of the ground the profile has two peaks for S greater than the touchdown S. Similarly, for $r_o\geq$1.8km the radial V_θ profiles below and above z=10m have two peaks for the S greater than the touchdown S.

ACKNOWLEDGEMENTS

Special thanks are extended to my advisor Dr. R. Selvam for his unconditional support, time and guidance during this work. I am thankful for the opportunity he gave me to work on the project upon to use his tornado modeling program and his training on Tecplot software. Besides my advisor, I would like to thank the rest of my thesis committee members: Dr. Heymsfield and Dr. Hale, for their insightful comments and encouragement.

My sincere thanks also go to Dr. Selvam's research group, including Dr. Majdi Yousef, Damaso Dominguez, and Myles Lacy, who wholeheartedly assisted me in reviewing my work. Also, special thanks to the faculty and staff member at the Civil engineering department of the University of Arkansas for their commitment to students.

I would also like to thank to my father, mother, brother and sister who always supported and encouraged me.

TABLE OF CONTENTS

LIST OF TABLES

LIST OF FIGURES

NOMENCLATURE

Latin symbols	Description
ABL	Atmospheric boundary layer
AGL	Above ground level
AR	Aspect ratio
CFD	Computational fluid dynamics
CFL condition	Courant-Friedrich- Lewy condition
EF	Enhance Fujita
FDM	Finite difference method
FEM	Finite element method
FVM	Finite Volume Method
GBVTD	Ground-Based Velocity Track Display
H_o	Height of the inlet
h	total height of the computational domain equal to $2H_o$
LES	Large Eddy Simulation
MGS	Minimum grid spacing
NS	Navier-Stokes
RCVM	Rankine Combined Vortex Model

RANS	Reynolds Averaged Navier-Stokes equations
R_e	Reynolds Number
S	Swirl ratio
SL	Straight Line
SOLA	Solution Algorithm technique
Tang.	Tangential
P	The ratio of pressure to constant density (normalized with density)
r_o	Updraft radius of the computational domain
r_c	Core radius, the radius at which maximum tangential velocity occurs (The horizontal distance from the tornado center to the peak V_θ)
V_r, V_θ, V_z	Velocity components in the *r* direction (radial), direction (tangential) and *z* direction (vertical) in cylindrical coordinate system
$V_{\theta,max}$	Maximum tangential velocity
Vtang.	Tangential velocity
WT	Wind tunnel
z_o	Reference height
z	Height
z_{max}	Elevation of occurrence of the $V_{\theta,max}$

Greek symbols

r, θ, z	The cylindrical coordinates
ν	Coefficient of the kinematic viscosity
ν_{sgs}	Sub-grid scale eddy viscosity
ν_{eff}	$= \nu + \nu_{sgs}$
y	distance from the wall
V_r(y)	Velocity at distance *y* from the wall
τ_w	shear stress
ρ	fluid density

CHAPTER 1. INTRODUCTION AND OBJECTIVES

The United States experiences a higher number of annual tornados than all other countries. An average of 1200 tornados occur within the USA each year killing up to 60 people and injuring more than 1500 people. Additionally, tornados cause $148 million building damages to the United Sates annually, and are the second largest cause of damage after hurricane in this country (NWS, 2010). A major reason for the continued devastations by tornados is an inadequate understanding of this type of wind storm and its loading on structures.

1.1. Tornado forces on buildings

The force that tornados exert on buildings is different from straight line (SL) atmospheric boundary layer (ABL) flows. Jischke and Light (1979 & 1983), Bienkiewicz and Dudhia (1993), Selvam and Millet (2003), Mishra et al. (2005), Zhao et al. (2016) and Yousef (2017) reported the mean surface pressures due to tornado to be in the range of 2.5-5 times higher than the SL flows. Likewise, the tornado-induced lateral and vertical forces on structures are, respectively, 1.5 times and 3 times higher than those by ASCE 7-05 (Sarkar et al. 2006; Hann et al. 2008; Haan et al. 2010; Hu, 2011). Therefore, a properly designed structure for the SL boundary layer flow might fail for a tornado-wind of the same speed (Selvam and Millett, 2003), and thus the existing building codes and provisions fail in predicting tornadic wind loads.

1.2. Difference between the SL and tornadic winds and forces

Figure 1.1 shows SL and tornadic flows. It can be seen in this figure that SL flow behavior is directly proportional to height, and translates across the isobars (Figure 1.1.a). On the other hand, a tornado is a narrow, violently rotating column of air that produces vortices with significant tangential velocity components (Figure 1.1.b). In a SL wind, wind flows in one direction as shown in Figure 1.1.a; whereas a tornadic flow has three velocity components: radial velocity (V_r), tangential velocity (V_θ), and vertical velocity (V_z). Out of these three components, V_θ is more intense than V_r and V_z (Church, 1979; Ishihara and Liu, 2014, Vatistas, 1998). Therefore, in order to design the buildings for tornados, the maximum V_θ ($V_{\theta,max}$) of the tornados should be investigated.

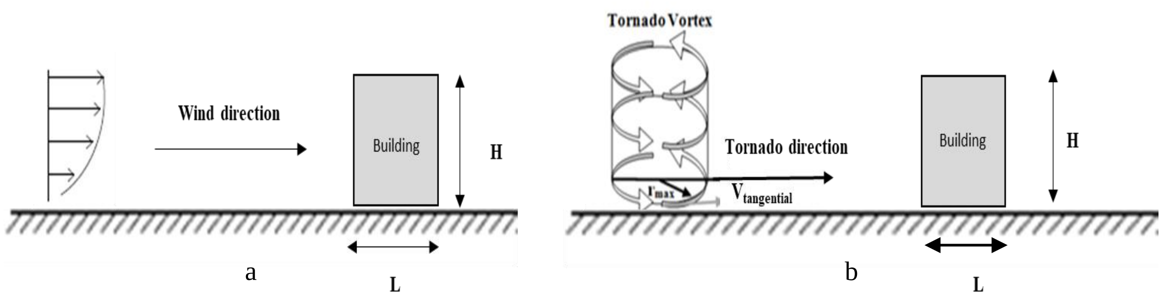

Figure 1.1. Main velocity components for: a) SL boundary layer wind; b) tornado wind

1.3. Importance of $V_{\theta,max}$ and computer modeling of tornados

The V_θ profile in the field can be obtained from Doppler radar measurements. Refan et al. (2017) analyzed five different tornado data and reported their $V_{\theta,max}$. One of the drawbacks of the Model of Refan et al. (2017) is that they can only provide the V_θ profile above 30m above ground level (AGL) due to the blocked reflection close to ground (Doswell et al. 2009; Wurman and Kosiba, 2013). On the other hand, wind engineers are interested in wind profiles close the ground for the following reasons: first, most buildings are within 10m from the ground; second, several studies show that the $V_{\theta,max}$ occurs close to the ground.

In order to understand further details of the V_θ, laboratory tornado vortex chambers (TVCs) are used (Ward, 1972). The V_θ in the laboratory TVCs is influenced by the following parameters (Maxworthy,1972; Davies-Jones, 1973): Reynolds number (R_e), the aspect ratio (AR), and swirl ratio (S), as given below:

$$R_e = \frac{(V_{r\infty})(Inlet\ height)}{\nu} \quad \text{Eq. (1.1)}$$

Where $V_{r\infty}$ is the radial velocity of the tornado and ν is the kinematic viscosity of air. Using Re≥4.5x104 in the TVC models make the tornado simulations independent of the R_e as reported by Refan and Hangan (2017).

$$AR = \frac{H_o}{r_o}; \quad \text{Eq. (1.2)}$$

where r_o=0.5*width of the tornado, and is the radius of TVC, and H_o is the inflow height. Also,

$$S = \frac{V_\theta}{2(AR)V_r} = \frac{V_\theta}{2(\frac{H_o}{r_o})V_{r\infty}}; \quad \text{Eq. (1.3)}$$

Eq (1.3) implies that S and r_o influence V_θ. Figure 1.2 shows these TVC parameters.

However, the relatively small size of the laboratory simulators results in large geometric scaling ratios (Refan and Hangan, 2017), thus they cannot evaluate the close-to-ground V_θ. In this regard, Refan (2014) proposed a simulator with scale of 1:11, but this model cannot measure V_θ at less than 35m AGL. Therefore, the laboratory simulators are incapable of measuring the close-to-ground V_θ. To solve this problem, computer models can be used. For particular r_o or S parameters, extensive studies using computational fluid dynamics (CFD) simulation models are conducted. CFD models of Rotunno (1977), Lewellen et al. (1997, 1999), Kuai et al. (2008) and Gallus et al. (2006) are limited to the minimum elevation of 20m AGL. The CFD model of Dominguez and Selvam (2017) was able to evaluate the V_θ at less than 10m AGL, but the radius was limited to r_o=1.0km in their study. However, observations of actual tornados by National Weather Service (NWS) shows that significant tornados in USA have radii in the range of 0.7km to 3.2km. Therefore, in the CFD models, the effect of r_o on the $V_{\theta,max}$ is not investigated so far and the computer modeling should be further investigated for different tornado r_o radii.

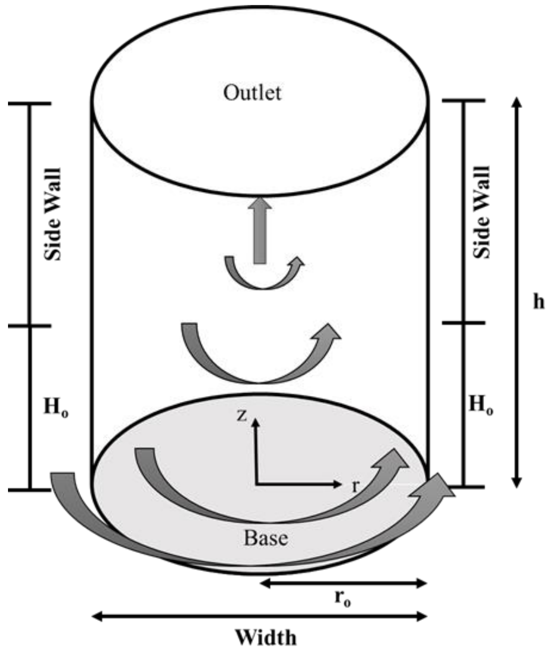

Figure 1.2. Schematic of a TVC and its parameters

1.4. Aim and objectives of the study

Dominguez and Selvam (2017) proposed a CFD model to simulate a tornado chamber of 1.0kmx2.0km. They used minimum grid spacing (MGS) of 0.001H_o in the vertical axis, where H_o=1000m; rendering that their model captured the spacing of 1.0m close to the ground. However, their model is limited to the tornado radius of r_o=1.0km, and the V_θ profile for other tornado radii are not investigated. Therefore, the present study will propose a CFD model to determine the $V_{\theta,max}$ for various r_o radii above and below 10m AGL. Based on these, the objectives of the study are formulated as follows:

Objective 1: To investigate the effect of the tornado radii on the $V_{\theta,max}$

Lewellen et al. (1999) postulated that by changing r_o parameter the $V_{\theta,max}$ will change. Dominguez and Selvam (2017) used a CFD model and reported that for r_o=1km the $V_{\theta,max}$ is approximately 5.0$V_{r\infty}$ which occurs at elevation (z_{max}) of 28m AGL with S=0.6; however other tornado radii were not investigated in their study. Hangan and Kim (2008) stated that by changing the r_o the S parameter producing the $V_{\theta,max}$ will change, but they did not report the S value for different r_o radii. Therefore, as the first objective of this study, the S parameter producing $V_{\theta,max}$ are determined for 0.7km≤r_o≤2.3km, which is the range of common tornados in the USA as reported by NWS. In addition, the r_c and z_{max} for 0.7km≤r_o≤2.3km are investigated.

Objective 2: To investigate the $V_{\theta,max}$ below 10m AGL for different r_o radii

Although the V_θ close to the ground is the major cause of building damages, the laboratory and CFD models cannot report the V_θ at less than 10m AGL (Dominguez and Selvam, 2017), whereas typical buildings are located at z=3.3m AGL. Dominguez and Selvam (2017) reported the $V_{\theta,max}$ a z=3.3m AGL for r_o=1.0km. Thus, the present study will investigate the $V_{\theta,max}$ for 0.7km≤r_o≤2.3km at z=3.3m AGL.

Objective 3: To investigate the effect of r_o on the V_θ profile close to the ground

Previous studies show that the V_θ profile of tornados at different elevations resemble the Rankine Combined Vortex Model (RCVM) flow. However, Dominguez and Selvam (2017) showed that for r_o=1.0km the radial V_θ profile at z<10m has two peaks and no longer resembles the RCVM profile. Church et al. (1979) asserted that occurrence of two peaks on the radial V_θ profile close to the ground is due to a strong shear force and is the main cause of destructive effect of tornados on buildings. Therefore, as the third objective of this study, the radial V_θ profiles of different tornados with 0.7km≤r_o≤2.3km at different elevations are investigated.

CHAPTER 2. LITERATURE REVIEW

The main goal of this literature review is to conduct a comprehensive analysis of the current state of knowledge on the tornado flows. The literature review begins with a brief review of the basic information about tornados. Afterward, the techniques of measuring the tornados' velocity and intensity are discussed. Then, the in-field and the post-damage investigation techniques are reviewed. Subsequently, techniques of modeling the tornados, including the analytical, laboratory and CFD models are also presented and their pros and cons are discussed.

2.1. Tornado as an atmospheric phenomenon

A tornado is a high-speed short-term rotating storm. This phenomenon can have a maximum velocity of 300 mph, and its damage paths can be in excess of 4.5km and 80km long. Tornados rotate counter-clockwise in the Northern Hemisphere and clockwise in the Southern Hemisphere. This phenomenon is visible as a vortex which rotates about a hollow cavity as a whirlpool structure of winds which produce centrifugal forces. As condensation occurs around the vortex, a pale cloud appears and tornado funnel becomes visible. Funnels usually appear as an extension of the dark, heavy cumulonimbus clouds of thunderstorms, and stretch downward toward the ground (Huschke, 1959). However, some of these funnels never touch the ground, and some of them touch and rise again. Genesis of the tornado and its structure are discussed in the following sections.

2.2. Tornado genesis and formation

Allaby (1997) stated that tornadoes are produced by the combined effects of thermal and mechanical forces, with one or the other force being the stronger generating agent. NOAA (2010) stated the reason of the tornado genesis in the USA is interaction of the warm moist Gulf air with the cold and dry Canadian air coming via the Rockies.

Figure 2.1 shows the process of genesis of the tornado as presented by NOAA (2010). It can be seen that before the process of tornado genesis has three stages. In the first stage, thunderstorms develop, a change in the wind direction and an increase in the wind speed with the height happens which causes an invisible horizontal spinning effect in the lower atmosphere. In the second stage, the rising air within the thunderstorm updraft tilts the rotating air from horizontal to vertical. In the third stage, an area of rotation extends through the storm body. Most tornados form within this area of strong rotation.

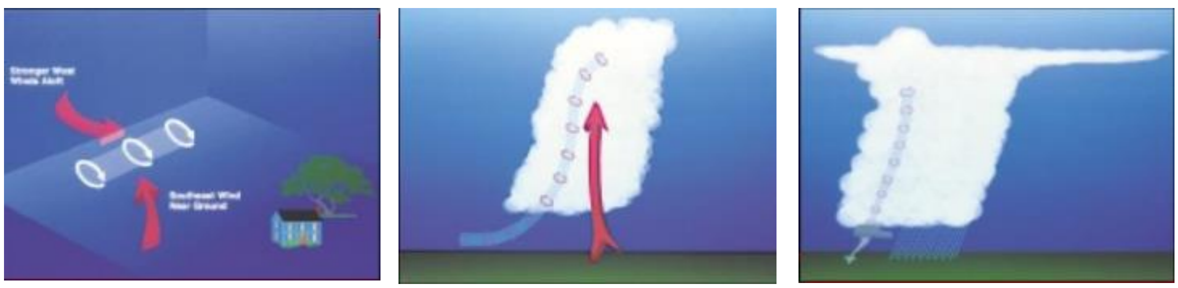

a b c

Figure 2.1. Tornado genesis and formation (NWA, 2010). a) Stage one; b) Stage 2; c) Stage 3

2.3. Tornado structure

Structure of tornados can be studied from two perspectives: the general structure which shows its different regions, and the vertical structure, which shows the number of its cells.

2.3.1. General structure of tornados

Figure 2.2a depicts the main features of the tornado as defined by Whipple (1982). As can be seen in Figure 2.2, a rotating funnel cloud is in contact with both the ground and the wall cloud. The rate of the circulation is decreasing away from the tornado vortex core, and a characteristic air suction is observed inside the vortex.

Wurman et al. (1996) provided more precise representation of the structure of the tornado, as shown in Figure 2.2b. They analyzed the data obtained from the Doppler Radar for a real tornado and distinguished five different flow regions, as shown in Figure 2.2b. In their model, Region I is the outer-flow region, which is above the boundary layer region and extends at least 1km above the vortex core. Region II represents the core of the tornado. This region is associated with high wind velocities and a pressure drop. Region III can be described as a tip of Region II. There, the tornado flow is intensified and disturbed by frictional interaction with the surface. Around Region III, there is the surface boundary layer region (Region IV), and in Region V the angular momentum of the vortex is concentrated and transported downward.

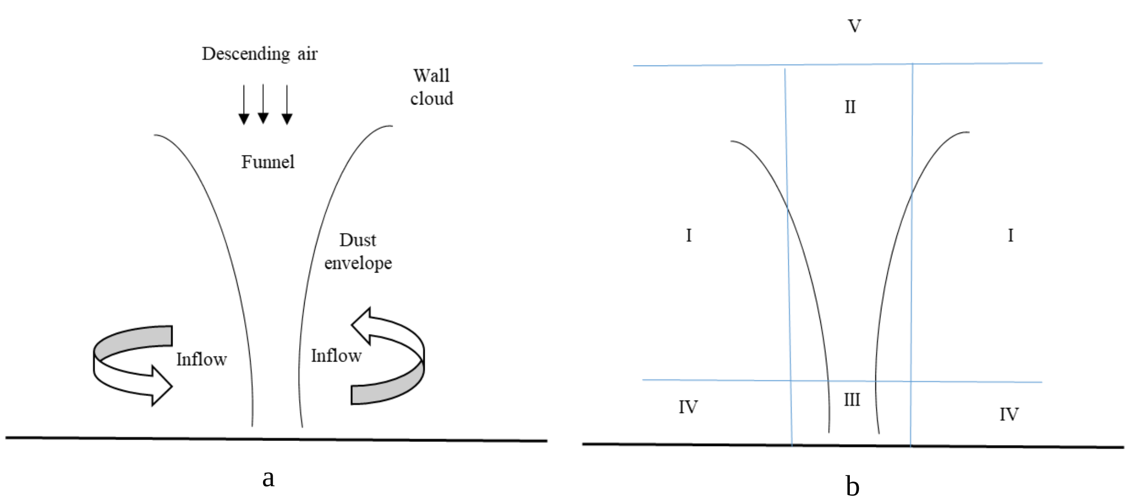

Figure 2.2. a) Structure of tornado vortex. a. Model of Whipple (1982); b) Tornado vortex with distinguished various flow regions (Wurman, Straka and Rasmussen, 1996).

2.3.2. Vertical structure of tornados

Lewellen (1976) and Davies-Jones (1986) stated that with increasing the S parameter of the tornado models, the tornado vortex evolves from a jet-like flow to a one-cell vortex which is characterized by an axial up-flow in the centerline (Figure 2.3.a). Afterwards, stagnation point and vortex breakdown occur aloft (Figure 2.3.b)., and double-cell tornado occurs, which is characterized by apparent downdraft in the center of the tornado (Figure 2.3.c). Occurrence of double-cell tornado is the stage at which the $V_{\theta,max}$ occurs. Refan (2014) and Refan et al. (2014) also suggested the same structures for the single- and double-celled tornados.

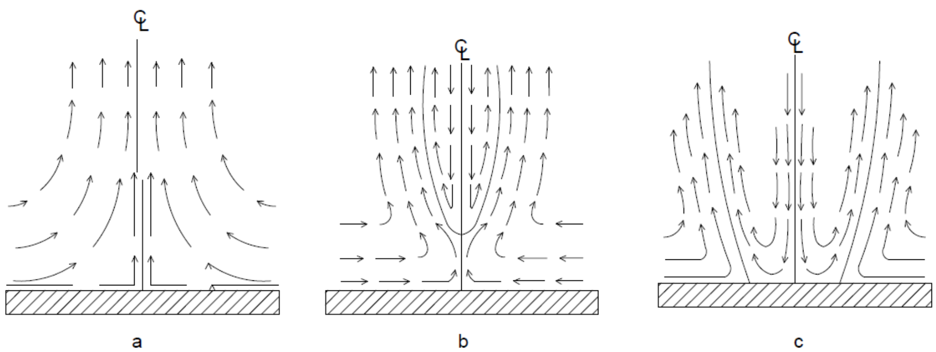

Figure 2.3. a) Vertical structure of single-cell; b) Vortex breakdown aloft; c) Vertical structure of the double-cell (Davies-Jones, 1986)

2.4. Size, speed and duration of tornados

As an NWS report in 2012 defines, the tornados can be categorized as weak, strong and violent tornados as shown in Table 2.1. However, their classification does not provide information on the tornado damages to the buildings, Therefore, researchers turned their attention to connecting the tornado speed to the damages they cause to the buildings.

Table 2.1. Tornado severity report (NWS, 2012)

Tornado severity	Weak tornado	Strong tornado	Violent tornado
Frequency (%)	88	11	1
Death ratio(%)	Less than 5	Almost 30	70
Lifetime (minute)	1-10	>20	>60
Speed (mph)	<110	10-205	>205

2.5. Tornado intensity classification

Intensity of the tornados and the damage they cause to the buildings is classified by methods Fujita and Enhance Fujita (EF) scales. These scales are explained by detail in this section.

2.5.1. Fujita intensity scale

The most important parameter to classify the tornado intensification and its damage to the buildings is its wind speed (Fujita, 1971). Thus, Fujita (1971) proposed a statistical method to scale a tornado intensity using the tornado velocity. He related the maximum tornado wind velocity to the intensity based on the observed damage investigations. However, the velocities in Fujita Scale are greatly overestimated (Grazulis, 1993). Therefore, attempts were made to modify the Fujita scale (McDonald, Forbes and Marshall, 2004).

2.5.2. Enhanced Fujita (EF) intensity Scale

In 2004, the Fujita intensity scale was modified in Texas Tech University (McDonald, Forbes and Marshall, 2004), and was named as EF scale. The EF scale provides a better correlation between the tornado damage and its maximum wind speed (NOAA, 2012). A comparison of the F and EF intensity scales is shown in Table 2.2.

Table 2.5. Comparison of Fujita (F) and Enhance Fujita (EF) intensity scales

Fujita Scale (F)	3-sceond gust speed (km/h)	Enhance Fujita Scale(EF)	3-sceond gust speed (km/h)
F0	73-127	EF0	105-138
F1	128-190	EF1	139-177
F2	191-261	EF2	178-222
F3	262-339	EF3	223-271
F4	340-424	EF4	272-323
F5	425-514	EF5	324-380

2.6. Frequency occurrence and the death rate of tornados

NOAA (2012) classified the death-related statistics of the tornados of 1950 to 2012 based on F-scale. They related the percentage of the number of the deaths due to each Fujita scale tornado is shown in Figure 2.4. NOAA (2012) reported that among 1704 tornados in 2011, only 5% of them fall in the category of EF3 to EF5, whereas 95% of tornados fall in the categories of EF0 to EF2. This figure implies the importance of providing a better design for the highly intense tornados, and for this purpose, the tornado wind profile should be investigated first. Hence, the next section reviews studies of the wind velocity profile.

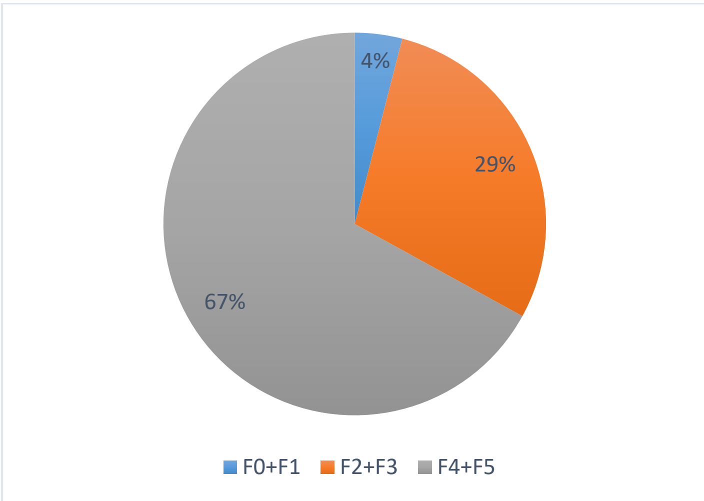

Figure 2.4. Percentage of the tornado-related deaths by Fujita scale from 1950 to 2011

2.7. Investigation of the wind velocity profiles

Studies pertaining to the wind velocity of tornados can be categorized as in-field measurements, and post-damage investigations. Each of these techniques has its own subclasses which are discussed in the following sections.

2.7.1. In-field measurements

2.7.1.1. Doppler radar measurements

The spatial distributions of Doppler velocities can be used to study special characteristics of tornadoes (Doviak and Zrnic,1993; Wuman et al. 1997). The mechanism of Doppler radar to measure the tornado parameters is straightforward. The radar initially quantifies only the wind toward and away from the radar. Afterwards, the radar measurements will be connected to Doppler spectra of tornadoes by showing a model of tornado circulation. Since using Doppler radars facilitates data collection of the tornado-induced damages (Wuman et al. 1997), different configurations of the Doppler radars have been used to collect the data of over 200 individual tornados (Wurman, 1997; Lee and Wurman, 2005; Wurman, 2002; Kosiba, Trappa and Wurman, 2008; Wakimoto et al., 2012; Wurman et al., 2013).

Using Doppler Radar for tornados revealed that the V_θ profile is similar to the Rankine model profile. The Rankine profile is often called Rankine Combined Vortex Model (RCVM) (Kilty, 2005). In the RCVM, the flow has two separate flow fields. In the interior flow field (inner core), the V_θ increases linearly with the radius, and peaks at a point which is called core radius (r_c). In the outer flow (tail), the V_θ declines inversely with radius from the r_c outward. The RCVM profile of Mulhall tornado is shown in Figure 2.5.

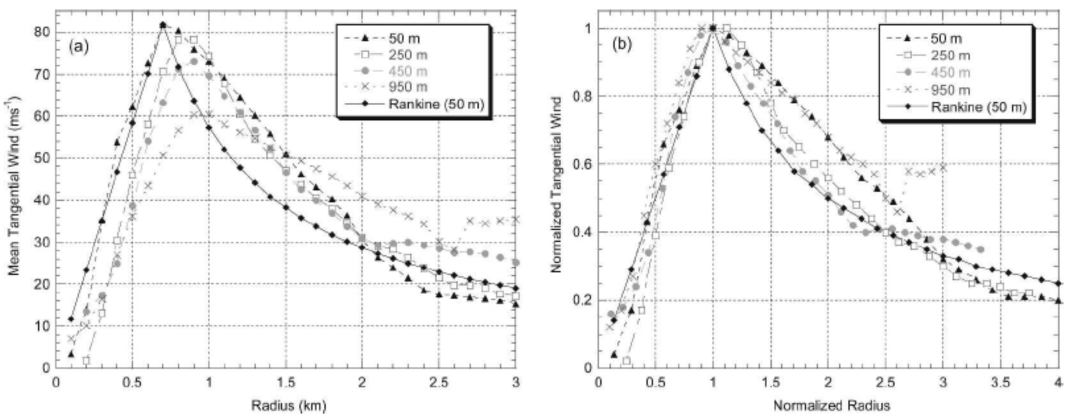

Figure 2.5. Rankine Model profile of an actual tornado (Taken form Lee and Wurman, 2005)

Likewise, Wurman and Alexander (2005) and Kosiba, Trappa and Wurman (2008) compared the observed tornado damage with retrieved Doppler Radar data, interpolated velocity fields and compared them with F-scale estimates. Their comparison revealed that radar-based estimates of the F-scale intensity usually exceeded the damage-survey-based F-scale. Table 2.3 presents a summary of some of the tornados that were investigated by Doppler Radar technique. Table 2.3 shows the Doppler radar measurements determine the $V_{\theta,max}$ at elevations above 50m.

Although the Doppler radar technique offered valuable insight of the tornado velocity profile and tornado structure, its measurements have some drawbacks. The most important drawback is that the Doppler Rada measurements is that they cannot evaluate the close-to-ground wind field, rather they are limited to about 50m from the ground (Wurman et al. 2007). This limit is due to the beam restrictions of the Doppler radars. In order to solve this problem, Wurman et al. (2003) used Doppler on Wheels for the Spencer tornado of 1998. However, they could not capture less than 30m AGL. Also, Wurman et al. (2013) used mobile Doppler radars and reported that the $V_{\theta,max}$ remains constant at less than 30m, which is in contrast to the reality (Lewellen et al., 2008; Wakimoto et al., 2012). Furthermore, the Doppler radar investigation is always associated with the injuries of the crew, and is thus unsafe (Wurman et al., 2014). Lastly, Doppler radar measurements suffer from the physical obstacles that exist in the field (Dominguez and Selvam, 2017).

Table 2.3. Doppler Radar measurements of some actual tornados

Tornado	Maximum $V_{r\infty}$ (m/s)	$V_{\theta,max}$ (m/s)	r_c (m)	z_{max}(m)
Mullhal, OK (1999)	NA	100	700	50
El Reno, OK (2013)	20	60	650	175
Bridge-Creek-Moore, OK (1999)	NA	126	175	50
Spencer, SD (1998)	30	101	700	50
Hong Kong (2004)	NA	22	30	~50

2.7.1.2. Ground-Based Velocity Track Display (GBVTD)

In order to rectify the drawbacks of the Doppler radar measurements, the mathematical technique of Ground-Based Velocity Track Display (GBVTD) is employed by some researchers. The GBVTD uses the data of the Doppler radar measurements to measure the $V_{r\infty}$ and V_θ close to the ground. The GBVTD analysis consists of four steps: filtering the raw radar data, transforming the data into a Cartesian grid, identifying the center of the vortex and retrieving tangential and radial velocity components through the algorithm. Refan et al. (2017) used this technique to determine the tornado features of five actual tornados: Spencer, SD 1998 (F4), Stockton, KS 2005 (F1), Clairemont, TX 2005 (F0), Happy, TX 2007 (EF0) and Goshen County, WY 2009 (EF2) Likewise, Kosiba and Wurman (2013, a, b) used this technique to determine the tornadic features of Russel, Ks 2014 and Happy TX tornados. A summary of the findings of the GBVTD is given in Table 2.4. However, Nolan (2013) claimed that the velocities obtained by the GBVTD are biased. Nolan (2013) showed that the close to ground V_θ profile of the GBVTDs is affected by the effect of the debris. This problem is more accentuated for smaller or weaker tornados.

Table 2.4. GBVTD analysis of some actual tornados

Tornado	Maximum $V_{r\infty}$ (m/s)	$V_{\theta,max}$ (m/s)	r_c(m)	z_{max}(m)	Reference
Spencer, SD (2003)	30	80	105	20	Hangan and Kim, (2008)
Mulhall, OK (1999)	NA	80	NA	50	Lee and Wurman, (2005)
Manchester, SD (2003)	~30	80	130	20	Gallus and Sarkar (2010)
Goshen, Wyoming (2009)	10	41	140	30	Wurman et al (2013)
Dimmit, Texas (1995)	50	60	150	Na	Wurman and Gill (2000)
Tuscaloosa, AL (2011)	76	43	Na	NA	Karstens and Gallus (2013)
El Reno, OK (2013)	20	Na	650	50	Bluestein et al., 2016
Moore, OK (2013)	50	80	NA	NA	Ortega et al. (2014)
Russel, Ks (2012)	NA	43	80	5.0	Kosiba and Wurman (2013)
Happy, TX (2002)	NA	36	160	NA	Refan et al. (2017)

2.7.2. Post-damage investigations

2.7.2.1. In-field post-damage investigation

Mehta et al. (1976) investigated the damage of the 1974, Canada tornado using in-field data collection by locating 148 damage survey spots and concluded that the appearance of the damage cannot be related to the wind speeds. They suggested that adoption of wind load criteria that focus on details of design materials can help reduce the damage to the buildings. Chmielewski et al. (2008) investigated the damage of a tornado occurred near Opole, Poland in 2008. In their study, they investigated the damages on the structures and found the velocity of the tornado. Likewise, Lewellen et al. (2008) assessed the effect of debris on tornados and concluded that the debris may affect tornadic flow near the surface. They also conclude that, as the damage track is the primary visual signature of tornadoes, realistic simulation of their path and width contributes to correlating the tornado structure to the measured velocities. Selvam et al. (2015) investigated the Mayflower Tornado of 2014 through in-field investigations. In their investigation, they considered the topography effect of the area interacting with the tornado.

However, the shortcoming of the in-field post-damage investigation is that they cannot provide any detail on the V_θ profiles, rather they only correlate the damages to the intensity scales.

2.7.2.2. Photography and video observations

Walter and Hoecker (1960) investigated the wind speed patterns of the 1957 Dallas Tornado. In their investigation, they used the movies taken by telephoto lenses from the tornado, and determined the path and wind speeds of the tornado. They reported the r_c equal to almost 60m, z_{max} equal to 90m, and the V_θ approximately 78m/s, respectively. However, this method was of limited applicability, because the movie-recording facilities were not available everywhere. Moller et al. (1974, 1979) investigated a tornado in Oklahoma by using the in-field photography after the occurrence of the tornado. Using the photography technique, they could provide an estimation of the tornado velocity.

However, several drawbacks are associated with this technique. The first shortcoming is that little could be understood from the in-field photography due to poor quality of the images. In addition, because of extreme limitations in the field, measurements of the tornado velocity were nearly impossible. So, it can be concluded that photography and video observations are an outdated technique for evaluating the velocity profile.

2.7.2.3. Satellite-based measurements

In this technique, the satellite images are used by surveyors in remote areas, from the ground, to either collect data of the tornado or correct the tornado track and differences given by other surveyors. The significance of the satellite based measurements is pronounced in large tornados and tornado outbreaks, where the in-field measurements such as Doppler radar are inefficient and cost-intensive.

The mechanism of the satellite imagery is that the satellite sensors measure reflected solar radiation in different spectral channels across the visible and infrared energy spectrum, and then recombine the spectral channels into an image and a natural color scene. In this way, these images can be used to detect variations in surface features associated with different land cover. The physical principle guiding the use of satellite data to detect tornado damage is based on the premise that the strong winds associated with a tornado will change the physical characteristics of the surface in such a way as to alter the visible and infrared energy reflected from the surface as measured by the satellite sensor. These characteristics could be a change in the orientation of surface features or a physical change in surface reflective properties or both.

Early applications of satellite imagery were to characterize or identify severe storm damages (Klimowski et al., 1998). Yuan et al. (2002) used Indian Remote Sensing (IRS) satellite data to examine the ground track of the 1999 Oklahoma City tornado, and found out that they can track F3 and greater regions on the Fujita scale (Fujita 1981, 1987). Strong and Zubrick (2004) used the data of the National Aeronautics and Space Administration (NASA) and the U.S. Geological Survey (USGS) on the La Plata, Maryland, tornado to relate the tornado velocity to the damage. NASA and USGS used very high spatial resolution research instruments to qualitatively map the damage track of the tornado.

Jedlovec et al. (2006) explored the possibility of using the image database of NASA Earth Observing System satellites to estimate tornado damage track length and width in order to study the tornado-related damages. They used Moderate Resolution Imaging Spectroradiometer

(MODIS) and Advanced Space-borne Thermal Emission and Reflection Radiometer (ASTER) data to study the damage tracks of three tornados. It was found that, depending on the nature of the land cover, tornado damage tracks from intense tornados (F1 or greater) may be evident in the satellites. However, in the forest-covered area the scar patterns are visible while in the grassland regions, scar patterns cannot be seen at all in these satellite imageries.

Molthan et al. (2011) investigated the damage track of Alabama tornado outbreak using NASA satellite imageries. Lengths and widths of satellite-based tornado tracks were compared against official survey measurements, and it was observed that the widths obtained using NASA images are considerably less than that of the NWS. In addition, Molthan et al. (2014) concluded that it is likely the satellite-based estimates of maximum width failed to detect damage in the EF0 to EF2 range that occurred along the periphery of the surveyed tracks.

Selvam and Ahmed (2013) used the Google Earth aerial imagery data for damage investigation of terrain effects on tornado damage. Selvam et al. (2015) investigated the Mayflower Tornado of 2014 by incorporating the in-field investigations with Aerial photography from the Civil Air Patrol (CAP), NASA satellite images, and Google Earth images. Dominguez and Selvam (2016, 2017) also employed the same technique to measure the maximum width and the translating velocity of Mayflower and Tuscaloosa tornados. An example of using satellite imagery data to measure the tornado parameters in shown in Figure 2.6.

Despite their growing application, the satellite-based measurements are limited to only reporting the width and the translational velocity of the tornados, and the evaluation of the V_θ velocity profile is impossible in this technique.

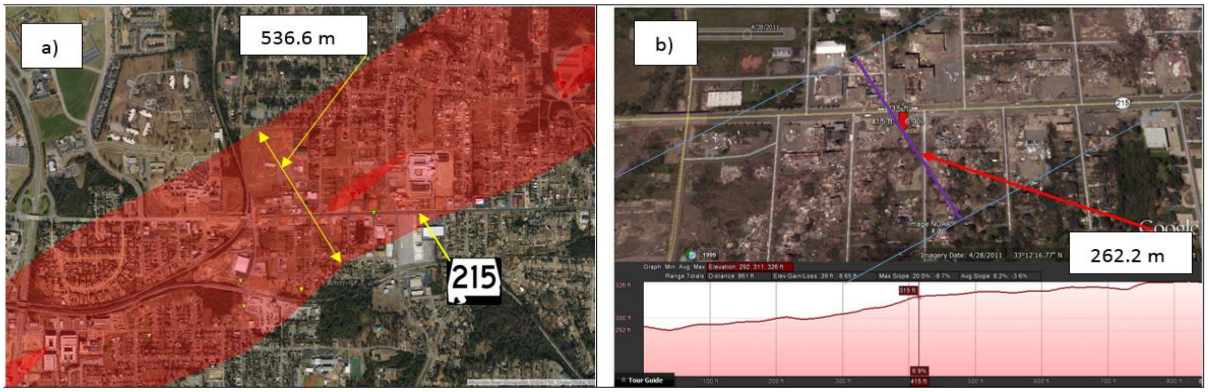

Figure 2.6. Satellite imagery measurement of a tornado using Google Map Imagery data (Dominguez and Selvam, 2017)

2.7.2.4. Post-damage investigation of the National Weather Service (NWS)

In this technique, researchers measure the tornado distance by either walking through the damage line or by using a vehicle trip (Clarke and Clarke, 2015). In large-scale tornados where these methods cannot be employed efficiently, online mapping using tools such as Damage Assessment Toolkit (DAT) are used instead. Subsequently, the data is used to calculate the path length, duration, the translational velocity and the maximum width of the tornados. Table 2.5 shows the width measurements, r_o and the related intensity scales. It can be seen in this table that the tornados with intensities of EF4 and EF5 have r_o in the range of 0.7km to 1.2km. The only exception is the Jarred, Texas tornado of 1997 which has r_o<0.1km; however, this small r_o might be underestimated due to poor accessibility of the measurement techniques. Similarly, tornados with EF1 through EF3 intensity scales have r_o<0.8km, except for El Reno tornado with r_o=2.3km. It implies that the most intensive tornados of the USA are within the range of $0.7 \leq r_o \leq 2.3$km. An example of the tornado survey by the NWS is shown in Figure 2.7.

However, the NWS technique primarily focuses on determination of the width, the path length, and the translational velocity, and does not report the V_θ. Moreover, since NOAA's technique is based on in-field survey and measurement of the damage width, it considers the debris-induced damages (Dominguez and Selvam, 2017). Meanwhile, the ground surveys are time consuming and often fail to identify the entire tornado track or damage region in sparsely populated areas because of limited vehicle access and resources (Jedlovec et al., 2006). Therefore, the width measurements of the NWS reports can only be used to estimate the relationship between of the width and the EF scale.

Table 2.5. Width measurements by NWS

Tornado	Maximum width (Km)	r_o (km)	Intensity scale	Tornado	Maximum width (Km)	r_o (km)	Intensity scale
Joplin, Mo (2011)	1.6	0.8	EF5	Tuscaloosa (2011)	2.4	1.2	EF4
Moore, OK (2013)	2.1	1.05	EF5	Wheatland Wisconsin (2008)	0.18	<1.0	EF3
Bridge Creek Moore (1999)	1.6	0.8	F5	El Reno (2013)	4.6	2.3	EF3
Jarrel, Texas (1997)	0.16	<0.1	EF5	Springfield, MA (2005)	0.8	0.4	EF3
Phil Campbel (part of an outbreak) (2011)	2	1	EF5	Goshen, Wyoming (2009)	2	1	EF2
Cullman (part of an outbreak) (2011)	1.4	0.70	EF4	Mayflower (2014)	0.5	0.25	EF2
Flat Rock, GA (Part of an outbreak) (2011)	1.6	0.8	EF4	Parrish-Cordova (Part of an outbreak, 2011)	0.34	0.17	EF2
Spencer (1998)	1.6	0.8	F4	Pinhook (Part of an outbreak) (2011)	0.32	0.16	EF2
Manchester (2003)	1.6	0.8	EF4	Wateroak (Part of an outbreak) (2011)	0.27	0.13	EF1
Dimmit, Texas (1995)	2.0	1.0	EF4				

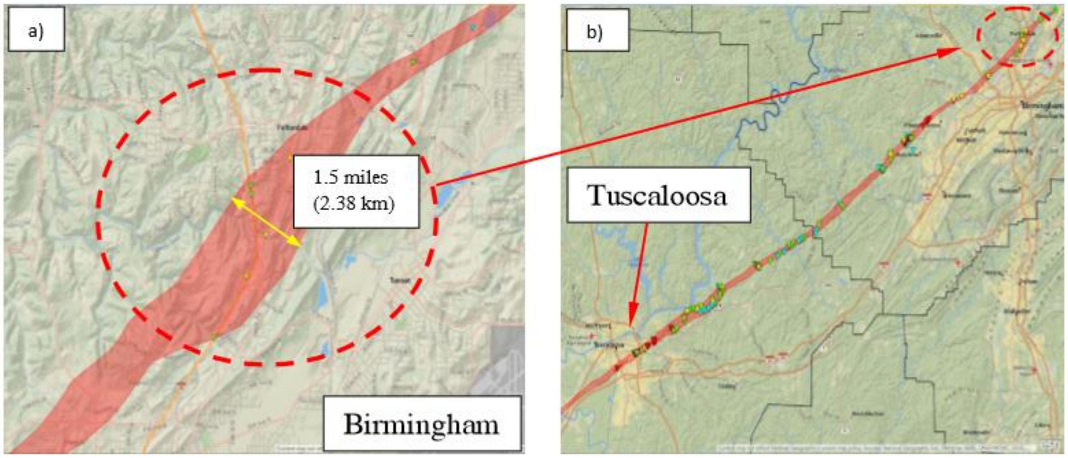

Figure 2.7. Measurement of the width of the Tuscaloosa Tornado by NWS, a) maximum width of tornado; b) The path of the tornado (Taken from Dominguez and Selvam, 2017)

2.7.2.5. Statistical analysis techniques

The earlier attempts of correlating the tornado parameters to the damage were done by Fujita (1971, 1981, 1987) that finally resulted in the Fujita and EF intensity scales. McCarthy (2003) described how the National Tornado Database is correlated to some aspects of the tornado damages. Brooks (2004) established a relationship between the tornado width and the EF damaging scale. They concluded that if the width of tornados increase, they become more intense. However, some actual tornados do not match with their model. Examples of this observation, as shown in Table 2.5, are the 2013 El Reno tornado which had a width of 4.6km corresponding to an EF3 scale, whereas the tornado of May 1997 tornado of Jarrell TX, had only a 0.1km path width corresponding to EF5. The reason of this mismatch is that, while the V_θ is the main damage-causing component of tornados, the model of Brooks (2004) cannot include the V_θ. Therefore, using Brooks' (2004) model is of poor accuracy (Dominguez and Selvam, 2017). In addition, the McCarthy (2003) and Brooks (2004) statistical techniques employ the data of other techniques, such as the data of NWS for their analysis (Brooks, 2004). Thus the drawbacks associated with NWS measurements can also be extended to the statistical techniques.

2.8. Techniques of modeling the tornados

Previous sections showed the post-damage and statistical investigation techniques cannot report the V_θ profile of the tornados. In addition, although the Doppler radars can evaluate the V_θ profile of the tornados, they cannot evaluate the V_θ in elevations less than 20m AGL. Therefore, researchers focused their attention to modeling the tornados in controlled environments. The tornado modeling techniques fall within one of the following categories: laboratory models, analytical models and CFD models.

2.9. Laboratory models

Ward (1972) proposed the first tornado vortex chamber (TVC) to model the tornados in the laboratory setups. Davies-Jones (1973) and Church (1979) reported that in laboratory modeling of the tornados, there are three main parameters that must be investigated carefully. These parameters are R_e, S parameter, AR. The AR is $\frac{H_o}{r_o}$, where H_o is the inflow height and the r_o is the outflow radius of the chamber. Comparing the TVC model to real tornados, the outflow radius corresponds to the radius of the tornado (r_o), where the radius is half of the width of the tornado. AR controls the size of the vortex. S parameter is the ratio of the angular momentum to the radial momentum of the vortex and is related to the tangential velocity of the tornado by $S = \frac{V_\theta}{2.AR.V_{r\infty}}$, hence variation of the V_θ can change the S parameter. In addition, since the V_θ is the main velocity component which is responsible for the tornado damages, the intensity of the tornados is dependent on the S parameter (Church and Snow, 1993; Jischke and Parang, 1974; Natarajan, 2011).

2.9.1. Different types of laboratory models

2.9.1.1. Ward-type TVCs

Figure 2.8 shows a Ward-Type TVC. In these models, the inputs are V_θ and $V_{r\infty}$, and the outlet is vertical velocity on the top of the honeycomb, which is on the top of the circular cylinder. In the Ward-type models, the H_o and r_o and V_θ are required as input of the model (Ward 1972; Jischke and Parang, 1974). Laboratory models of Jischke and Light (1983) and Jienkiewicz and Dudhia (1993) focused on the interaction of the tornado with structures using the Ward type simulator. The earliest Ward-type simulators suffer from small $S<0.5$ (Davies-Jones, 1973). Diamond and Wilkins (1984) proposed a Ward type translating with a rather large r_o, which is equal to 0.457m, H_o=0.508m, with S=0.1 to 0.5. However, their model also has a constant r_o radius, and effect of varying r_o was not discussed in their model.

2.9.1.2. Simulator of Purdue University

Church et al. (1977, 1979) modified the Ward type simulator and developed their Tornado Vortex Chamber-I (TVCI) at Purdue University that used a rotating wire mesh to provide circulation. Their main parameter in their simulator was the S parameter. They found a secondary circulating flow existing within the primary vortex flow. The Purdue simulators showed that that for laminar vortices, the peak velocity is highly dependent upon the S, whereas for turbulent vortices, the S dependency is weak. In the Purdue model, S could be varied from 0 to 1.0 but r_o was constant. The second generation of TVCs was generated by Snow and Lund (1985) and Lund and Snow (1993). Their suggested models had the advantage of changing the r_o, and could use Doppler velocity-meter for making nonintrusive velocity measurements. However, the S range was on the lower side of the normal range (less than 1.0).

2.9.1.3. TVC simulator of Kyoto University

The TVC of Kyoto University (Monji, 1985) rectified the problem of the Ward-type simulators by producing larger r_o radii. This model was later used by Matsui and Tamura (2005), but the problem of this TVC model suffers from S≤1.0.

2.9.1.4. Texas Tech University vortex (TTU) simulator

The simulator proposed by the Texas Tech University vortex (TTU) is a modified version of Ward-type simulator. The main application of the TTUs was studying the tornado-structure interaction, but not the tornado wind-field. In this regard, Wang (2001) and Wang et al. (2001), Fouts et al. (2003) and Mishra et al. (2008) used TTU and performed tests on cubical and cylindrical models. Using a scale of 1:3500 in this simulator, the TTU models have difficulties in simulating a sustained turbulence.

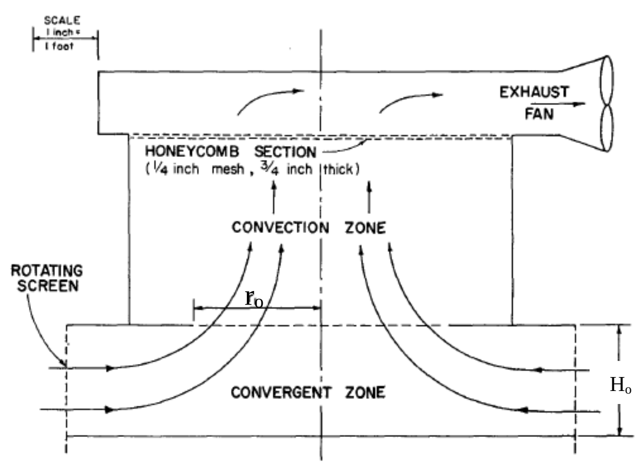

Figure 2.8. Ward type simulator. The Purdue University model, the Japanese Ward-type, and TTU models are modifications of this type

2.9.1.5. Iowa State University (ISU) simulator

In an effort to rectify the drawbacks of the Ward-type TVCs, Sarkar et al. (2006) and Haan et al. (2007) developed the Iowa State University (ISU) tornado simulator. The difference of the ISU with the Ward type was that the ISU was a closed-circuit type with the angular momentum in the flow being introduced by turning vanes at the top of an annular duct above the open test section, whereas the Ward-type had an open circuit with angular momentum being introduced by turning vanes surrounding the test chamber. Figure 2.9 shows the schematic of the ISU simulator. In the ISU simulator, the r_o=75mm and is constant in their model, H_o=30mm-100mm, and S is between 0.08 to 1.4. The scale used in this simulator is scale of 1:100.

Balaramudu (2007), Haan et al. (2008), and Haan, et al. (2010) used this model to study the tornado wind-fields. However, a problem with this simulator was that the transition from a laminar core to a turbulent core that was clearly observable in the Ward-type simulators, is not observed in the ISU simulator which could be due to the instability of the vortex. In addition, the V_θ velocity component and the total flow rate could not be controlled separately in this simulator (Haan et al. 2008). Moreover, the r_o variation cannot be investigated in this model.

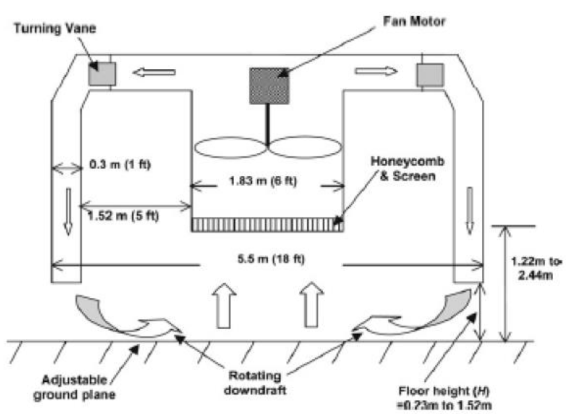

Figure 2.9. Schematic of the ISU simulator

2.9.1.6. Model WindEEE Dome (MWD) simulator

A further development to the laboratory models was the Wind Engineering, Energy and Environment (WindEEE) model (MWD) by Refan (2014) at University of Western Ontario. The schematic of the model is shown in Figure 2.10. The main concept of this simulator is similar to that of the Ward-type model except that the MWD uses controllable fans at the periphery of the TVC to supplement the turning vanes and enhance control of the inflow and a traversing bell mouth to provide a translating source of updraft. Thus, the MWD simulator allows for variation of inflow conditions which implies that the S parameter can be controlled independently in this simulator. Moreover, while the previous laboratory TVCs could produce intensities of as much as EF2, the MWD can produce EF0-EF3 tornados.

Refan (2014) used MWD to relate the S parameter to the tornado intensity. The MWD model has a constant r_o equal to 0.2m with varying simulator height up to 0.4m. The MWD has a scale of 1:16. Their model is capable of modeling tornado with the radii of up to 1.0km. Refan and Hangan (2014) reported that the vortices simulated in MWD with $0.12<S\leq 0.57$ are representatives of EF0 to low-end EF1 actual tornadoes, and the ones simulated in MWD with $0.57<S<1.29$ correspond to full-scale tornadoes with mid-range EF1 to low-end EF3 intensity rating. However, in the MWD apparatus, the S parameter is restricted to $0.12<S<1.30$, and r_o is constant.

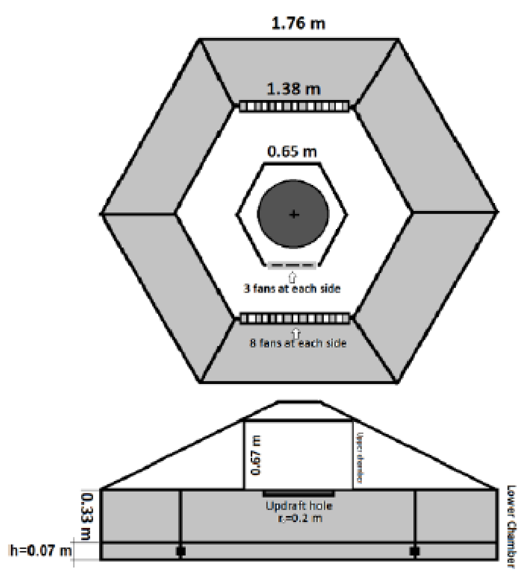

Figure 2.10. Schematic of the MWD simulator (Refan, 2014)

2.9.1.7. VORTECH Simulator

Tang et al. (2016 and 2017) from Texas Tech University proposed the VORTECH simulator to study the effect of changing S and parameters on the V_θ. VORTECH has a constant r_o radius of 4m with varying inflow height of 1m to 2m. This model is the largest among all laboratory models (Figure 2.11). Scale of this model is dependent upon the S parameter to be used, and varies in the range of 1:96 to 1:500. It can evaluate the V_θ at low as 10m AGL, but in their model $S \leq 1.0$.

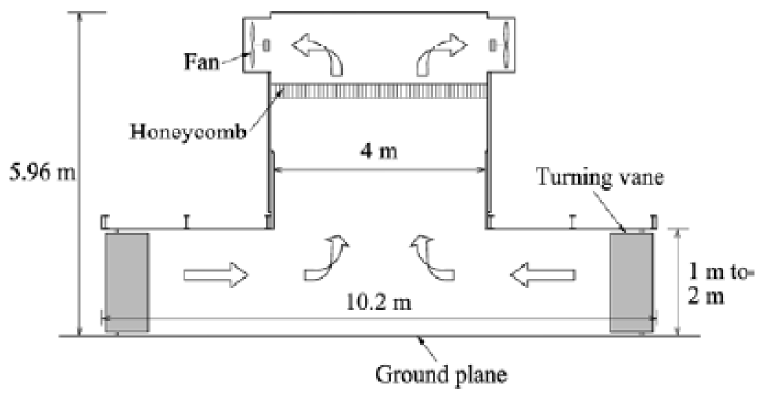

Figure 2.11. Schematic of the VORTECH simulators

2.9.1.8. Wall of wind (WoW) Simulator

Wall of Wind (WoW) was first introduced in 2003 at Florida International University (FIU) as a large scale wind engineering testing facility. However, the main focus of this model is the hurricane simulation rather than tornado modeling structures (Aly et al., 2010).

2.9.1.9. Summary of the laboratory TVCs

Table 2.6 summarizes the results of all the laboratory models. It can be seen in this table that the minimum attainable elevation of the velocity profile is 10m (Tang et al., 2016 and 2017). The reason for the limitations of the laboratory models in evaluating the close-to-ground velocity is that the laboratory data is affected by the presence of the boundaries of the apparatus, measurement tools, and the scale used in the experiment (Smith, 1986; Kopp, 2016 and 2017).

Also, Table 2.7 summarizes the tornado parameters used in the laboratory models. It can be seen in this table that in all the laboratory models, the r_o range is from 0.8km to 2.0km and S≤1.0. These limits imply that these testing facilities cannot replicate the different tornado sizes, nor tornado intensities.

Table 2.6. Results of the laboratory TVCs

Reference	Type	r_o(km)	Swirl ratio	$V_{\theta,max}$	Minimum z(m)
Church (1979)	Ward	1.5	0 0.338 0.765	NA	15
Mitsuta (1984)	Ward	1.0	<1.0	12m/s	20
Monji (1985)	Ward	0.38	2.3	41m/s	40
Church (1993)	PU Ward	1.5	0.28	4.5 $V_{r\infty}$	~100
Matsui (2008)	Ward	0.15	0.14	2.0 $V_{r\infty}$	10
Mishra et al. (2008)	TTU	0.19	0.19	2.5 $V_{r\infty}$	NA
Matsui and Tamura (2009)	Ward	0.15	NA	NA	10
Lund and Snow (1993)	Ward	1.0	0.67	NA	~20
Tari et al. (2010)	ISU	0.75	0.08 0.4 0.68	0.9 $V_{r\infty}$ 4.5 $V_{r\infty}$ 6 $V_{r\infty}$	~50
Lund and Snow (1993)	Ward	1.0	0.67	NA	~20
Sarkar and Haan (2005)	ISU	1.8	0.5	45m/s to 80m/s	20
Gallus et al. (2006)	ISU	0.8-1.0	1.0	75m/s to 157m/s	20
Matsui (2008)	Ward	0.15	0.14	2.0 $V_{r\infty}$	10
Matsui (2009)	Ward	0.15 0.15	0.14 0.65	2.5 $V_{r\infty}$ 5.5 $V_{r\infty}$	10
Zhou et al. (2016)	Ward	0.5	1.2 to 1.6	45-80m/s	NA
Natarajan & Hangan (2010)	WindEEE	0.4	0.5	6.0 $V_{r\infty}$	16

Table 2.6 (Cont.)

Razavi and Sarkar (2016)	ISU	1.8	0.78	NA	22
Natarajan (2012)	WindEEE	0.4	0.28 0.5	5.5 $V_{r\infty}$ 6.0 $V_{r\infty}$	16
Refan (2014)	WindEEE	0.35	1.29	2.3 $V_{r\infty}$	16
Tang et al. (2016)	VORTECH	4.0	0.13 to 0.6	2 $V_{r\infty}$ to 2.6 $V_{r\infty}$	10
Tang et al. (2017)	VORTECH	4.0	0.17 to 0.84	2 $V_{r\infty}$ to 3 $V_{r\infty}$	10

Table 2.7. Summary of laboratory tornado simulators

Simulator Type	r_o(km)	S	Simulator Type	r_o(km)	S
Ward-type	0.3-3.0	≤1.0	ISU	0.8-1.2	0.08- 1.14
MWD	0.4	0.12<S<1.30	MWD	0.4	0.12<S<1.30
TTU	1.0-3.0	0.25-1.68	VORTECH	4.0	<1.0
Kyoto	1.3	<1.0			

2.10. Analytical tornado vortex techniques

The analytical tornado vortex techniques model the tornado at every instant of time by a mathematical equation. The most frequently used analytical models for tornado modeling are the RCVM, Burger-Rotts (BR), and Sullivan models as discussed by Strasser and Selvam (2015). These models are briefly discussed in the following sections.

2.10.1. Rankine combined vortex Model (RCVM)

This model divides the vortex into two parts (Wilson, 1977): the inner part of the vortex which is in solid body rotation and the outer part of the vortex in which the V_θ is a decreasing function of radius, as shown in Figure 2.12. The RCVM represents the air flow around a tornado with only the

V_θ component, which implies that that the radial and axial velocity components are not included in this model (Lewellen, 1976).

Maxworthy et al. (1985), Vatistas (1989), Selvam (1985, 1993) and Selvam and Millett (2003) used RCVM for simulating the tornado-like vortices for flows over cubes. Brown and Wood (2011), Wurman (2002), Wurman and Gill (2000) compared Doppler velocity data from tornadoes with RCVM and concluded that the results of all model were in good agreement with the actual measurements. Xu and Hangan (2009) modeled the tornado-like vortex by using a free narrow jet solution combined with RCVM. The advantage of their model is that the upward free-jet can represent the two-dimensional radial and axial motions. Therefore, together with the V_θ profile of the RCVM, this model provides three velocity components for the tornado-like vortices. Selvam and Gorecki (2012) used RCVM model to study the influence of the different ratios of tornado sizes to the cylinder size on the tornado forces. Strasser and Selvam (2015), Strasser, Yousef and Selvam (2016) and Dominquez and Selvam (2016) used this model to study the interaction of tornados with structures and hills. Also, Ahmed and Selvam (2015) used RCVM to investigate the ridge effects on the tornado path deviation and Yousef (2017) employed this model to investigate the tornado interaction with the dome buildings.

An advantage of the analytical models is they are easy to implement, and they only require two values to be defined in the model, namely the radius of the location and the tangential velocity (Selvam and Millett, 2003 and 2005). However, discontinuity of the velocity derivatives at the point of transition from free forced mode to forced, and also the overestimation of the velocity near the core are the shortcomings of the Rankine models. In addition, the RCVM overestimates the velocity near the core (Refan, 2014).

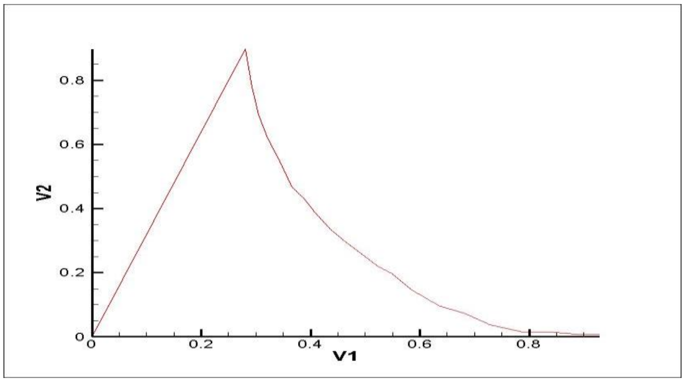

Figure 2.12. Rankine combined vortex model (RCVM)

2.10.2. The Burgers-Rott (BR) vortex

This model is an exact solution to the Navier-Stokes (NS) Equation. the BR vortex has a central axis similar to RCVM, around which is an azimuthal flow, as shown in Figure 2.13. Unlike the RCVM, the BT model has radial and axial velocity components as well. In addition, unlike the RCVM, there is partially an actual counterpart for this model in the atmosphere, as it results from suction at great height above a plane surface. Xu and Hangan (2009) compared the values of the actual tornados with the BR model and showed that this model produced similar results in four out of five locations.

However, the BT model suffers from some deficiencies. In the BR model, the axial velocity is constant with radius, but linear with height, which means that the vertical velocity is only a function of z but not x, which implies that the velocity field is similar everywhere (Varistas, 1989). Furthermore, modeling turbulence effect in this model is problematic (Lewellen, 1974) since when the viscosity is included, the partial differential equations of the NS equations will exhibit a diffusive behavior (Kilty, 2005). In addition, the vertical pressure gradient increases by height without bound, whereas it is negligible close to the ground. Therefore, BR is not a good model for finding the close-to-ground velocity (Refan, 2014).

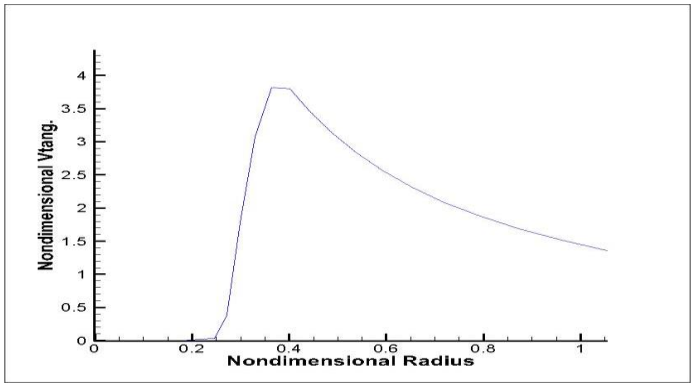

Figure 2.13. The BR vortex model (Kilty, 2005)

2.10.3. Sullivan vortex model

Similar to the BR model, the Sullivan vortex is also an exact solution to the NS Equation and has similarities to the BR model, as shown in Figure 2.14. The Sullivan vortex describes the flow in an intense tornado with a central downdraft, and localizes its updraft to a particular place. However, placing the vortex at the center of the updraft makes the model too symmetric to describe a real tornado. Furthermore, the Sulivan model is poor in presenting the V_θ profile (Tang et al., 2016 and 2017). In addition, the minimum reported elevations using analytical models are almost 50m (Wen, 1975; Karstens et al., 2010).

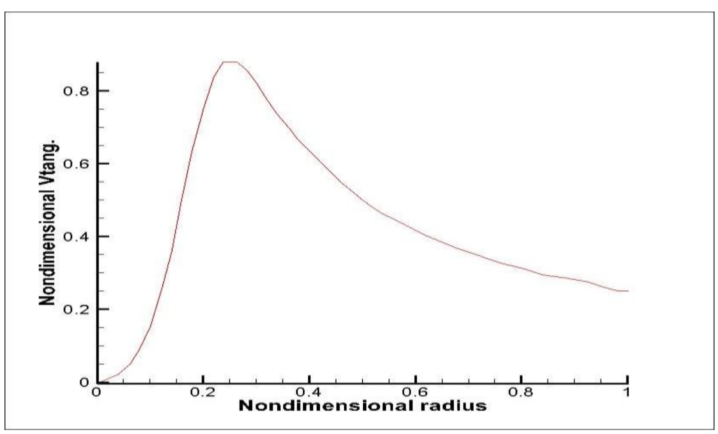

Figure 2.14. Sullivan vortex model (Kilty, 2005)

2.10.4. Lamb-Ossen vortex model

Lamb-Ossen vortex mode represents a solution to the laminar NS Equations with axisymmetric solution for the swirl velocity together with the assumption that the axial and radial velocities are zero (Tryggeson, 2007). Strasser, Yousef and Selvam (2016) used the Lamb-Oseen model or the variant of Vatistas model to study the dynamic amplification of tornado wind field for a circular cylinder. One of the drawbacks of this model is that it considers radial and vertical velocity to be zero as a start and reports high V_θ magnitude close to the ground.

2.11. CFD tornado chamber models

In general, the CFD tornado chamber models are the representation of the experimental TVCs in a computational domain. In this regard, some CFD studies modeled the Ward-type simulator, such as Wilson and Rotunno (1986), Lewellen et al. (1997, 2005), Liu and Ishihara (2012, 2013, 2014), and Dominguez and Selvam (2017), some other studies simulated the ISU model in computer, such as Sarkar et al. (2005), Gallus et al. (2006) and Kuai et al. (2008). The former computational domain is called open outlet, and the latter is called semi-open outlet, which are shown in Figures 2.15 and 2.16, respectively. The semi-open outlet is mostly used for either considering the translation effect of the tornados or investigating the tornado interaction with a building inside the model, such as Phuc et al. (2012).

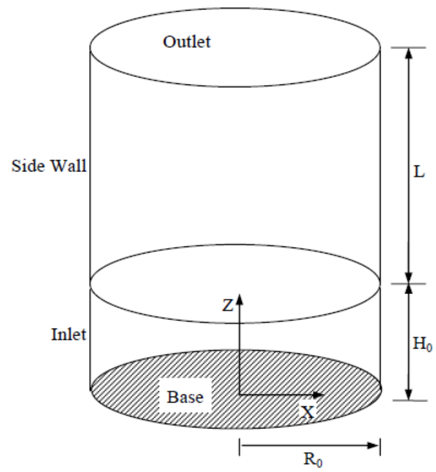

Figure 2.15. The computational model with open outlet. It is based on Ward-type simulator.

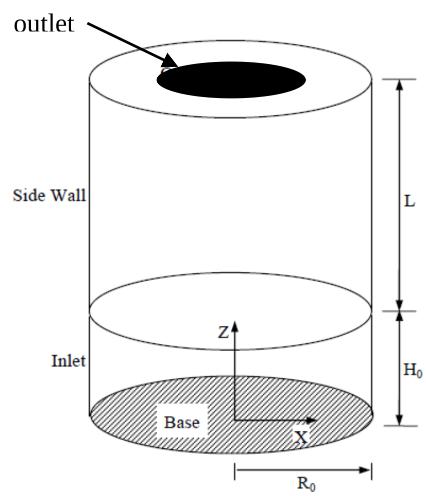

Figure 2.16. The computational model with semi-open outlet. It is based on ISU simulator.

2.11.1. Investigation of the tornado parameters by the CFD chamber models

Wilson and Rottuno (1986) proposed models with S~0.3 and r_o=1.0km. The constant r_o and small S parameter are shortcomings of their models. Lewellen et al. (1997 and 1999) investigated the influence of S value on tornado intensification near the surface by using LES, and reasonably captured the turbulent effects. Afterward, Lewellen et al. (2008) and Lewellen (2012) used CFD with a focus on improvement of the MGSs, for r_o=1.0km. They also showed that the core radius

(r_c) increases by increase of the S parameter. However, they only considered r_o=1.0km, and did not take into account of the effect of variation of r_o. Moreover, the minimum attainable elevation is almost 27m AGL in the studies of Lewellen et al. (Table 2.8).

Also, Ishihara et al. (2011) and Liu and Ishihara (2013) used CFD models with constant r_o=150mm, capable of producing actual r_o radii of up to 1.0km. However, the S parameter was less than 1.0. Liu and Ishihara (2012) used a similar model with the same size but capable of producing S~3.8. However they did not present the effect of high S values on V_θ. Likewise, Liu and Ishihara (2016) used the same model and added the roughness effect. Although their models are capable of capturing spacing of 1.0m close to the ground, their models are limited to r_o=1.0km (Table 2.8). Phuc et al. (2012) used r_o=0.3m and S=0.68 to determine the relation of the aspect ratio to the pressure coefficients, but did not report the velocity wind-field. Zhao et al. (2017) used the largest r_o equal to 800m, but their focus was on variation of the H_o rather than the r_o (Table 2.8). Natarajan and Hangan (2012) used S=0.5 and 2.0 with r_o=H_o=0.4m, and Natarajan (2012) proposed a model with S~0.3 and r_o=1.0km to investigate the effect of variation of the S value on the V_θ profile. However, the minimum attainable elevation in their models is 20m AGL. In addition, the constant r_o and small S parameter are shortcomings of their models (Table 2.8). Hangan and Kim (2008) proposed a 3D numerical model for TVCs to investigate dependency of the V_θ of actual tornados on the S and the relation with Fujita scale. They used S in the range of 0.28 to 2.0 and investigated the 1998 Spencer tornado. However, they only considered r_o=1.0km which is the radius of the 1998 Spencer tornado. Gallus et al. (2006) and Kuai et al. (2008) utilized models with r_o= 800m r_o=1000m and r_o=1100m, which correspond to the r_o of actual tornados. Also, they used S parameter in the range of $0.17 \leq S \leq 0.26$, and conducted parameter sensitivity tests for the mesh size, boundary conditions and surface roughness. However, the limitation of their study is small range of S and r_o.

2.11.2. Summary of the CFD models

Table 2.8 presents a summary of the CFD parameters. It can be seen that the CFD models suffer from limited range of the r_o and S parameters. The CFD models are limited to the $r_o \leq 1.0$km, whereas the actual is up to 3.0km. In addition, in the CFD models, S is mostly less than 1. In addition, the minimum elevation attainable in the CFD studies is 6m (Liu and Ishihara, 2012, 2013, and 2014). Hence, the existing CFD studies cannot evaluate the V_θ profile in the elevation of the typical buildings (z=3.3m).

Table 2.8. Results of CFD tornado chamber models on the V_θ profiles

Reference	r_o(km)	Swirl ratio	$V_{\theta,max}$	Minimum z (m)
Wilson and Rotunno (1986)	1.0	0.3	$4.99V_{r\infty}$	20
Wicker and Wilhelmson (1993)	1.0	NA	32m/s	20
Lewellen et al. (1997)	1.0	0.94	$6.6\ V_{r\infty}$	27
Lewellen et al. (2005)	1.0	0.94	$6.5\ V_{r\infty}$	27
Sarkar et al. (2005)	0.46	0.17	$4.4\ V_{r\infty}$	20
Kuai et al. (2008)	0.8 and 1.0	0.17	$4.4\ V_{r\infty}$	20
Hangan and Kim (2008)	0.4	0.28	$3.75V_{r\infty}$	20
Ishihara et al. (2011)	1.5	0.31	NA	10
Liu and Ishihara (2012)	1.5	NA	NA	10
Liu and Ishihara (2013)	1.5	0.6 3.8	15.3m/s 24m/s	10
Liu and Ishihara (2014)	1.5	NA	NA	10

Table 2.8. (Cont.)

Reference	r_o(km)	Swirl ratio	$V_{\theta,max}$	Minimum z (m)
Natarajan (2012)	0.4	0.28	5.5 $V_{r\infty}$ - 7.5 $V_{r\infty}$	NA
Zhao et al. (2017)	0.8	<1.0	3 $V_{r\infty}$ to 4 $V_{r\infty}$	NA
Tao Tao et al. (2017)	NA	NA	26m/s 25m/s	NA
Dominguez and Selvam (2017)	1.0	0.6	4.98 $V_{r\infty}$	1

2.12. Criteria of comparing the tornado simulations to the actual tornados

2.12.1. Significance

The main parameters of the laboratory and CFD models are the R_e, S and r_o. Using high value of R_e makes the simulation results independent of R_e. Thus, the simulation results rely heavily on S and r_o. Hence, the laboratory and CFD models report the flow characteristics by the S parameter, which is directly related to the V_θ and indicates the intensity of tornados. However, the S parameter is very difficult to determine in actual tornados because there is no clear definition of the inlet/outlet boundary conditions in the actual tornados (Refan, 2014). Therefore, comparing criteria should be defined to compare the simulation results to the actual tornados. These criteria should be measurable geometric scales. There are various geometric lengths in a tornado simulator such as updraft radius, inflow depth, r_c and z_{max}. After determining the proper criteria, the velocity fields can be matched with the numerical simulations.

2.12.2. Defining the comparison criteria

Baker and Church (1979) used the average velocity as the comparison criteria and called it as length scale. However, Nolan (2012) showed that this length scale is not accurate for small tornados. Mishra et al. (2008) used r_c as length scale using the TTU simulator for the 1998 Spencer tornado. They also added that the radial profile of the V_θ at various heights can be used for comparison of the simulations to actual tornados. Haan et al. (2008) validated the ISU simulator through comparisons between full-scale and simulator flow fields of Spencer and Mulhall tornados. They used tornado structure, and the radial V_θ profiles as a comparison criterion. In other words, they compared the radial V_θ profiles of their simulations at different heights to the in-field measurements and observed that they collide perfectly on each other. They concluded that the r_c and the z_{max} are the two important comparison criteria. Zhang and Sarkar (2012) used Particle Image Velocimetry (PIV) to compare the V_θ profile of the simulated tornado with that of an actual tornado using the $V_{\theta,max}$ and r_c as comparison criteria. Kuai et al. (2008) employed a CFD model and used $V_{\theta,max}$ and r_o as the criteria to compare the simulation results to the radar data. They used the radial V_θ profile and the $V_{\theta,max}$, r_c and z_{max} as the comparison criteria. Similarly, Refan (2014), and Refan et al. (2017) used the GBVTD to determine intensity of the actual tornados and for this purpose they used the r_c and z_{max} as the comparison criteria for their comparison. Therefore, reviewing the previous studies shows that the structure, r_c and z_{max} of tornados are proper criteria for comparison of the simulations to the actual tornados.

2.13. Summary of the chapter

Review of the previous studies on the tornado effects on buildings indicates that the infield and post-damage investigations are not capable of evaluating the V_θ profile close to the ground. On the other hand, the laboratory TVCs, despite being able to model the tornados, are limited to minimum elevation of 35m AGL and certain r_o lengths. The analytical vortex models cannot evaluate the V_θ profile at less than 50m AGL. In parallel, although the CFD models can model tornados for $0.2 \leq S \leq 3.6$, they are limited to $r_o \leq 1.0$km. In addition, the CFD models, cannot evaluate the V_θ profile at z=3.3m, which is the elevation of the typical buildings. Moreover, review shows that the r_o of the most intense tornados in the USA is in the range of 0.7km to 2.3km.

CHAPTER 3. RESEARCH METHODOLOGY

In this chapter, the methodology employed in the study is given. The main reason for using CFD technique in this study is that, unlike the laboratory models, the CFD techniques provide full access to wind field as well as allowing a control of important simulation parameters without compromising the accuracy of the simulation. The Navier Stokes (NS) equations for the incompressible flow were approximated by Finite Volume Method (FVM), which was found to be more efficient than Finite Element Method (FEM) for the tornado modeling purposes (Selvam, 1994). The turbulence is modeled by Large Eddy Simulation (LES), which is ideally a proper technique for the strong short-term vortices of tornados (Lim et al., 2009).

3.1. Governing Equations

The governing equations in cylindrical coordinates system using LES for axisymmetric model are obtained by filtering the time dependent NS equations as follows (Stein and Harlow, 1974):

The continuity equation is:

$$\frac{1}{r}\frac{\partial}{\partial r}(r.V_r) + \frac{\partial}{\partial z}V_z = 0 \quad (3.1)$$

The r-component of momentum equation is:

$$\frac{\partial V_r}{\partial t} + \frac{1}{r}\frac{\partial r{V_r}^2}{\partial r} + \frac{\partial V_r V_z}{\partial z} = -\frac{\partial p}{\partial r} + \left[2v_{eff}\frac{\partial^2 V_r}{\partial r^2} + \frac{2}{r}v_{eff}\left(\frac{\partial V_r}{\partial r} - \frac{V_r}{r}\right) + \frac{\partial}{\partial z}v_{eff}\left(\frac{\partial V_r}{\partial z} + \frac{\partial V_z}{\partial r}\right)\right] + \frac{{V_\theta}^2}{r} \quad (3.2)$$

The θ-component of momentum equation is:

$$\frac{\partial V_\theta}{\partial t} + \frac{1}{r}\frac{\partial r V_r V_\theta}{\partial r} + \frac{\partial V_\theta V_z}{\partial z} = -\frac{V_r V_\theta}{r} + \left[2v_{eff}\frac{\partial^2 V_\theta}{\partial z^2} + \frac{\partial}{\partial r}v_{eff}\left(\frac{\partial V_\theta}{\partial r} - \frac{V_\theta}{r}\right) + \frac{2}{r}v_{eff}\left(\frac{\partial V_\theta}{\partial r} - \frac{V_\theta}{r}\right)\right] \quad (3.3)$$

The z-component of momentum equation is:

$$\frac{\partial V_z}{\partial t} + \frac{1}{r}\frac{\partial r V_r V_z}{\partial r} + \frac{\partial {V_z}^2}{\partial z} = -\frac{\partial p}{\partial z} + \left[2v_{eff}\frac{\partial^2 V_z}{\partial z^2} + \frac{1}{r}\frac{\partial}{\partial r}v_{eff}(r\left(\frac{\partial V_r}{\partial z} - \frac{\partial V_z}{\partial r}\right))\right] \qquad (3.4)$$

In which

$$v_{eff} = v + v_{sgs}$$

And v_{sgs} is calculated as follows (Barhaghi and Davidson, 2003):

$$v_{sgs} = (C_s\nabla)^2 f_\mu \sqrt{2.s_{ij}.s_{ij}}$$

Where $C_s = 0.1$, and

$$f_\mu = 1 - \exp(-\frac{y^*}{25})$$

$$2.s_{ij}.s_{ij} = 2\left[(\frac{\partial V_r}{\partial r})^2 + (\frac{1}{r}\frac{\partial V_\theta}{\partial \theta} + \frac{V_r}{r})^2 + (\frac{\partial V_z}{\partial z})^2\right]$$
$$+ \left[(\frac{\partial V_r}{\partial z} + \frac{\partial V_z}{\partial r})^2 + (\frac{1}{r}\frac{\partial V_r}{\partial \theta} + \frac{\partial V_\theta}{\partial r} - \frac{V_\theta}{r})^2 + (\frac{\partial V_\theta}{\partial z} + \frac{1}{r}\frac{\partial V_z}{\partial \theta})^2\right]$$

The governing equations are non-dimensionalized using $V_{r\infty}$ and H_o as the reference values. The reference value for H_o and $V_{r\infty}$ are considered to be 1.0km and 1.0 m/s, respectively. For these reference values the R_e will be $1x10^8$.

3.2. Computational domain and boundary conditions

The computational domain used in this study is similar to the computational domain of Lewellen et al. (1997). Their computational domain is a Ward-Type TVC of 1km x 2km domain, which means that the updraft radius (r_o) and the domain height ($h=2H_o$) are respectively 1.0km, 2.0km, and the inlet height (H_o) is 1.0km. considering H_o=1.0km as reference value, therefore the nondimensional computational domain is 1.0x2.0 ($r_o=H_o$ & $h=2H_o$). However, the present study uses a similar domain with the only difference of using various r_o from 0.7km to 2.3km. Therefore, the nondimensional r_o varies from 0.7 to 2.3 The increment of r_o is 0.1, which means that r_o will be 0.7, 0.8, 0.9 and so on. Nondimensional H_o is 1.0 and $h=2H_o$ in this study. The boundary conditions of the axisymmetric model are similar to study of Wilson and Rotunno (1986) as shown in Figure 3.1 and Table 3.1.

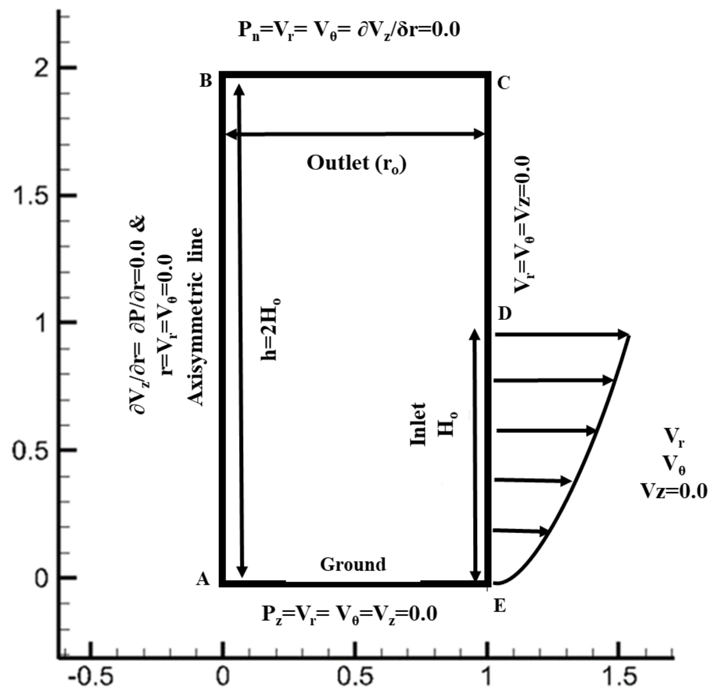

Figure 3.1. Axisymmetric computational domain and the boundary conditions

Table 3.1. Boundary conditions of the model

Region	Boundary type	Boundary Condition	Region	Boundary type	Boundary Condition
AB	Axisymmetric line	$\frac{\partial V_z}{\partial r} = \frac{\partial P}{\partial r} = 0.0$ $r = V_r = V_\theta = 0.0$	DE	Inlet	$V_{r\infty}$ V_θ V_z=0.0
BC	Outlet	$P_n = V_{r\infty} = V_\Theta = \frac{\partial V_z}{\partial r} = 0.0$	EA	Ground	$P_z = V_{r\infty} = V_\Theta = V_z = 0.0$
CD	Wall	$V_{r\infty} = V_\Theta = V_z = 0.0$			

3.3. Wall function

For the cells close to the ground of the TVC and to the symmetry line, the Law of the Wall is used in the modeling. In this technique, the turbulence near that boundary is a function of only the flow conditions pertaining to that wall and is independent of the flow conditions further away. Law of the Wall is derived and applied using Equations (3.5) to (3.7) taken from Neale et al. (2006). For the distance of y from the wall, the friction velocity u_r can be defined as:

$$u_r = \sqrt{\tau_w/\rho} \qquad (3.5)$$

Where τ_w is the wall shear stress, and is based on the velocity gradient in the direction normal to the surface of the wall (Neale et al., 2006):

$$\tau_w = \rho\nu\frac{\partial V_r}{\partial y} \qquad (3.6)$$

Where the dimensions of the parameters are: y[L], V_r(y)[L/T], τ_w [M/LT^2], ρ[M/L^3], ν[L^2/T]. The dimensionless length and velocity are, respectively:

$$y^* = \frac{u_r y}{\nu}$$

$$V_r{}^+ = \frac{V_r}{u_r} \qquad (3.7)$$

3.4. Radial and tangential velocity components

$V_{r\infty}$ is assumed to vary logarithmically from the ground at the inlet and the equation for the radial velocity is as follows:

$$V_r = C_1 ln\frac{z+z_o}{z_0} \qquad (3.8)$$

For open country or Exposure C taking zo=0.035m, the nondimensional z_o will be 0.035/1000=3.5x10^{-5}. Keeping the maximum $V_{r\infty}$=1.0m/s at z=Ho, the corresponding C_1 becomes:

$$C_1 = \frac{V_{r\infty}}{ln\frac{H_O+z_O}{z_O}} = 0.0975$$

Knowing $V_{r\infty}$, then V_θ is obtained at the inlet by rearranging Equation (1.3) as follows:

$$V_\theta = \frac{S(2H_0)V_{r\infty}}{r_0} \qquad (3.9)$$

In Equation 3.9, the $V_{r\infty}$ and H_o are constant, and the two parameters of S and r_o will be varied to determine the V_θ.

3.5. Grid resolution of the computational domain

Dominguez and Selvam (2017) used the same domain as that of Lewellen et al. (1997) but used MGS=0.001H_o alongside the r- and z- axes. The present study also uses MGS=0.001H_o along the r- and z-axis in the vicinity of the axisymmetric line (z axis). Considering H_o=1.0km for non-dimensionalization, thus the model can capture 1.0m spacing close to the axisymmetric line. In addition, the grid spacing exponentially increases by 1.1 from the center of the tornado and the maximum spacing is limited to 0.1H_o. Figure 3.2 shows the computational domains of r_o=0.7km, 1.0km, 1.5km and 2.0km using MGS=0.001H_o. As can be seen in this figure, more refinement is applied near the ground and near the z-axis in order to properly capture the boundary layer. This refined grid close to ground enables the model to evaluate the V_θ in the vicinity of the ground. Figure 3.3 shows the zoomed view close to the symmetry line of the computational domain, and it can be seen that the spacing of 1.0m is captured close to the ground. The number of nodes for different r_o are given in Table 3.2. Table 3.3 summarizes the physical and mesh parameters of the numerical tornado simulator.

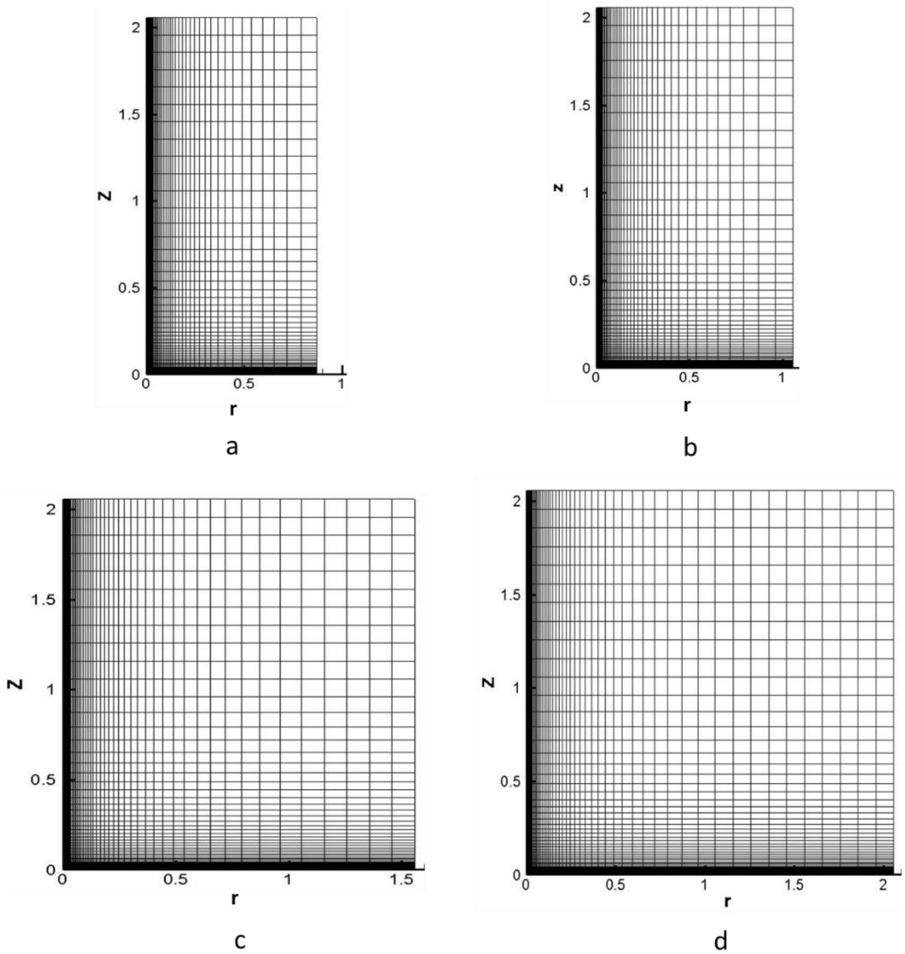

Figure 3.2. Computational domains with MGS=0.001H_o for: a) r_o=0.7km; b) r_o=1.0km; c) r_o=1.5km; d) r_o=2.0km

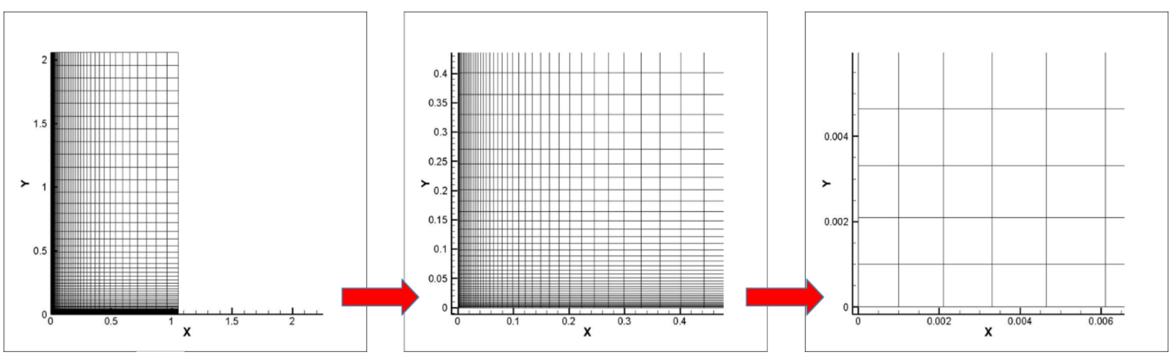

a b c

Figure 3.3. a) Computational domain for r_o=1.0km; b) Zoomed view of the high resolution close to symmetry line; c) Zoomed view of the high resolution which captures 1.0m spacing close to the symmetry line.

Table 3.2. Number of nodes in computational domain with MGS=0.001H_o

Radius (r_o)	Number of nodes in the computational domain	Radius (r_o)	Number of nodes on the computational domain
0.7km	46x60	1.6km	56x60
0.8km	48x60	1.7km	57x60
0.9km	49x60	1.8km	58x60
1.0km	50x60	1.9km	59x60
1.1km	51x60	2.0km	60x60
1.2km	52x60	2.1km	61x60
1.3km	53x60	2.2km	62x60
1.4km	54x60	2.3km	63x60
1.5km	55x60		

Table 3.3. Physical parameters and mesh parameters of numerical tornado simulator

Parameter	Actual value	Nondimensional value	Parameter	Actual value	Nondimensional value
Domain height (h)	2000m	2.0	Reynolds number	1.e8	1.e8
H_o	1000m	1.0	$V_{r\infty}$	1.0 m/s	1.0
r_o	700m-2300m	0.7-2.3	MGS	0.001H_o	0.001

3.6. Solution scheme

The CFD model uses the SOLA-Yaqui type algorithm to solve the equations (Hirt et al., 1975). In this method, a staggered grid is used where velocities are stored at the nodes and the pressure at the middle of the cell. In the momentum equation, the diffusion and convention terms are respectively implicit and explicit. The equations are approximated using second order FVM. At this time, the pressure is solved using SOLA type pressure correction. The advantage of using the Yaqui-type configuration is to avoid the problem of pressure-velocity decoupling (Harlow and Welch, 1965; Selvam, 1992). The computer model is run for 5 time units with a time step of 0.1 to satisfy the CFL condition.

3.7. Running the program

The program used for this simulation was developed at the Computational Laboratory of the Civil Engineering Department at University of Arkansas, and is called **Axisym6**. The program is developed with FORTRAN language, is run in LINUX terminal on the server of the Computational Mechanics Lab (CML) of the University of Arkansas. Each simulation takes 60 minutes to 150 minutes depending on the size of the domain.

3.7.1. Program input

The SSH Secure File Transfer is used to connect to the server and to run the program in LINUX environment. A sample program input is shown in Table 3.4 and Figure 3.4. In the program input, XMAX refers to the r_o and S refers to the swirl ratio. The input is given to the program using *.txt file. In this study, the H_o=1000m and is constant.

Table 3.4. Data input of the **Axisym6** program for r_o=1.0km and S=1.0

Program inputs	Definition	Value (non-dimensional)
HMIN	Minimum grid spacing (MGS)	0.001
HMAX	Maximum grid spacing	0.1
FAC	growth factor of the spacing	1.1
XMAX	Radius of the domain (tornado radius, r_o)	0.7
ZMAX	Height of the domain (h)	2.0
DT	Time spacing	0.01
REN	Reynolds number	1.e8
S	Swirl ratio	1.0
TTIME	Total computation time unit	5.0

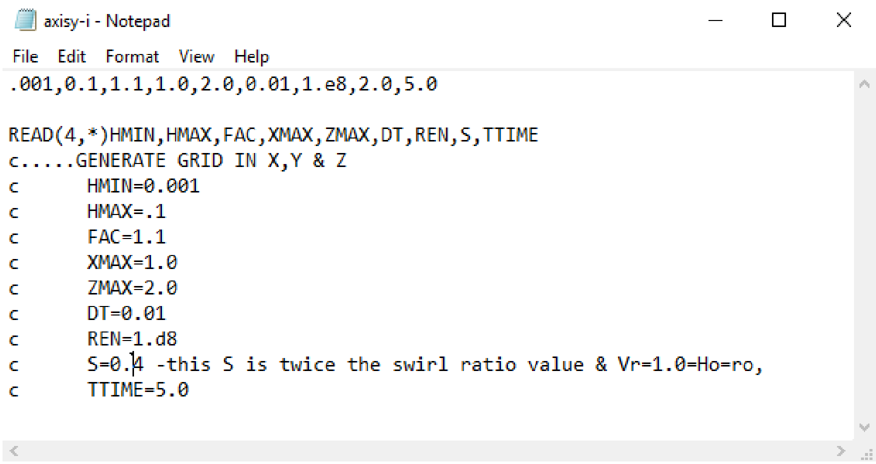
axisy-i - Notepad

File Edit Format View Help

```
.001,0.1,1.1,1.0,2.0,0.01,1.e8,2.0,5.0

READ(4,*)HMIN,HMAX,FAC,XMAX,ZMAX,DT,REN,S,TTIME
c.....GENERATE GRID IN X,Y & Z
c       HMIN=0.001
c       HMAX=.1
c       FAC=1.1
c       XMAX=1.0
c       ZMAX=2.0
c       DT=0.01
c       REN=1.d8
c       S=0.4 -this S is twice the swirl ratio value & Vr=1.0=Ho=ro,
c       TTIME=5.0
```

Figure 3.4. Data input of the **Axisym6** program for r_o=1.0km and S=1.0

3.7.2. Post-processing

The output of the program for each run is stored in *.plt file which can be opened in TECPLOT software. The results include the pressure (p) and V_θ at different (r,z) points of the domain.

A program, called the **velc** program is used to plot the radial and vertical velocity profiles at different heights. The **velc** is written in FORTRAN. The input of the **velc** program is the output of the **Axisym6** program. Table 3.5 and Figure 3.5 show an input sample of the **velc** program for r_o=1.0 at z=51.5m. Input of Table 3.5 shows that nine files from **Axisym6** are used as input for **velc**. Each of these nine files correspond to a certain S value. The **velc** program plots the profile at node=28. This node corresponds to z=51.5m for r_o=1.0km. in order to plot the velocity profiles at a certain distance from the tornado center, the same program can be used. In this case, instead of using the node number in the desired elevation, the number of node in the desired radial location should be used as input. The results are stored on a *.plt file and are thus displayed in TECPLOT.

Table 3.5. Sample input of **velc** for r_o=1.0km at z=51.5m

Program inputs	Value
Number of nodes in X direction	50
Number of nodes in Y direction	60
Number of input files	9
Node corresponding to desired elevation	28

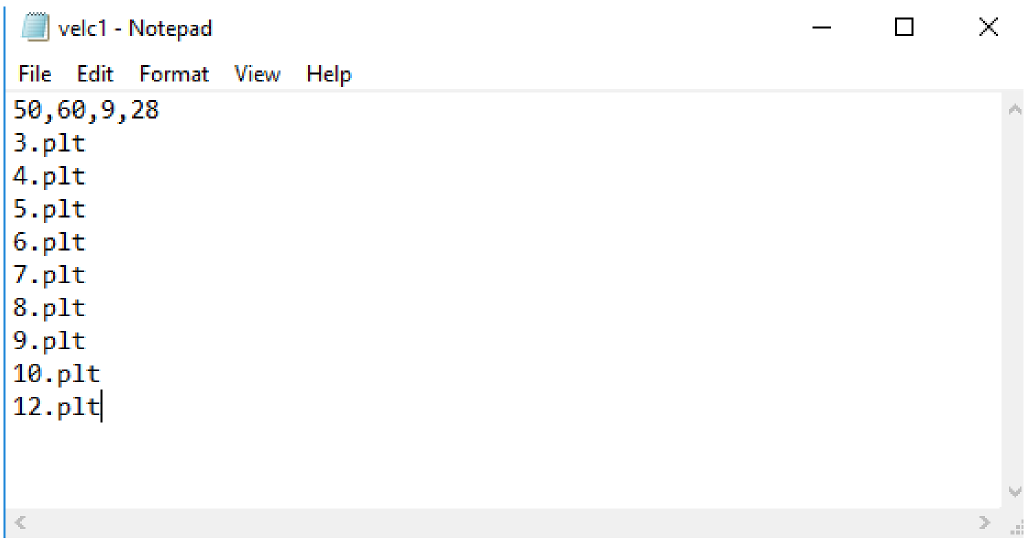

Figure 3.5. Sample input of **velc** program for r_o=1.0km at z=51.5m

3.8. Verification of the simulations

Simulation results are verified against the radar measurements of actual tornados. For verification purpose, the comparison criteria defined in Section 2.12 are employed, which include the vertical structure, r_c, z_{max}.

3.8.1. Assumptions made for comparison of the simulations to the radar measurements

In order to verify the simulation results against the radar measurements of actual tornados, the following assumptions are made:

1. Only actual tornados for which radar measurements of r_o, r_c, z_{max} are available are considered for comparison.

2. The r_o of actual tornados, taken from radar measurements, are used in the simulation; the results are then compared to the data collected from actual tornados.
3. Only actual tornados with the radii in the range of 0.7km to 2.3km are considered for comparison. As shown in Table 2.5, actual tornados with r_o<0.7km are of less significance in terms of intensity and damage and are thus excluded. Similarly, the largest tornado r_o in the USA is the EL Reno tornado of 2013 with r_o=2.3km.

3.9. Summary of the chapter

In this chapter, the governing equations using LES for axisymmetric model, and subsequently, the computational domain and the boundary conditions were presented. Finally, verification criteria were proposed.

CHAPTER 4. INVESTIGATION OF THE EFFECT OF VARIATION OF THE R_O ON THE MAXIMUM V_θ

Jischke and Parang (1974) and Church et al. (1979) asserted that the $V_{\theta,max}$ is dependent on the S parameter, and variation of the S parameter affects the r_c and z_{max}. In this chapter, initially the S parameter producing the $V_{\theta,max}$ will be determined for different r_o radii, and then the effect of variation of the S parameter on the vertical and radial V_θ profiles of different r_o will be investigated. Afterwards, the effect of variation of the S parameter on the vertical structure of the tornados is studied.

4.1. Swirl ratio corresponding to the Touchdown and $V_{\theta,max}$ for different r_o radii

Previous studies show that changing the r_o will affect the swirl ratios of tornado touchdown and the $V_{\theta,max}$. However, swirl ratios of touchdown and the $V_{\theta,max}$ are not investigated for different r_o. In this regard, the S parameter of touchdown is the S at which the tornado initially touches the ground, whereas the S of the $V_{\theta,max}$ is the S after touchdown which produces the highest intensity. Review of the previous laboratory and CFD tornado simulators in Tables 2.7 and 2.8 of the present study shows that the $V_{\theta,max}$ occurs at S value is in the range of 0.2 to 1.5. Therefore, the present study uses $0.2 \leq S \leq 1.5$ for each r_o to investigate their wind-fields Therefore, the swirl ratios that produce the touchdown and the $V_{\theta,max}$ are determined.

4.1.1. Simulation results

Figure 4.1 presents the S parameters corresponding to the touchdown and $V_{\theta,max}$ for various r_o radii. It can be seen in Figure 4.1 for r_o from $0.7km \leq r_o \leq 1.0km$, the touchdown occurs at S=0.40; for $r_o \geq 1.0km$ the touchdown S gradually increases from 0.4 to 0.7 at r_o=1.9km. Likewise, for $r_o \geq 2.0km$ the touchdown S is in the range of 0.7 to 0.9.

Figure 4.1 also shows the S values that correspond to the $V_{\theta,max}$ for different r_o radii. It can be seen in this figure that for $0.7km \leq r_o \leq 1.5km$, the $V_{\theta,max}$ occurs at almost $0.50 \leq S \leq 0.60$. Occurrence of the $V_{\theta,max}$ in this range was observed by Ishihara (2016) for a limited number of r_o radii. For $r_o \geq 1.5km$, the S value associated with $V_{\theta,max}$ increases with the r_o lengths and for r_o=2.3km the S of the $V_{\theta,max}$ is 1.3. Figure 4.1 also shows that the S of the $V_{\theta,max}$ is not similar to the touchdown S, rather it is larger than the touchdown S. In addition, this difference gradually increases after $r_o \geq 1.9km$. Using the information given in Figure 4.1, the $V_{\theta,max}$, r_c and z_{max} can be investigated.

4.1.2. Summary of findings

Simulation results show that by increasing the r_o, the S of touchdown and the S that produces the $V_{\theta,max}$ will increase. In addition, the S parameter producing the $V_{\theta,max}$ is larger than the touchdown S. In other words, the $V_{\theta,max}$ occurs beyond the touchdown.

4.1.3. Comparison of the results to the CFD and laboratory results

Figure 4.1 shows that for r_o=1.0km, the $V_{\theta,max}$ occurs at S=0.6. Lewellen et al. (1997) and Ishiahara et al. (2011), respectively, reported the S=0.60 and S=0.65 as the S value corresponding to the $V_{\theta,max}$. Therefore, the results of the present study for r_o=1.0km is in agreement with the previous studies. Similarly, findings of this section on the touchdown S of the tornados complies well with Lewellen et al. (1999) that suggested by increasing the r_o, the S that produces the $V_{\theta,max}$ is likely to increase. Likewise, Church et al. (1979) and Jischke and Parang (1974) reported the touchdown S equal to 0.5. Refan (2014), Refan and Hangan (2016) and Refan et al. (2017) reported the touchdown at approximately S=0.57. Also, the CFD model of Hangan and Kim (2008) reported that at S=0.4 the cell vortex breakdown is observed, and at S=0.7 touchdown completely occurs. However, they did not investigate any S value between 0.4 to 0.7, rendering that the touchdown S should be in the range of S=0.4 to S=0.7.

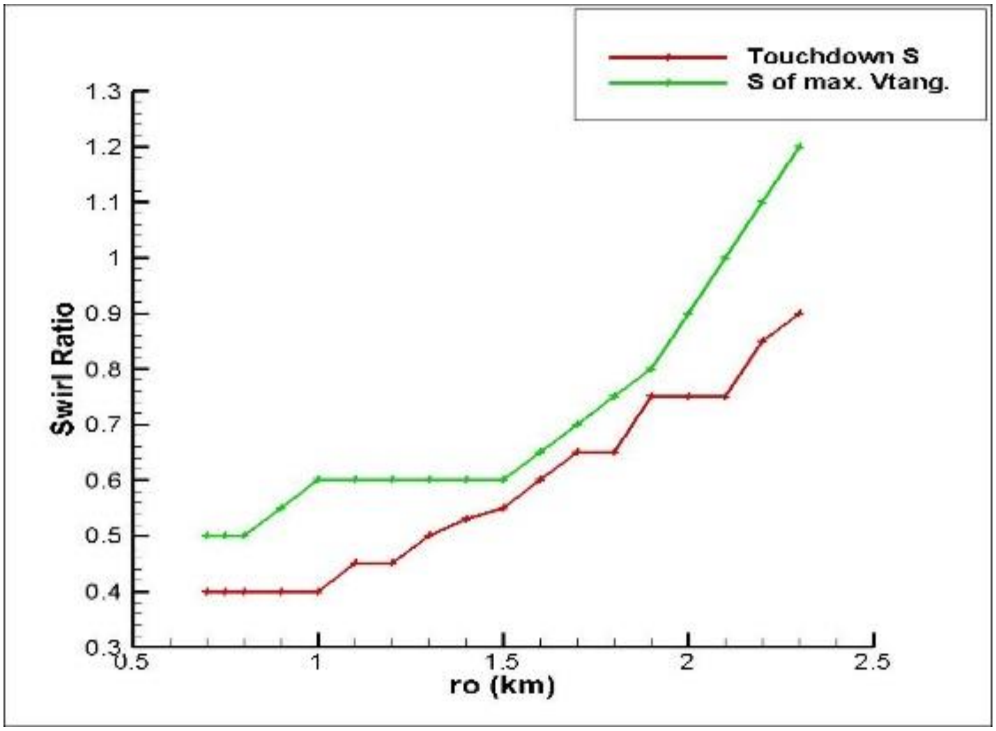

Figure 4.1. Swirl ratios corresponding to the touchdown and $V_{\theta,max}$ for 0.7km≤r_o≤2.3km

4.2. $V_{\theta,max}$, r_c and z_{max} for different r_o

In this chapter, the $V_{\theta,max}$, r_c and z_{max} of different tornado radii are reported using the S that produces the $V_{\theta,max}$. The S producing the $V_{\theta,max}$ was reported in Figure 4.1.

4.2.1. Absolute $V_{\theta,max}$ for various r_o

Figure 4.2 presents the absolute $V_{\theta,max}/V_{r\infty}$ for various tornado with 0.7km≤r_o≤2.3km. The $V_{\theta,max}/V_{r\infty}$ is yielded at the S parameter given in Figure 4.1. It can be seen in Figure 4.2 that the $V_{\theta,max}/V_{r\infty}$ occurs for r_o=0.7 (V_θ=6.53$V_{r\infty}$). However, by increasing r_o from 0.7km to 1.3km, the $V_{\theta,max}/V_{r\infty}$ gradually reduces and for r_o=1.3km, the $V_{\theta,max}$ is 4.05$V_{r\infty}$. For 1.4km≤r_o≤1.9km, the $V_{\theta,max}$ is almost 3.80$V_{r\infty}$, and for r_o>1.9km the $V_{\theta,max}$ again reduces to less than 3.50$V_{r\infty}$. So, it can be concluded that the $V_{\theta,max}/V_{r\infty}$ is significant for 0.7km≤r_o≤1.3km. Results of Figure 4.2 comply well with the previous studies. It can be seen in Figure 4.2 that for r_o=1.0km, the highest peak is $V_{\theta,max}$=4.98$V_{r\infty}$. Wilson and Rotunno (1986) reported $V_{\theta,max}$=5.0$V_{r\infty}$ for r_o=1.0km. In addition, Lewellen et al. (1997) reported the $V_{\theta,max}$=6.6 $V_{r\infty}$, which is in good agreement with the finding of the present study.

4.2.2. $V_{\theta,max}$ for various r_o radii at z=3.3m

As was stated in the first chapter, the V_θ at less than 10m AGL is not reported in the previous CFD or laboratory chamber models. The present section reports the $V_{\theta,max}/V_{r\infty}$ of different tornado radii at z=3.3m, which is the elevation of the typical buildings (Ishihara et al., 2011; Dominguez and Selvam, 2017). Figure 4.3 shows the $V_{\theta,max}/V_{r\infty}$ for various tornado radii at z=3.3m. It can be seen in Figure 4.3 that for r_o=0.7km, the $V_{\theta,max}$ is almost 2.5$V_{r\infty}$, while it constantly reduces to almost 1.0V_r for r_o=1.3km, and then reduces to almost 0.6$V_{r\infty}$ for $r_o \geq$2.1km. This finding implies that at z=3.3m, the effect of the intensity of the tornado reduces by increase of the tornado's r_o.

The reason of higher $V_{\theta,max}/V_{r\infty}$ for smaller r_o lies in the amount of energy transferred to the tornado. Wilson and Rotunno (1986) stated that in small r_o radii, a significant angular momentum will be carried to the smaller radii. This phenomenon is due to the narrowness of the swath of the tornado close to the ground for the smaller radii and thus the intensity is higher.

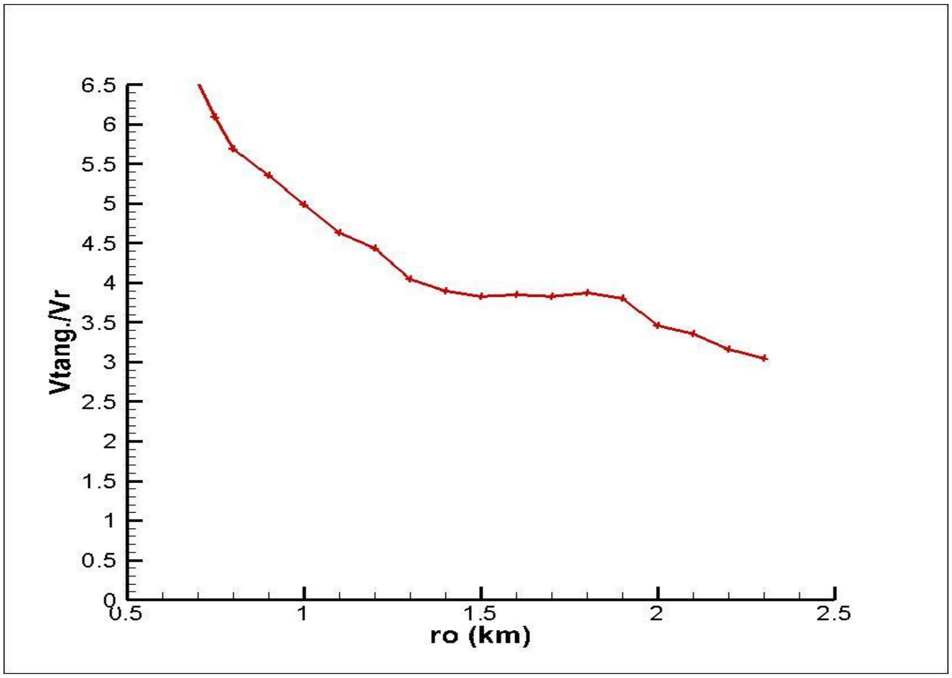

Figure 4.2. Absolute $V_{\theta,max}$ for different r_o radii ($V_{\theta,max}/V_{r\infty}$)

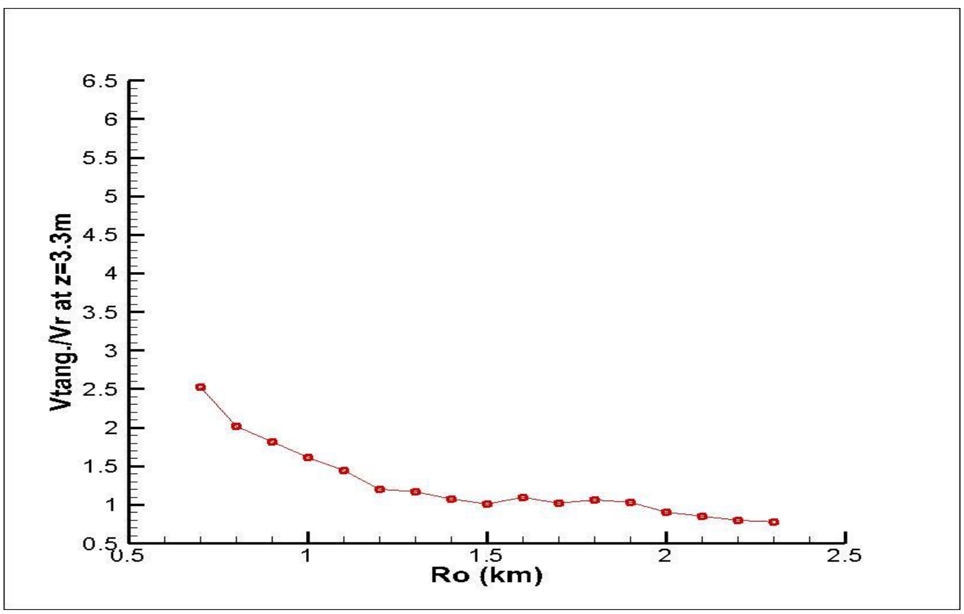

Figure 4.3. $V_{\theta,max}$ at z=3.3m for different r_o radii ($V_{\theta,max}/V_{r\infty}$)

4.2.3. Z_{max} for different r_o radii

Figure 4.4 shows the z_{max} for different r_o radii. It can be seen in the figure that by increasing the r_o, the z_{max} will also increase. However, for $r_o \geq 2.0$km, the z_{max} is constant at z_{max}=64m. This finding complies reasonably with the actual tornados. Wurman et al. (2013) reported z_{max}=27.5m with r_o=1.0km for Goshen Wyoming tornado of 2009. Figure 4.4 shows that for r_o=1.0km z_{max}=27m. Similarly, Hangan and Kim (2008) reported z_{max}=20m for Spencer tornado which had r_o=0.8km and Figure 4.4 shows that for r_o=0.8km, z_{max} is equal to 21m.

The reason of increase of z_{max} by increase of the r_o length is the outward expansion of the tornado vortex by increase of r_o. In general, the vortex column is narrow close to the ground, but at the top of the vortex column, the vortex column is wider (Lewellen et al., 1997; Wurman and Grill, 2000; Wurman and Alexander, 2005). This phenomenon was observed in the in-field study of the actual tornados (Bluestein et al., 2015; Bluestein and Pazmany, 2000). Simulations also show this outward expansion of the tornado column by increase of the r_o. Figure 4.5 compares the simulation results to the in-field measurements for the phenomenon.

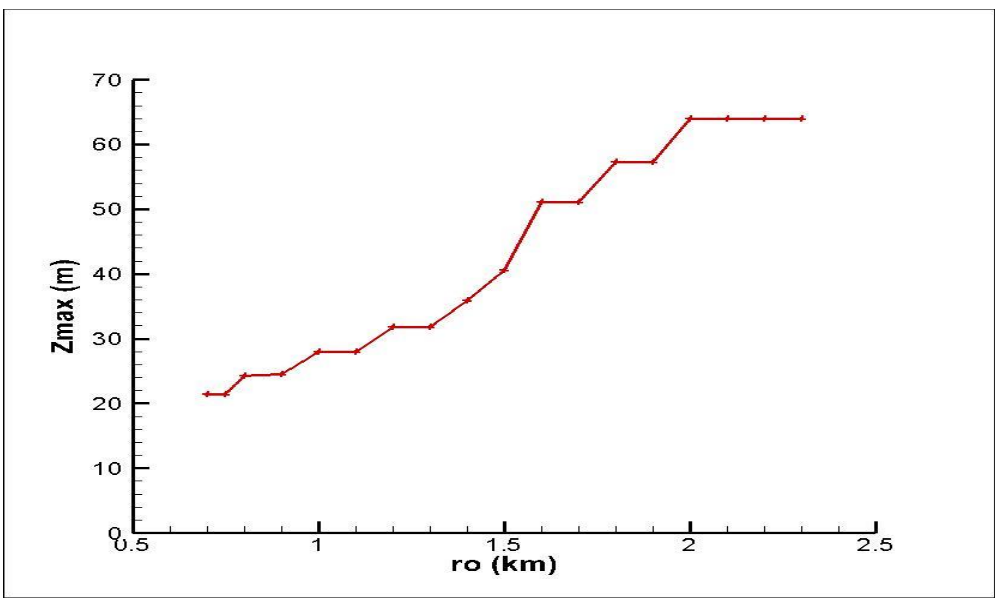

Figure 4.4. z_{max} for different r_o radii (m)

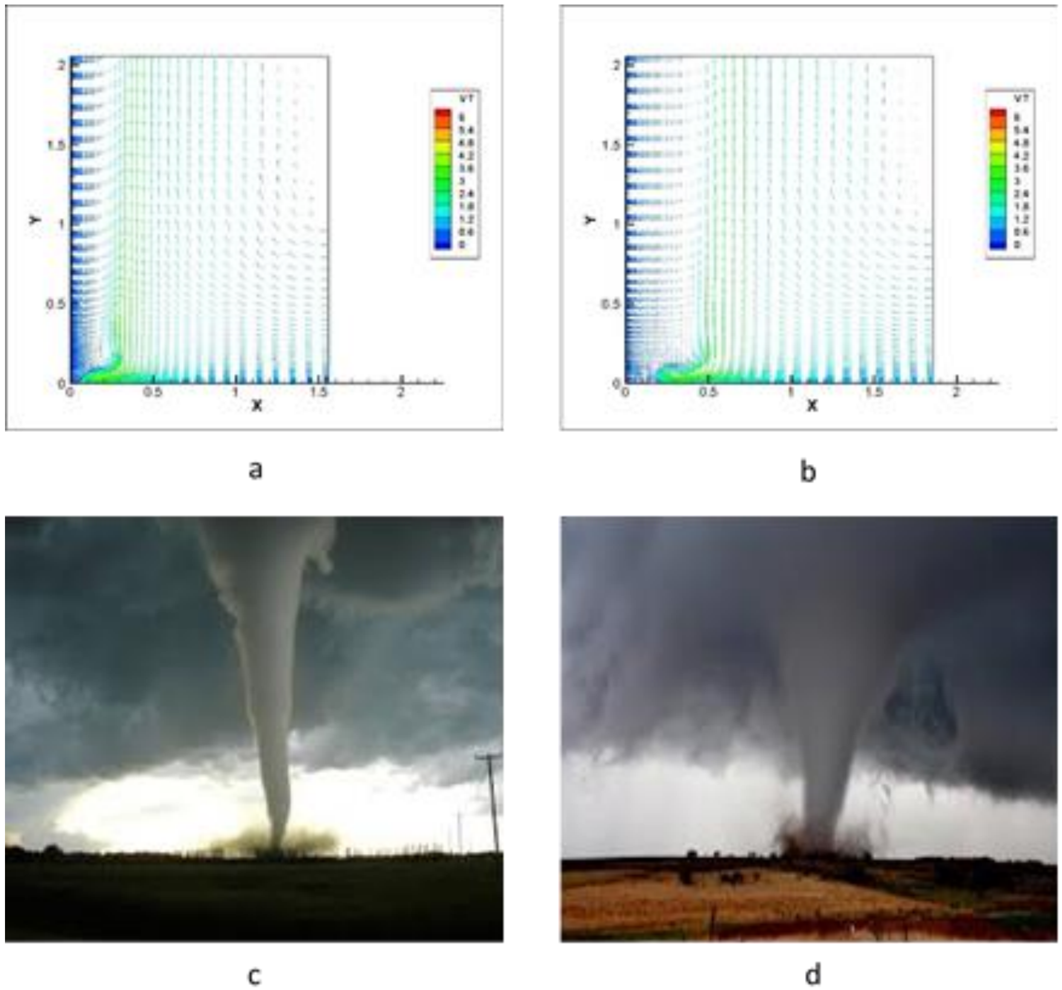

Figure 4.5. The outward expansion of tornados with larger r_o. a) r_o=1.5km; b) r_o=1.8km; c) actual tornado with small radius; d) actual tornado with large radius

4.2.4. Core radius (r_c) for different r_o

Figure 4.6 presents the r_c for different r_o. This figure shows the direct proportionality of the S to the r_c. It can be seen in Figure 4.6 that for 0.7km$\leq r_o \leq$1.8km, the r_c is in the range of almost 100m to 180m. However, for r_o>1.8km, by increasing the r_o, the r_c also expands from r_c=222m at r_o=1.9km to r_c=460m at r_o=2.3km.

Increase of the r_c with increase of the r_o is in agreement with experimental studies of Ward (1972), Davies-Jones (1973), Jischke and Parang (1974), Church et al. (1979), Church and Snow (1993), Baker and Church (1979), Tari et al (2010), Refan (2014), Refan et al. (2017), Refan and Hangan (2017). Likewise, Hangan and Kim (2008) reported the r_c at S=0.7 and S=1.0 to be, respectively, 90m and 220m. Table 4.1 summarizes findings of the swirl ratio of touchdown and swirl ratio of $V_{\theta,max}$, the absolute $V_{\theta,max}$, the $V_{\theta,max}$ at z=3.3m, z_{max}, and r_c.

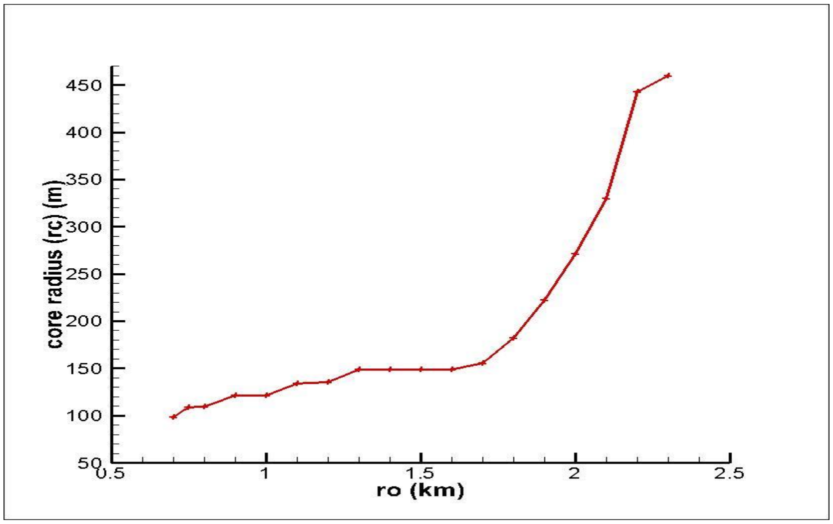

Figure 4.6. The core radius (r_c) for different r_o radii (m)

Table 4.1. Summary of the findings for different radii

r_o(km)	Touchdown S	S of $V_{\theta,max}$	Absolute $V_{\theta,max}/V_{r\infty}$	$V_{\theta,max}/V_{r\infty}$ at z=3.3	z_{max}(m)	r_c(m)
0.7	0.4	0.5	6.53	2.53	21.4	98.3
0.8	0.4	0.5	5.69	2.02	24.25	109.18
0.9	0.4	0.55	5.35	1.82	24.5	121.1
1	0.4	0.6	4.99	1.62	27.98	121.1
1.1	0.45	0.6	4.63	1.44	27.98	134.21
1.2	0.45	0.6	4.43	1.2	31.77	135.21
1.3	0.5	0.6	4.05	1.17	31.77	148.64
1.4	0.53	0.6	3.89	1.07	35.94	148.63
1.5	0.55	0.6	3.83	1.01	40.54	148.63
1.6	0.6	0.65	3.85	1.09	51.16	148.63
1.7	0.65	0.7	3.83	1.02	51.16	134.21
1.8	0.65	0.75	3.87	1.06	57.28	181.94
1.9	0.75	0.8	3.8	1.03	57.28	222.2
2	0.75	0.9	3.46	0.9	64	271.02
2.1	0.75	1	3.36	0.85	64	330
2.2	0.85	1.1	3.16	0.8	64	443
2.3	0.9	1.2	3.05	0.78	64	460

4.3. Effect of variation of the swirl ratio on the vertical V_θ profile

Identifying the vertical V_θ profile is essential for engineering purposes because this profile shows the $V_{\theta,max}$ and the z_{max} (Refan et al., 2017). Therefore, in this section, effect of variation of the S parameter on the vertical V_θ profile is investigated. The investigation is conducted for $0.2 \leq S \leq 1.5$ for different tornado radii and results are shown for r_o=0.8km, 1.0km, 1.5km and 2.0km.

4.3.1. Simulation results

Figure 4.7 shows the vertical V_θ profile for r_o=0.8km. The vertical V_θ profiles are shown at different r locations: r=33m, r=88m, r=r_c=110m and r=245m from the center of the tornado. Figure 4.7shows that the V_θ profile has always a conical shape and the $V_{\theta,max}$ always occurs at elevations less than 30m AGL for all S values. Moreover, Figure 4.7(a) shows that at r=33m from the center the $V_{\theta,max}$ is almost 5.5$V_{r\infty}$, and Figure 4.7(b) shows that at r=88m the $V_{\theta,max}$ is almost 5.8$V_{r\infty}$. At r=r_c=the $V_{\theta,max}$ is almost 6.1$V_{r\infty}$. 110m (Figure 4.7(c)). Also, Figure 4.7(d) shows that by moving farther from the r_c, at r=245m the $V_{\theta,max}$ decreases to less than 4.0$V_{r\infty}$. It implies that the $V_{\theta,max}$ occurs at the inner core of the tornado. In addition, Figure 4.7 shows that at all distances by increasing the S, the z_{max} descends towards the ground and minimizes at S greater than the touchdown S.

Similarly, Figure 4.8 shows the vertical V_θ profile for r_o=1.0km at: r=33m, r=88m, r=r_c=121m and r=245m from the center of the tornado. Figure 4.8 shows that the V_θ profile has always a conical shape and the $V_{\theta,max}$ always occurs at elevations less than 30m AGL for all S values. In addition, by increasing the S value, the z_{max} descends towards the ground. Moreover, Figure 4.8(a) shows that at r=33m from the center the $V_{\theta,max}$ is almost 1.6$V_{r\infty}$, and Figure 4.7(b) shows that at r=88m the $V_{\theta,max}$ is almost 4.5$V_{r\infty}$. At r=r_c=121m (Figure 4.7(c)) the $V_{\theta,max}$ is almost 4.9$V_{r\infty}$. Figure 4.7(d) shows that by moving farther from the r_c, at r=245m the $V_{\theta,max}$ decreases to less than $4.3V_{r\infty}$. It implies that the $V_{\theta,max}$ occurs at the inner core of the tornado.

In parallel, Figure 4.9 shows the vertical V_θ profile for r_o=1.5km at: r=33m, r=88m, r=r_c=148m and r=245m from the center of the tornado. Figure 4.9 shows that for all S values, the vertical V_θ profile has a conical shape with the $V_{\theta,max}$ at less than 50m AGL. In addition, by increasing the S value, the z_{max} descends towards the ground. Moreover, Figure 4.10(c) shows that the $V_{\theta,max}$ again peaks at r=r_c=148m and by moving away from the r_c, the $V_{\theta,max}$ will decrease. Therefore, the $V_{\theta,max}$ occurs at the inner core and the z_{max} occurs at the radial location corresponding to the r_c.

Figure 4.10 shows the vertical V_θ profile for r_o=2.0km at different r locations: r=50m, r=150m, r=r_c=271m and r=490m from the center of the tornado. Similar to the previous case, in this case it can be seen that the vertical V_θ profile has always a conical shape and the $V_{\theta,max}$ always occurs at around 60m AGL. Moreover, in this case again by increasing the S value, the z_{max} descends towards the ground. Furthermore, the $V_{\theta,max}$ is $3.5V_{r\infty}$ and occurs at r=r_c (Figure 4.10(c)). For this case also the $V_{\theta,max}$ occurs at the inner core and the z_{max} occurs at the radial location corresponding to the r_c.

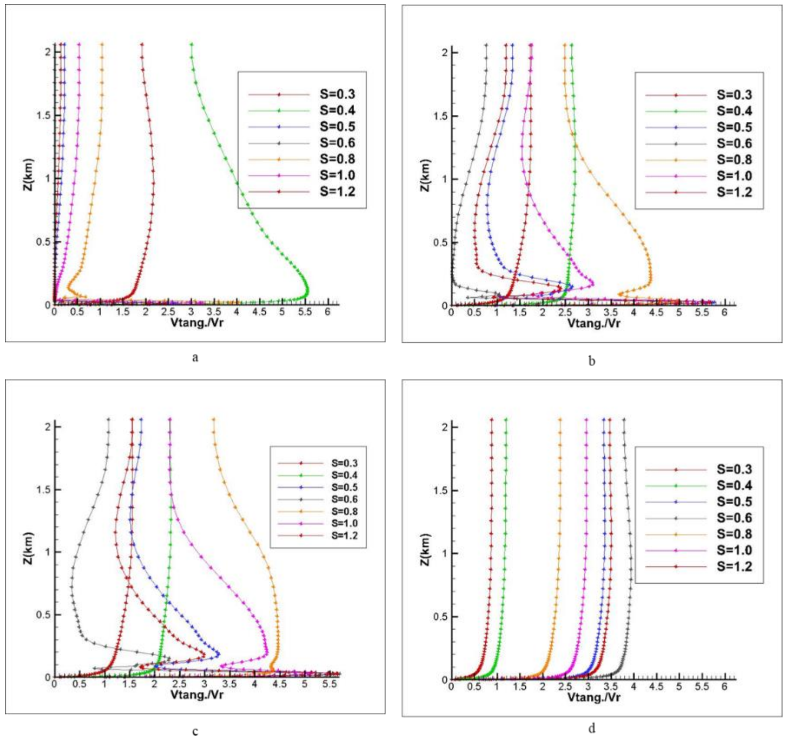

Figure 4.7. Vertical V_θ profile of different swirl ratios for r_o=0.8km. a) r=33m; b) r=88m; c) r=r_c=110m; d) r=245m

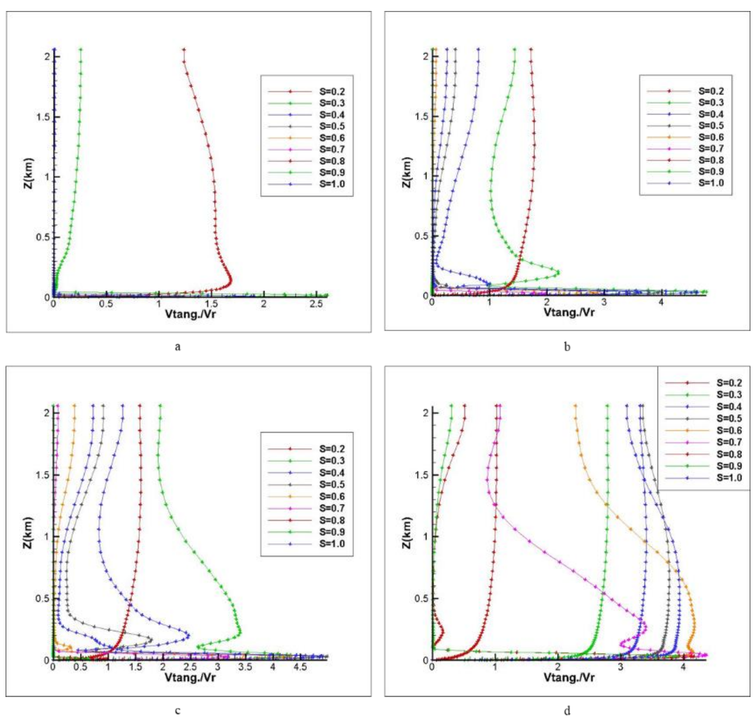

Figure 4.8. Vertical V_θ profile of different swirl ratios for r_o=1.0km. a) r=33; b) r=88; c) r=r_c=121m; d) r=245m

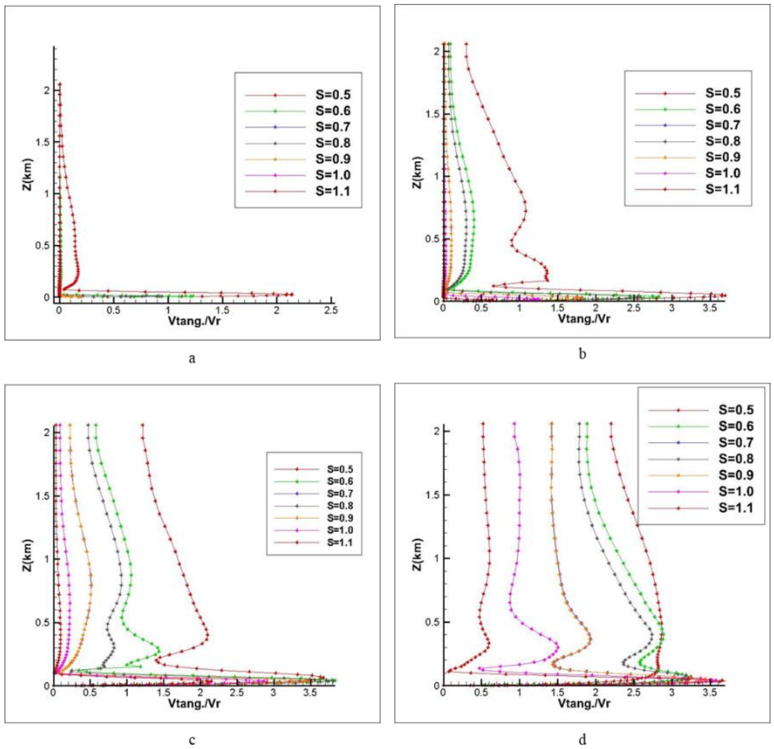

Figure 4.9. Vertical V_θ profile of different swirl ratios for r_o=1.5km. a) r=33; b) r=88m; c) $r=r_c$=148m; d) r=245m

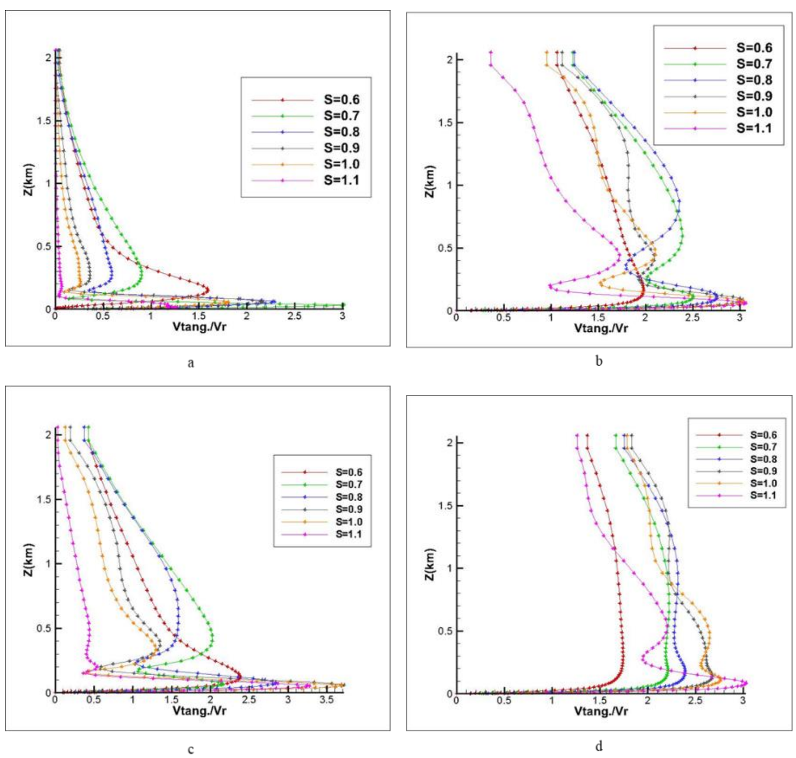

Figure 4.10. Vertical V_θ profile of different swirl ratios for r_o=2.0km. a) r=50; b) r=150m; c) $r=r_c$=271m; d) r=490m

4.3.2. Summary of findings

Investigation of the vertical V_θ profiles shows that for all radii, the vertical V_θ profile has a conical shape, where the location of the $V_{\theta,max}$ is close to the ground and descends towards the surface by increasing the S parameter. These close-to-ground maxima is always in the range of 21m to 64m of the ground and differentiates tornadic flows from the SL flows. In addition, the $V_{\theta,max}$ and the z_{max} always occur within the inner core of the tornado.

4.3.3. Comparison of the results to the laboratory and radar measurements

Tari et al. (2010) showed that by increasing the S parameter, the z_{max} descends towards the ground. They also reported the vertical V_θ profile has a conical shape and the nose-like peak occurs at the swirl ratio of the $V_{\theta,max}$. However, their laboratory simulator was not capable of reporting at less than 20m AGL. Refan (2014) also showed that the vertical V_θ profile has a conical shape, but reported the z_{max} in the range of 30 to almost 200m AGL. In addition, Doppler radar measurements of Wurman et al. (1997) showed that the $V_{\theta,max}$ occurs close to the ground at around 30m AGL. However, they were not able to evaluate for less than 30m AGL.

4.4. Effect of variation of the swirl ratio on the radial V_θ profile

The radial V_θ profile will provide information of the $V_{\theta,max}$, and changing the S parameter changes the V_θ profile (Refan, 2014). In addition, the radial V_θ profile can provide the $V_{\theta,max}$ at any elevation. Thus, in this section effect of variation of the S parameter on the radial V_θ profile is investigated. The investigation is conducted for $0.2 \leq S \leq 1.5$ on $0.7km \leq r_o \leq 2.3km$. For the sake of brevity, the radial V_θ profiles of r_o=0.8km, r_o=1.0km, r_o=1.7km, r_o=1.8km and r_o=2.0km are shown only. Figures 4.11 to 4.15 show the radial V_θ profiles for the these r_o radii at elevations z=51m, 18.5m, 9.5m, and 4.5m.

4.4.1. Simulation results

4.4.1.1. Pattern of the radial V_θ profile

Figure 4.11 shows the V_θ profile for r_o=0.8km at different heights. Based on Figure 4.1 swirl ratios of touchdown and the $V_{\theta,max}$ for r_o=0.8km are S=0.4 and 0.5, respectively. Figures 4.11(a) and 4.11(b) show that at z=51m and z=18.5m the radial V_θ profiles resemble the RCVM profile at different S values. Figures 4.11(c) and 4.11(b) show the radial V_θ profiles at z=9.5m and z=4.5m, respectively. As can be seen in these figures, at these elevations the V_θ profile for S values beyond the touchdown S no longer resemble the RCVM flow, rather two peaks occur on the profile. However, for S values smaller than the touchdown S, the profiles still resemble the RCVM. Therefore, tit can be concluded for r_o=0.8km two peak occurs at z<10m AGL for S values beyond the touchdown S.

Figure 4.12 shows the V_θ profile for r_o=1.0km at different heights. Based on Figure 4.1 swirl ratios of touchdown and the $V_{\theta,max}$ for r_o=1.0km are S=0.4 and 0.6, respectively. Figures 4.12(a) and 4.12(b) show that at z=51m and z=18.5m the profiles have a trend similar to RCVM flow for different S values. Figures 4.12(c) and 4.12(d) show the radial V_θ profiles at z=9.5m and z=4.5m, respectively. It can be seen that at these elevations the V_θ profiles no longer resemble the RCVM flow, rather two peaks occur on the profiles for S values beyond the touchdown S. However, for S values smaller than the touchdown the profiles resemble the RCVM profile. Therefore, it can be concluded that for r_o=1.0km at S of touchdown and beyond that, two peaks occur at z<10m AGL.

Figure 4.13 shows the V_θ profile for r_o=1.7km at different heights. Based on Figure 4.1 swirl ratios of touchdown and the $V_{\theta,max}$ for r_o=1.7km are S=0.65 and S=0.7, respectively. Figure 4.13(a) shows that at z=51m, the radial V_θ profiles resemble the RCVM flow for all S values. Figure 4.13(b) shows the radial V_θ profiles at z=18.5m. At this elevation, the profile has two peaks for S greater than the touchdown S, and no longer resembles the RCVM profile. Similarly, Figures 4.13(c) and 4.13(d) respectively show the profiles at z=9.5m and 4.5m. It can be seen that at these elevations the profiles have two peaks for S beyond the touchdown S (S=0.65). Therefore, simulation results for r_o=1.7km show that at z<20m the V_θ profile has two peaks, whereas for z>20 the profile resembles the RCVM flow.

Figure 4.14 shows the V_θ profile for r_o=1.8km at different heights and various S values. Based on Figure 4.1 swirl ratios of touchdown and the $V_{\theta,max}$ for r_o=1.8km occurs at S=0.65 and S=0.75, respectively. Figure 4.14 shows that at different elevations of z=51m, z=18.5m, z=9.5m and z=4.5m the radial V_θ profiles have two peaks for S values beyond the touchdown S. Therefore, for r_o=1.8km two peaks always occur at all elevations for the S values beyond touchdown.

Similarly, Figure 4.15 shows the V_θ profile for r_o=2.0km at different heights and various S values. Based on Figure 4.1 swirl ratios of touchdown and the $V_{\theta,max}$ for r_o=2.0km are 0.75 and 0.9, respectively. Figure 4.15 shows that at different elevations of z=51m, z=18.5m, z=9.5m and z=4.5m the radial V_θ profiles have two peaks for S values beyond the touchdown S. Therefore, for r_o=2.0km two peaks always occur at all elevations for the S values beyond touchdown.

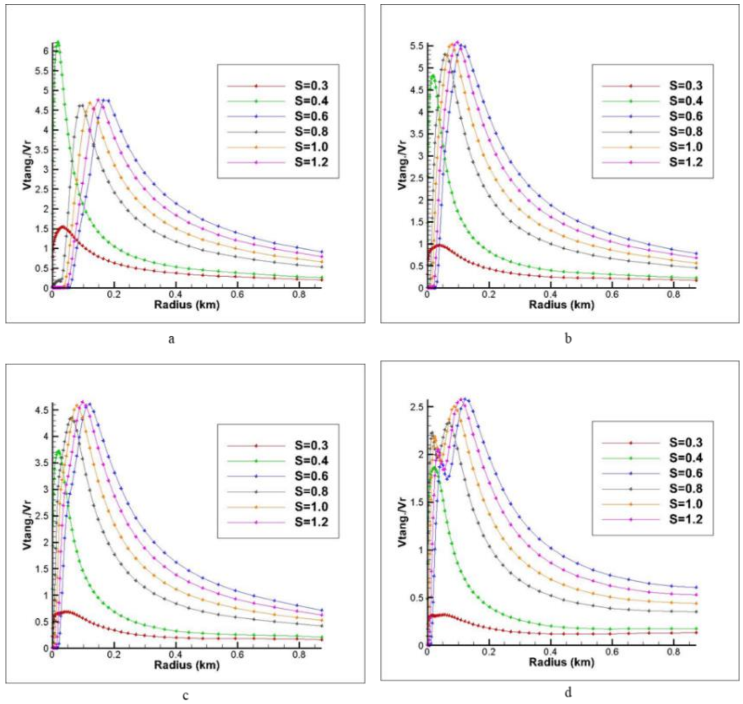

Figure 4.11. Radial V_θ profile of different swirl ratios for r_o=0.8km. a) z=51m; b) z=18.5m; c) z=9.5m; d) z=4.5m

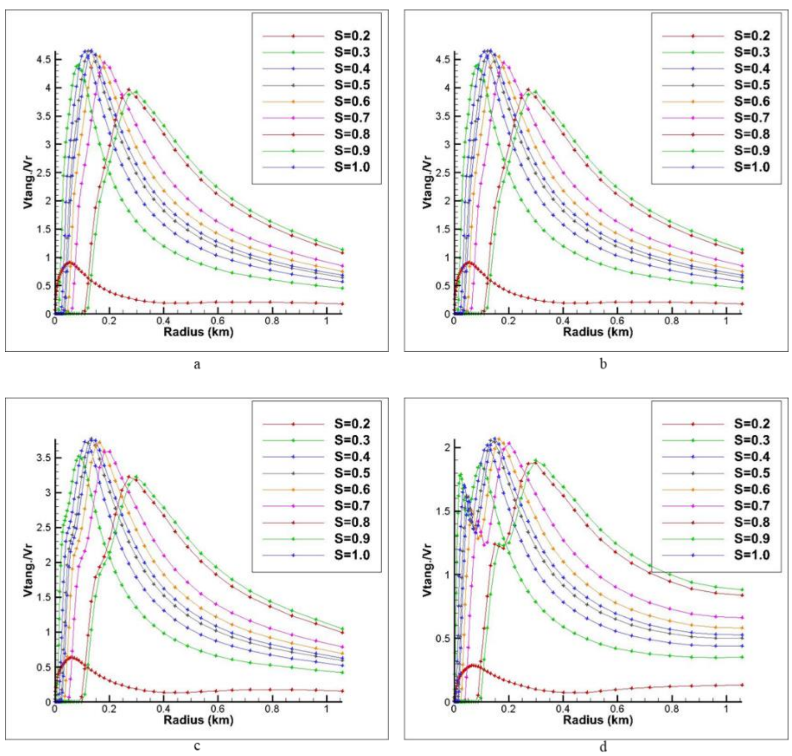

Figure 4.12. Radial V_θ profile of different swirl ratios for r_o=1.0km. a) z=51m; b) z=18.5m; c) z=9.5m; d) z=4.5m

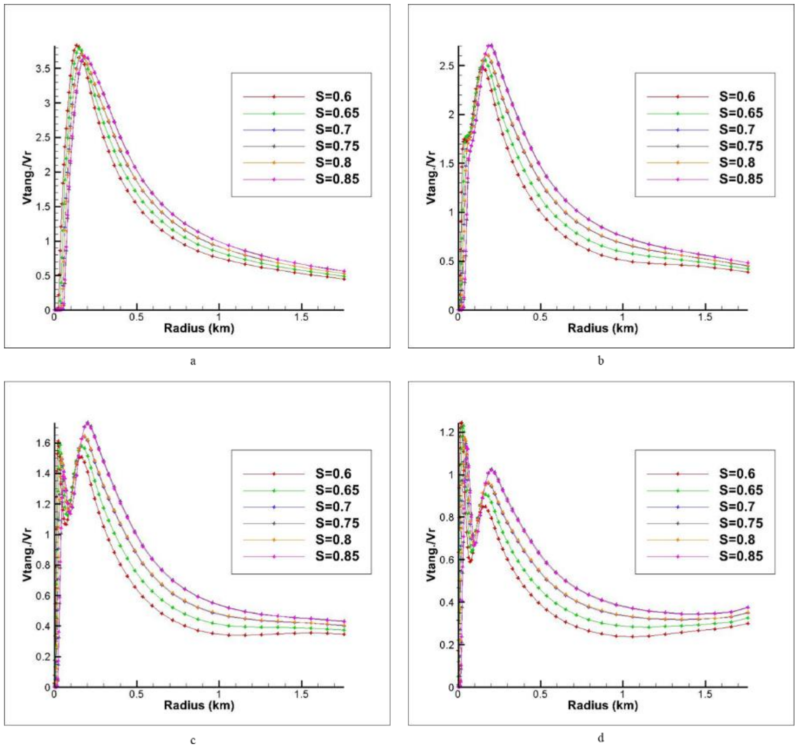

Figure 4.13. Radial V_θ profile of different swirl ratios for r_o=1.7km. a) z=51m; b) z=18.5m; c) z=9.5m; d) z=4.5m

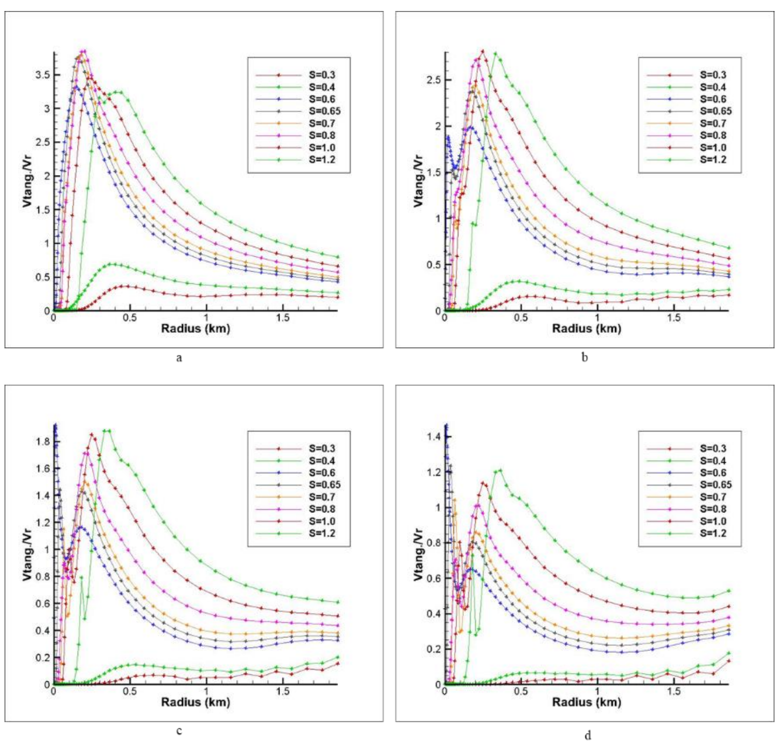

Figure 4.14. Radial V_θ profile of different swirl ratios for r_o=1.8km. a) z=51m; b) z=18.5m; c) z=9.5m; d) z=4.5m

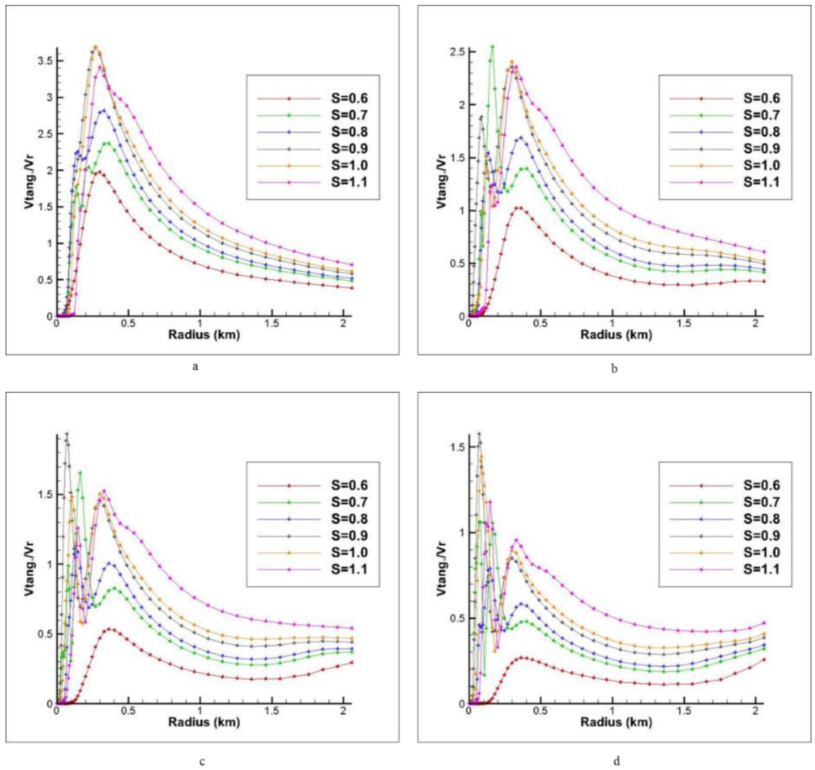

Figure 4.15. Radial V_θ profile of different swirl ratios for r_o=2.0km. a) z=51m; b) z=18.5m; c) z=9.5m; d) z=4.5m

4.4.1.2. Location of occurrence of peaks on the profile

Figure 4.16 represents the occurrence of two peaks on the V_θ profile of the tornados with r_o=0.8km, r_o=1.0km, r_o=1.5km, r_o=2.0km at z=4.5m. Profiles are shown at the S parameter that produces the $V_{\theta,max}$. Figure 4.16(a) shows that for r_o=0.8km, the first peak occurs at almost 35m from the tornado center and r_c is 110m (Figure 4.6). Similarly, Figure 4.16(b) shows that r_o=1.0km the first peak occurs at almost 40m away from the center while the r_c is 121m (Figure 4.6). Also, Figure 4.16(c) shows that for r_o=1.5km the first peak is almost 50m from the tornado center where r_c is 148m. Finally, Figure 4.16(d) shows that for r_o=2.0km the first peak occurs almost 200m away from the center whereas the r_c is 271m. Therefore, it can be concluded that for different r_o tornados, the first peak occurs within the inner core.

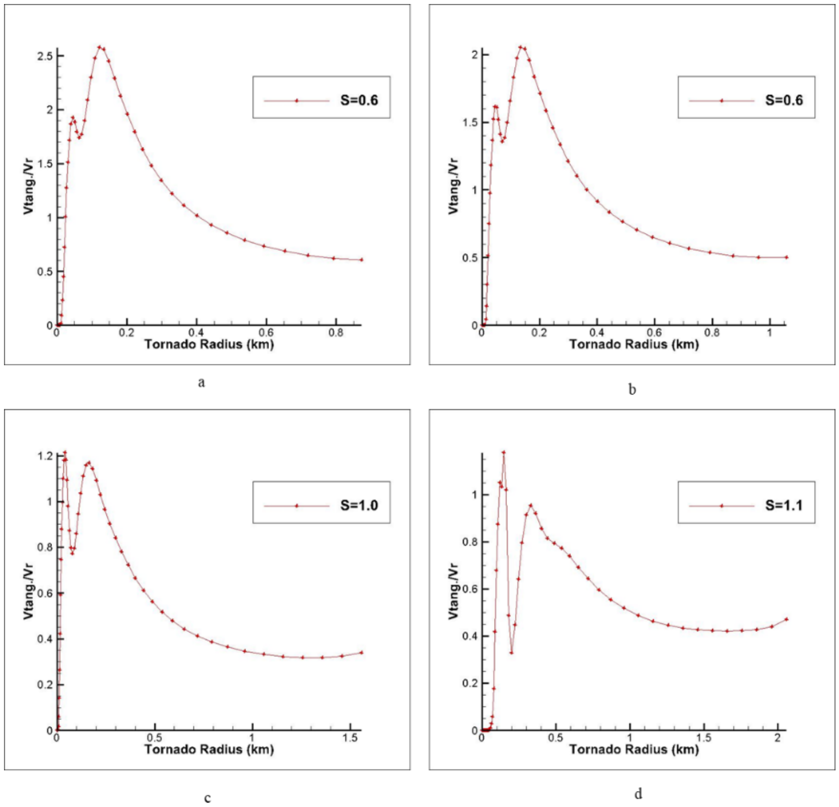

Figure 4.16. Tangential velocity profiles at z=4.5m and the S corresponding to double-peak. a) r_o=0.8km; b) r_o=1.0km; c) r_o=1.5km; d) r_o=2.0km. It can be seen that for larger radii, higher S is required to observe the double-peak.

4.4.2. Summary of findings

Figures 4.11 through 4.15 show that for ro≤1.6km, the radial V_θ profiles resemble the RCVM profile at z>10m AGL before and after the touchdown; whereas for z≤10m they have a different profile with two peaks on it after the touchdown. Similarly, for ro≥1.8 the radial V_θ profiles always have two peaks after the touchdown at all elevations. Occurrence of two peaks on the profile can be related to the strong shear force close to the ground, which causes increased intensity of the wider tornados despite their smaller $V_{\theta,max}/V_{r\infty}$ than smaller tornados.

4.4.3. Comparison of the results to the laboratory and CFD models

Figure 4.12 shows that for r_o=1.0km, the velocity profiles at z=51m and 18.5m resemble the RCVM profile. This finding is in agreement with the findings of Lewellen et al. (1997) which reported that the V_θ profile for r_o=1.0km follows the RCVM trend. Likewise, Refan (2014) reported occurrence of two peaks on the radial V_θ profile for S>1.0, but did not discuss the elevation and the ro for which this two peak occurs. Moreover, Refan (2014) did not discuss any reason for this observation. Church et al. (1979) used a laboratory tornado simulator and showed that the tornado velocity profile has two peaks close to the ground; however, this profile was not the V_θ profile, rather it was the magnitude of the velocity profile. They attributed this observation to the strong shear force close to the ground.

4.5. Effect of the swirl ratio on the vertical structure of the tornados

Tari et al. (2010) and Refan (2014) showed that changing the S parameter will change the structure of the tornados from a single-cell to a double-cell structure. Hangan and Kim (2008), Refan (2014), Refan et al. (2017) stated that before the touchdown, the tornado has a jet-like structure, during the touchdown a vortex breakdown occurs aloft, and in transition to the double-cell, the $V_{\theta,max}$ occurs. Figure 2.3 shows the vertical structure of tornados as proposed by Lewellen (1976). In the present section, the simulation results for the vertical structures of the tornados are investigated. For this purpose, the vertical structures are shown for r_o=0.8k, r_o=1.0km, r_o=1.5km and r_o=1.8km. The S that produces the $V_{\theta,max}$ for each of these r_o are taken from Figure 4.10. It can be implied form Figure 4.10 that at S=0.3, there is no touchdown for any r_o.

4.5.1. Simulations results

Figure 4.17 shows the tornado wind-field for r_o=0.8km at S=0.3, S=0.5, and S=0.8. The S=0.5 is taken from Figure 4.10. Figure 4.17(a) shows the wind-field at S=0.3. It can be seen in this figure that the flow is jet-like with no downdraft. This structure is similar to the structure shown by Lewellen (1976) for a single-cell structure. Figure 4.17(b) shows that by increasing the S to S=0.5, which is the touchdown S, the vortex breakdown occurs aloft. Afterwards at S=0.6, which is the S producing the $V_{\theta,max}$, the tornado transitions from single-cell structure to double-cell structure (Figure 4.17(c)). The vortex breakdown aloft at the touchdown and the transition at the S producing the $V_{\theta,max}$ agree well with the proposed structures by Lewellen (1976) as shown in Figures 2.3(b) and 2.3(c), respectively.

Figure 4.18 shows the tornado wind-field for r_o=1.5km at S=0.3, S=0.5, and S=0.6. The S parameters of 0.5 and 0.6 are taken from Figure 4.10, which are, respectively, the touchdown S and the S producing the $V_{\theta,max}$. Figure 4.19(a) shows the wind-field at S=0.3. It can be seen in this figure that with S=0.3 the flow is jet-like with no downdraft, which is similar to the single-cell structure proposed by Lewellen (1976), as shown in Figure 2.3(a). Figure 4.19(b) shows that by increase of the S to S=0.5, which is the touchdown S, the vortex breakdown occurs aloft, and afterwards at S=0.6, which is the S producing the $V_{\theta,max}$, the tornado transitions from single-cell structure to double-cell structure (Figure 4.19(c)). The vortex breakdown aloft at the touchdown and the transition at the S producing the $V_{\theta,max}$ agree well with Figures 2.3(b) and 2.3(c), respectively.

Figure 4.19 shows the tornado wind-field for r_o=2.0km at S=0.3, S=0.65, and S=0.75. The two latter values are, respectively, the touchdown S and the S producing the $V_{\theta,max}$ taken from Figure 4.10. Again, it can be seen in Figure 4.20(a) that at S=0.3, the flow is jet-like with no downdraft, which is similar to the single-cell structure proposed by Lewellen (1976), as shown in Figure 2.3(a). Figure 4.20(b) shows that by increase of the S to S=0.5, which is the touchdown S, the vortex breakdown occurs aloft, and afterwards at S=0.6, which is the S producing the $V_{\theta,max}$, the tornado transitions from single-cell structure to double-cell structure (Figure 4.20(c)). The vortex breakdown aloft at the touchdown and the transition at the S producing the $V_{\theta,max}$ agree well with Figures 2.3(b) and 2.3(c), respectively.

The reason that the double-cell structure occurs is the large outward centrifugal force which is produced due to increase of the S parameter (Davis-Jones, 1973; Haan et al., 2008). Hence, it can be implied that for transitioning from a single-cell to a double-cell tornado, more energy is required. In other words, since the S parameter is the ratio of the angular momentum to the radial momentum, therefore the wider tornados require more momentum and energy to have transition from single-cell to double-cell tornados after the touchdown.

4.5.2. Summary of findings

Simulations show that by increase of the S, flow changes from a single-celled to a vortex breakdown aloft at the touchdown stage, and finally to a double-celled structure at the S producing the $V_{\theta max}$.

4.5.3. Comparison of the results to the CFD and laboratory models

Hangan and Kim (2008) reported that for r_o=1.0km, variation of the S parameter from 0.28 to 0.8 covers the main stages of the tornado genesis from the formation of a laminar core vortex, the aloft vortex break down to the touchdown of the turbulent vortex. Also, Refan et al. (2017) reported 0.8<S<1.4 as the range of producing the double-celled tornados for the tornado radii of 0.2km to 2.0km. Dominguez and Selvam (2017) stated that for r_o=1.0km at S=0.3, the flow is jet-like and no touchdown occurs, whereas the touchdown S and S of $V_{\theta,max}$ are, respectively, 0.4 and 0.6. Refan (2014) stated that for S=0.96, the structure of tornados is double-celled. Therefore, the simulations of the vertical structure of the tornados in the present study agree well with the previous studies.

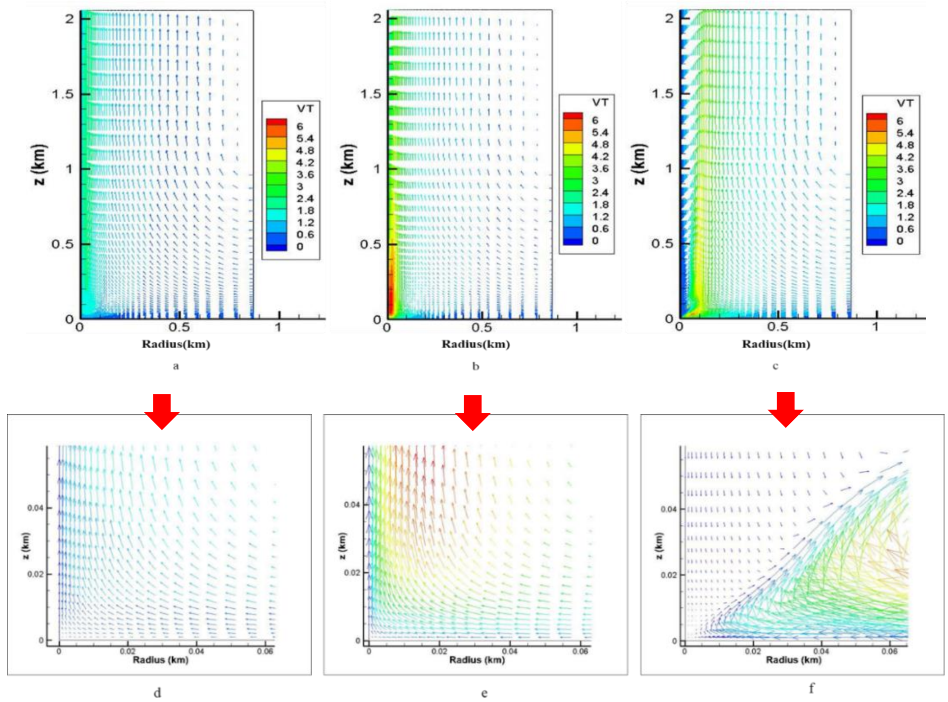

Figure 4.17. Tornado wind field for r_o=0.8km. a) S=0.3, jet-like and single-cell structure; b) S=0.4, vortex breakdown aloft at touchdown; c) S=0.5, beyond touchdown, double-cell structure; d) zoomed view of single-cell structure; e) zoomed view of vortex breakdown aloft; f) zoomed view of double cell structure

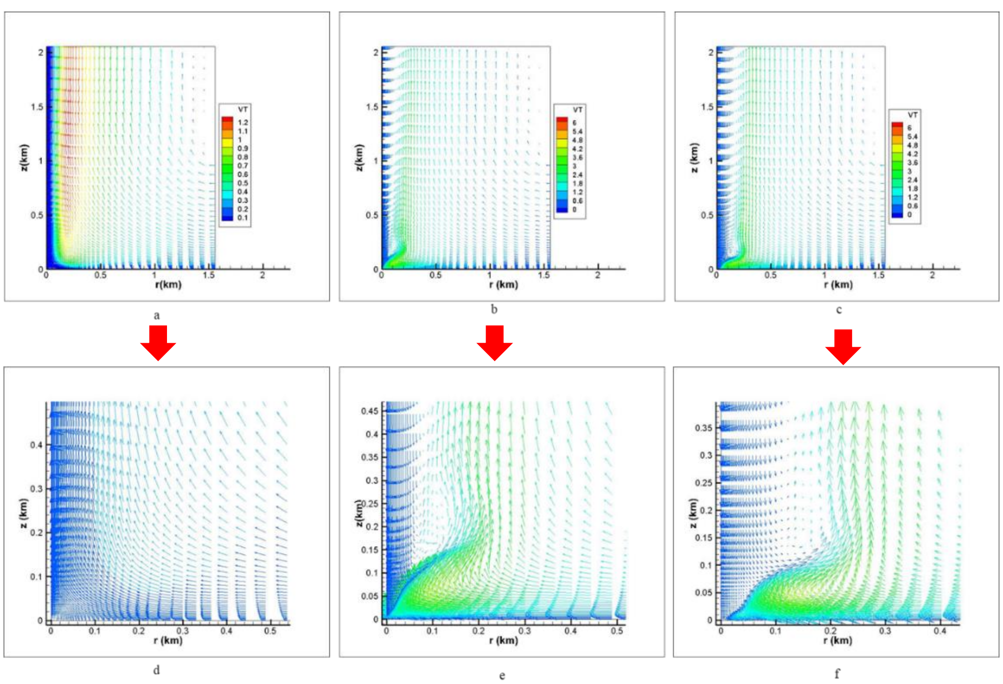

Figure 4.18. tornado wind field for ro=1.5 km. a) S=0.3, jet-like and single-cell structure; b) S=0.50: touchdown, vortex breakdown aloft; c) S=0.6: double-cell structure; d) zoomed view of single-cell structure; e) zoomed view of vortex breakdown aloft; f) zoomed view of double cell structure

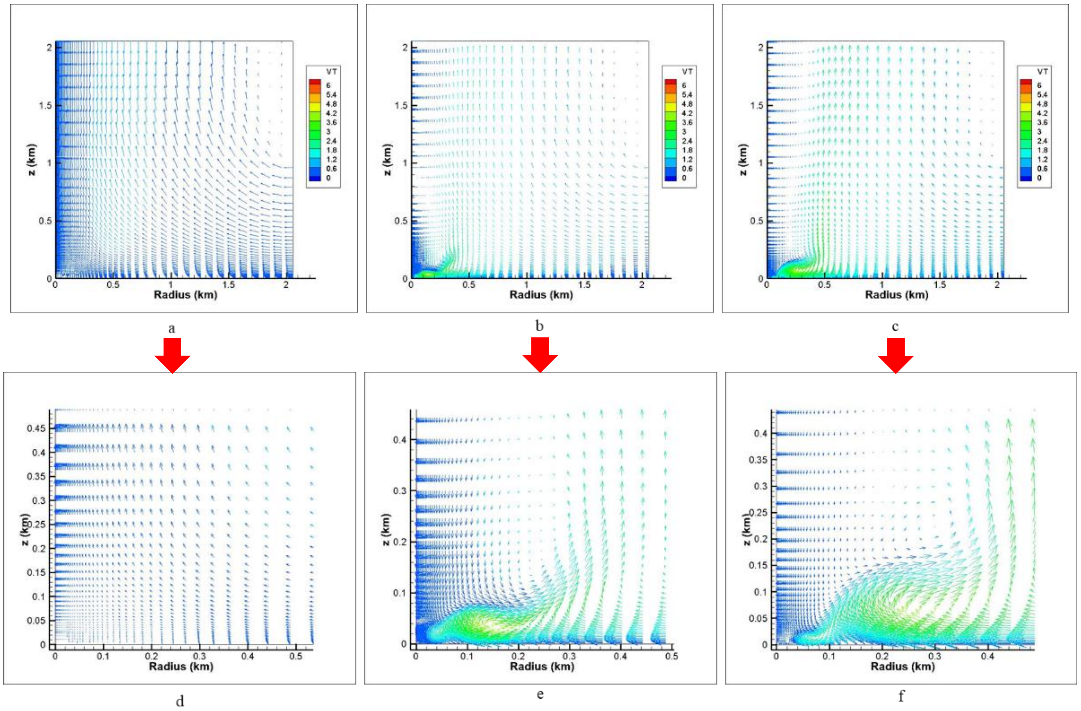

Figure 4.19. Tornado wind field for r_o=2.0km. a) S=0.3, jet-like and single-cell structure; b) S=0.75, vortex breakdown aloft at touchdown; c) S=0.9, beyond touchdown, double-cell structure; d) zoomed view of single-cell structure; e) zoomed view of vortex breakdown aloft; f) zoomed view of double cell structure

4.5.4. Comparison of the simulation results to the laboratory and radar measurements

Hangan and Kim (2008) used a laboratory model and stated that the 1998 Spencer tornado with r_o=0.8km is a double-celled tornado. In addition, Lee and Samaras (2004) used Doppler radar and reported a double-cell structure for the 2003 Manchester tornado with r_o=0.8km. Similarly, Wakimoto et al (2016) used Doppler radar and showed that the 2013 El Reno tornado with r_o=2.3km, are double-celled tornados. Results of the present study in Figures 4.10 and 4.13 show that after the touchdown, the r_c=110m for r_o=0.8km and for r_o=2.3km, the r_c is 460m, and are therefore double-celled. It can be implied that the simulation produces acceptable results compared to the radar measurements.

4.6. Verification of the simulation results against the radar measurements

In this section, the simulation results will be verified against the radar measurements of the actual data. As discussed in Chapter 3, the verification criteria are: the vertical tornado structure, r_c and z_{max}. The radar measurements of 6 actual tornados on their structure, r_c and z_{max} are available, as shown in Table 4.3.

Comparison of the structure of the tornados in Table 4.3 shows that for all 6 cases, the structures match at both simulations and radar measurements. Also, comparison of the r_c from the radar and simulation results in Table 4.3 shows that the simulation and radar reasonably agree in cases of Spencer and Manchester tornados. However, for cases of El Reno and Bridge, Creek, Moore tornados, the simulations report smaller r_c than the radar measurements. This discrepancy is due to the debris effect in the radar measurements (Kosiba and Wurman, 2010) which causes the radars measure higher values for the r_c.

Also, Table 4.3 shows z_{max} of the actual tornados by radar and simulations. The z_{max} by radar is reported for Spencer, Manchester, and Goshen Wyoming tornados, and the simulation results for z_{max} of these three tornados agree closely with the radar measurements. However, for the 1999 Dimmit TX, the 2013 El Reno and the 1999 Bridge Creek Moore tornados the z_{max} from the Doppler radar are not available. Refan et al. (2017) stated that if two sailing criteria meet in comparison of the simulations to the radar measurements, then the simulations are reliable. Therefore, since the structure and the r_c of the simulations for these three tornados comply with the radar data, it can be claimed that the simulations in the present study are valid.

Likewise, Figures 4.20 through 4.22 compares the radial V_θ profile of the actual tornados to the simulation results. Figures 4.20 through 4.22, respectively, represent the 1995 Dimmit, Texas, 1998 Spencer, and 2003 Manchester tornados. Comparisons show that the simulation results resemble the RCVM profile, as do the radar measurements. In addition, the r_c from both simulations and radar measurements fairly agree with each other.

Verification of the simulation results for the vertical structure, r_c, z_{max} and the radial V_θ profiles of tornados shows close agreement of simulations with the radar measurements.

Table 4.2. Comparison of the vertical structure, r_c and z_{max} of radar measurements to simulations

Tornado	r_o (km)	Technique	Structure	r_c(m)	Z_{max}(m)
Spencer (1998)	0.8	Doppler radar (Wurman et al., 1998)	Double-celled	120	20
		Simulation results	Double-celled	109	21.4
Manchester (2003)	0.8	Doppler radar (Sarkar and Gallus, 2010)	Double-celled	130	20
		Simulation results	Double-celled	109	21.4
Goshen, Wyoming (2009)	1.0	Doppler radar (Wurman et al.2013)	Double-celled	140	30
		Simulation results	Double-celled	121	27.5
Dimmit, Texas (1999)	1.0	Doppler radar (Wurman and Gill, 2000)	Double-celled	150	NA
		Simulation results	Double-celled	121	27.5
El Reno (2013)	2.3	Doppler radar (Bluestein et al, 2015; Wakimoto et al. 2016)	Double-celled	650	NA
		Simulation results	Double-celled	500	65
Bridge Creek Moore(1999)	0.8	Doppler radar (Burgess et al., 2002)	Double-celled	175	NA
		Simulation results	Double-celled	110	21.4

4.7. Summary of the chapter

In this chapter, the S values corresponding to the touchdown and the $V_{\theta,max}$ were initially investigated. Afterwards, the absolute $V_{\theta,max}$ and the $V_{\theta,max}$ at z=3.3 were investigated. In addition, the z_{max} and the rc for different ro radii were reported. Subsequently, the effect of variation of the S parameter on the radial and vertical V_{θ} profiles and the structure of the tornados were investigated. It was found that the $V_{\theta,max}$ always occurs at 21m<z<64m. In addition, it was observed that for $r_o \leq 1.8$km the radial V_{θ} profiles at z>10m are similar to the RCVM flow, and at z<10m the profile has two peaks. In addition, for $r_o \geq 1.8$km, the radial V_{θ} profiles always have two peaks. Occurrence of double peaks on the V_{θ} profiles is due to strong shear forces and is the main cause of the building damages.

CHAPTER 5. SUMMARY AND CONCLUSIONS

In this chapter, a summary of the study is initially reviewed and the finding and conclusions are presented.

5.1. Summary of the study

In the literature review it was revealed that the V_θ component is the main velocity component of tornadic flows that exerts forces to buildings. Therefore, it is necessary to evaluate the V_θ profile of tornados in order to design tornado-resistant buildings. However, it was revealed that the in-field measurements, such as the Doppler Radar, suffer from limitations of their beams, and cannot evaluate the V_θ profiles for less than 20m AGL. In parallel, the post-damage investigations are capable of relating the tornado damages to its maximum velocity, but cannot evaluate the V_θ profile. The satellite based measurements also suffer from the same shortcomings and thus are not capable of evaluating the V_θ profile close to the ground. Because of the shortcomings of the in-field measurements and post-damage investigations, the experimental TVCs were built in order to model to the tornados in laboratory. The laboratory TVCs advanced the tornado-related studies by showing that in modeling the tornados there are two parameters that must be investigated in order to evaluate the V_θ profile: S and r_o parameters. However, laboratory TVCs suffer from scaling limits and cannot evaluate the V_θ profile at less than 10m AGL. The CFD models can computationally simulate the TVCs and evaluated the V_θ profile close to the ground, but the results of the CFD models is limited to r_o=1.0km, while the actual tornados have the radii of up to 2.3km. Hence, there is a need to propose a model that can evaluate the V_θ profile of different r_o radii at less than 10m AGL.

5.2. Conclusions

In investigating the $V_{\theta,max}$ of tornados for different r_o radii, and also the $V_{\theta,max}$ at z=3.3m, the following conclusions are made:

1. **Max. V vertical location z_{max} is always in the range of 21m to 64m AGL**

It was observed that for different radii, always 21m<z_{max}<64m, whereas the radar measurements show that 30m<z_{max}<200m.

Also, the vertical V_θ profile of tornados resembles a conical shape where the maximum occurs on the nose-like peak of the cone, as shown in Figure 5.1. This conical shape distinguishes tornadic flows from SL flows.

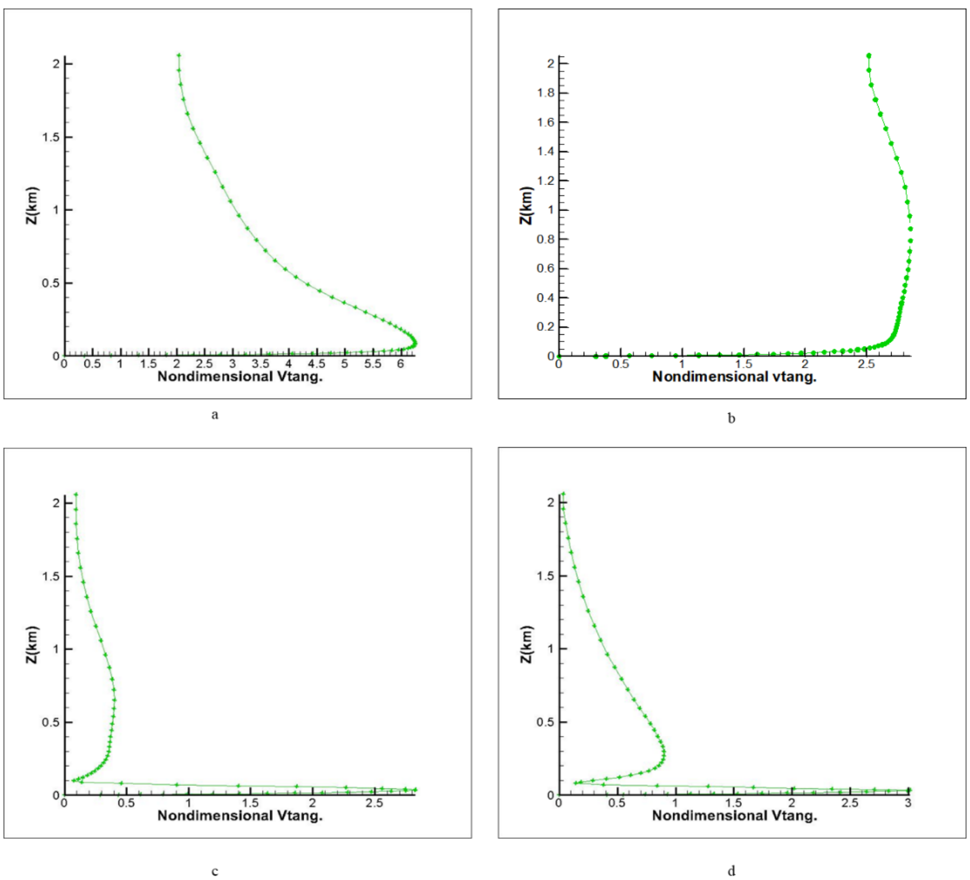

Figure 5.1. Vertical V_θ profile of tornados. a) 13m away of the tornado center for r_o=0.8km; b) 13m away of the tornado center for r_o=1.0km; c) 88m away of the tornado center for r_o=1.5km; d) 150m away of the tornado center for r_o=2.0km

2. **Increasing the r_o increases the z_{max}**

By increasing the r_o from r_o=0.7km to 1.9km, the z_{max} will also increase from 21m to 57m. However, for $r_o \geq 2.0$km, the z_{max} is constant at 64m.

3. **For $r_o \leq 1.6$km the radial V_θ profiles above 10m of the ground resemble the RCVM profile for different S values, whereas at less than 10m of the ground the profile has two peaks for S greater than the touchdown S**

Simulations show that for $r_o \leq 1.6$km, regardless of increasing the S value, the V_θ profiles at z>10 always resemble the RCVM profile, whereas at z<10m AGL, the radial V_θ profile has two peaks for the S value greater than the touchdown S. Figures 5.2(a), 5.2(b), 5.3(a) and 5.3(b) shows this observation.

4. **For $r_o \geq 1.8$km the radial V_θ profiles below and above z=10m have two peaks for the S greater than the touchdown S**

For $r_o \geq 1.8$km the radial V_θ profiles resemble the RCVM for S smaller than the touchdown S; whereas for S greater than the touchdown S, the profiles no longer resemble the RCVM flow, rather two peaks occur on the profile. Figures 5.2 and 5.3, respectively, show the radial V_θ profiles at z=9.5m and z=5.1m for different ro. It can be seen that for r_o=2.0km, the radial V_θ profiles always have two peaks, whereas for r_o=0.8km and 1.5km the profiles the two peaks occur only at z<10m AGL. Figures 5.2(c), 5.2(d), 5.3(c) and 5.3(d) shows this observation.

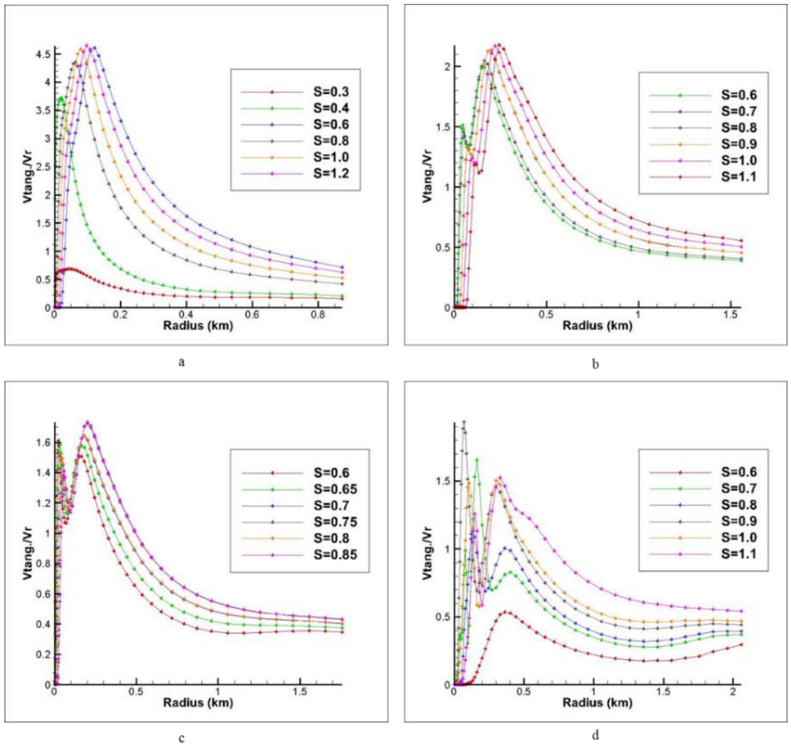

Figure 5.2. Radial V_θ profile at z=9.5m AGL. a) r_o=0.8km; b) r_o=1.5km; c) r_o=1.7km; d) r_o=2.0km

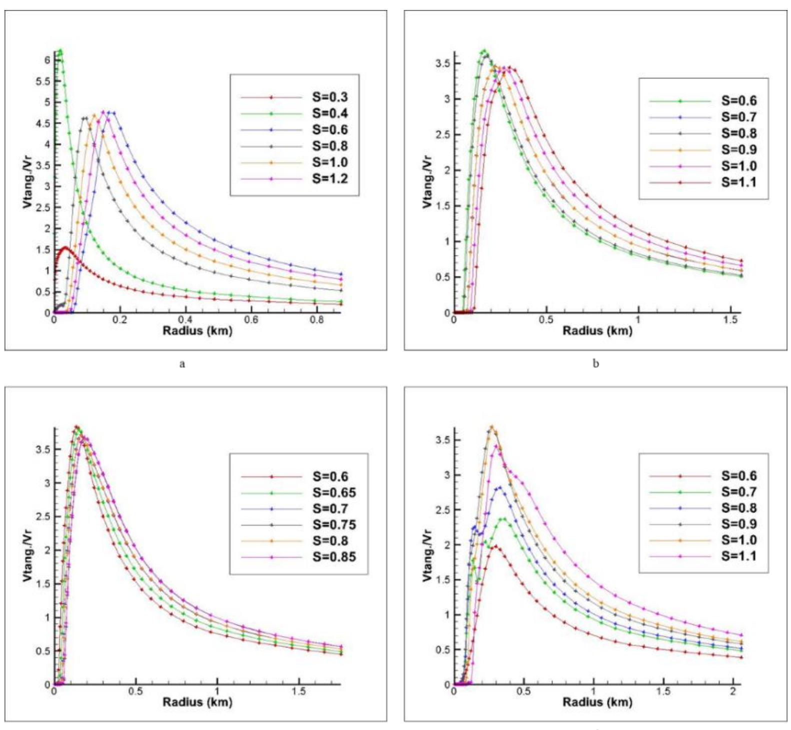

Figure 5.3. Radial V_θ profile at z=51m AGL. a) r_o=0.8km; b) r_o=1.5km; c) r_o=1.7km; d) r_o=2.0km

5. Increasing the r_o reduces the $V_{\theta,max}/V_{r\infty}$

Investigating the $V_{\theta,max}$ at different elevations above and below 10m shows that an increase of r_o causes the $V_{\theta,max}/V_{r\infty}$ to decrease.

5.3. Suggestions for future work

This study, despite being the first to measure the absolute $V_{\theta,max}$, z_{max}, r_c and $V_{\theta,max}$ at z=3.3m of different tornado radii, has some limits. Based on the limitation of the present study, the future paths of work are suggested as follows:

1. Investigation of the $V_{\theta,max}$ for different tornado radii with constant AR.

In the present study swirl ratio was considered as $S=V_\theta/(2(AR)V_{r\infty})$. Reorganizing this yields $V_\theta=2(AR)(V_{r\infty})(S)$. Since $AR=H_o/r_o$, it can be implied that H_o is directly proportional to the V_θ, and thus it is a significant factor in determining the tornado intensity. However, in the present study, H_o was constant and equal to 1000m, and $0.7km \leq ro \leq 2.3km$. Hence, the study was conducted for varying AR. Future studies can use variable H_o in order to have constant AR.

2. Using refined grids to investigate the triple-celled structures

In the present study, the double-cell tornados were observed in the simulations. However, although it is expected that by increase of the S parameter a triple-cell tornado occurs, there is not such observation in the present study, which is due to insufficient MGS away from the ground. In fact, the triple-cell tornados require extremely small scale modeling in the computation, whereas the present study used $MGS=0.001H_o$ with a growing factor of 1.1. Further refinement at this moment is impossible due to the storage limits in the computer modeling. Future studies can use higher grid resolutions to capture these small scale features.

3. Using a different computational domain

In the present study, the computational domain of Lewellen et al. (1997) was used and the boundary conditions were taken from Wilson and Rotunno (1986). However, other computational domains with different boundary conditions can simulated and compared to the present study. In this regard, the computational model of Ishihara et al. (2012) is an alternative computational domain which can be used for this purpose. Figures 2.15 and 2.16, respectively, show the schematics of the computational domains of the present study and Ishihara et al. (2012). The difference between these two computational domains has not been studied before.

REFERENCES

Abbey, R.F., and Fujita, T.T (1975). Use of tornado path lengths and gradations of damage to assess tornado intensity probabilities. Preprints, Ninth Conference on Severe Local Storms, Norman, OK, American Meteorological Society.

Ahmed, S.N., and Selvam, R.P. (2015). Ridge effects on tornado path deviation. International Journal of Civil and Structural Engineering Research.

Alrasheedi, N.H. (2012). Computer modeling of the influence of structure plan areas on tornado forces. PhD dissertation, University of Arkansas, Fayetteville, USA.

Allaby, M. (1997). Tornadoes. New York: Facts On File.

Aly, A.M., Bitsuamlak, G., Chowdhury, A.G. (2011). Florida International University's Wall of Wind: A Tool for Improving Construction Materials and Methods for Hurricane-Prone Regions. Vulnerability, Uncertainty, and Risk: Analysis, Modeling, and Management.

Afgan, I., Moulinec, C., Prosser, R., Laurence, D. (2007). Large Eddy simulation of turbulent flow for wall mounted cantilever cylinders of AR 6 and 10. International Journal of Heat and Fluid Flow, 2007.

Ahmed, N. (2015). Field Observations and Computer Modeling of Tornado-Terrain Interaction and Its Effects on Tornado Damage and Path. PhD dissertation, University of Arkansas, USA.

Alexander, C.R., Wurman, J. (2004). The 30 May 1998 Spencer, South Dakota, Strom. Prat I: The Structure Evolution and Environment of The Tornadoes, Journal of Monthly Weather Review.

Alrasheedi, N. (2015). Computer modeling of the influence of structure plan areas on tornado forces, PhD dissertation, University of Arkansas, USA.

Atkins, N., Butler, K.M., Flynn, K.R., Wakimoto, R.M. (2014). An integrated damage, visual, and Radar analysis of the 2013 Moore Oklahoma EF5 Tornado. Bulletin of the American Meteorological Society.

Baker, G.L, Church, C.R. (1979). Measurements of core radii and peak velocities in modeled atmospheric vortices. Journal of the Atmospheric Sciences.

Balaramudu, V. K. (2007). Tornado-induced wind loads on a low-rise building, Master's thesis, Aerospace department, Iowa State University, USA.

Barhaghi, D. G., and Davidson, L. (2003). Large Eddy simulation of a natural convection boundary layer on a vertical cylinder. Progress report, Department of Thermo and Fluid dynamics, Chalmers University of Technology, Sweden.

Bienkiewicz B, Dudhia, P. (1993). Physical modeling of tornado-like flow and tornado effects on building loading. Proceeding of 7th US National Conference on Wind Engineering.

Bitsuamlak, G. (2017). CFD applications in Wind Engineering. 13th Americas Conference on Wind Engineering Gainesville, Florida, USA, 2017.

Bluestein, H.B and Pazmany, A.L. (2000). Observations of tornadoes and other convective phenomena with a mobile, 3-mm wavelength, Doppler radar: The spring 1999 field experiment. Bulletin of American Meteorology Society.

Bluestein, H.B and Pazmany, A.L. (2004). The Vertical Structure of a Tornado near Happy, Texas, on 5 May 2002: High-Resolution, Mobile, W-band, Doppler Radar Observations. Journal of Monthly Weather Review.

Bluestein, H.B., Snyder, J.C. and Houser, J.B. (2015). A Multiscale Overview of the El Reno, Oklahoma, Tornadic Supercell of 31 May 2013. Weather Forecasting Journal.

Brooks, H. E. (2004). On the relationship of tornado path length and width to the intensity. Journal of Weather and Forecasting.

Catastrophes: U.S. (2014). Retrieved December 21, 2014, from http://www.iii.org/fact-statistic/catastrophes-us.

Chang, C.C. (1966). First real man made tornado is generated in laboratory cage by space scientists at the catholic University of America. News item of PI of CUA, 1966.

Clarke, S., and Clarke, T. (2015). GIS and the Arkansas EF-4 Tornado of April 27, 2014. http://proceedings.esri.com/library/userconf/proc14/papers/1491_736.pdf, May 28, 2016.

Chmielewski, T. , Nowak, H, Walkowiak, K. (2008). Tornado near Opole– estimates of wind velocity and assessment of buildings performance.

Church, C.R., Snow, J.T. (1993). Laboratory models of tornadoes. Journal of the tornado: its structure, dynamics, prediction, and hazards.

Church, C. R., Snow, J.T., Agee, E.M. (1977). Tornado vortex simulation at Purdue university. Bulletin American Meteorological Society.

Church, C.R., Snow, J.T., Baker, G.L., Agee, E.M. (1979). Characteristics of tornado-like vortices as a function of swirl ratio: a laboratory investigation. Journal of the Atmospheric Sciences.

Davies-Jones, R.P. (1973). The Dependence of Core Radius on Swirl Ratio in a Tornado Simulator. Journal of the Atmospheric Sciences.

Davies-Jones, R.P. (1976). Laboratory simulations of models. Assessment of knowledge and implications from man: proceedings of the Symposium on tornadoes, Texas Tech University, Lubbock, Texas, USA, 1976.

Diamond C.J., Wilkins, E.M. (1984). Translation Effects on Simulated Tornadoes, Journal of the Atmospheric Sciences.

Dominguez, D., Selvam, R.P. (2017). Close to ground wind-field in a vortex chamber using CFD. The 13th Americas Conference on Wind Engineering (13ACWE) Gainesville, Florida USA, 2017.

Domiguez, D., R. P. Selvam (2016). Tornado width for computer modeling from Google Earth data and period of the vortex. Oklahoma Conference, 2017.

Doswell, C. A. Brooks, H. E., Dotzek, N. (2009). On the implementation of the enhanced Fujita scale in the USA. Journal of Atmospheric Research.

Doswell, Ch. (1985). The Operational Meteorology of Convective Weather, Volume Ii: Storm Scale Analysis. NOAA Technical Memorandum.

Dutta, P. K., Ghosh, A. K., and Agarwal, B. L. (2002). Dynamic response of structures subjected to tornado loads by FEM. Journal of Wind Engineering and Industrial Aerodynamics.

Elikashvili, A., Gedalin, M., and Golbraikh, E. (2017). The initial vortex aloft and helical structure near the surface. Journal of Physics of Fluids.

Filippone, A., Afgan, I. (2008). Orthogonal blade-vortex interaction on a helicopter tail rotor, Journal of American Institute of Aeronautics and Astronautics.

Fujita, T.T., Bradbury, D.L. and Black, P.G. (1967). Estimation of tornado wind speed from characteristic ground marks. University of Chicago, USA.

Fujita, T.T. (1971). Proposed characterization of tornadoes and Hurricanes by area and intensity. University of Chicago: Research Project.

Fujita. T.T. Pearson, A. D. (1973). Results of FPP classification of 1971 and 1972 tornadoes. Preprints, Eighth Conference on Severe Local Storms, Denver, CO, American Meteorological Society.

Gallus, W. A., Haan, F. L., Sarkar, P., Le, K., Wurman, J. (2006). Comparison of numerical model and laboratory simulator tornado wind fields with radar observations of the Spencer, South Dakota tornado. In Symposium on the Challenges of Severe Convective Storms, 86th AMS Annual Meeting, Atlanta, GA, 2006. American Meteorological Society.

Grazulis, T.P. (1993). A 110-year perspective of significant tornadoes. In C. Church et al. (Eds.), The Tornado: its structure, dynamics, prediction, and hazard. Washington D.C.

Haan, F.L., Sarkar, P. (2017). An investigation of translation and static pressure effects on tornado-induced peak pressures on low-rise buildings using the DesignSafe cyberinfrastructure, 13th Americas Conference on Wind Engineering Gainesville, Florida, USA, 2017.

Haan, F.L., Sarkar, P., Balaramadu, V., Zhang, W. (2008). Non-stationary tornado-induced wind loads compared with traditional boundary layer wind loads on low-rise buildings. BBAA VI International Colloquium on: Bluff Bodies Aerodynamics & Applications Milano, Italy, 2008.

Haan, F.L., Sarkar, P., Gallus, W. (2008). Design, construction and performance of a large tornado simulator for wind engineering applications. Journal of Engineering Structures.

Haan, F.L., Jr., Balaramudu, V.K., Sarkar, P. (2010). Tornado-Induced Wind Loads on a Low-Rise Building. ASCE Journal of Structural Engineering.

Haan, F.L., Sarkar, P., Gallus, W.A. (2007). Design, construction and performance of a large tornado simulator for wind engineering applications. Eng. Structures Journal.

Hangan, H., and Kim, J.D. (2006). Numerical simulation of tornado vortices. The fourth symposium on Computational Wind Engineering (CWE2006), Yokohama, 2006.

Hangan, H., and Kim, J. D. (2008). Swirl ratio effects on tornado vortices in relation to the Fujita scale. Journal of Wind and Structures.

Harlow, F.H., and Welch, J.E. (1965). Numerical calculation of time-dependent viscous incompressible flow of fluid with free surface. Journal of The physics of Fluids.

He, M., Lam, F., Foschi, R.O. (2001). Modeling three-dimensional timber light-frame buildings, Journal of Structural Engineering.

Hirt C. W., Nichols, B.D., Romero, N.C. (1975). SOLA: A numerical solution algorithm for transient fluid flows. NASA STI/Recon Technical Report N, 75, 32418, 1975.

Hoecker, W.H. (1960).Wind speed and air flow patterns in the Dallas tornado of April 2, 1957. Journal of Monthly Weather Review.

Houston, A., Wilhelmson, R. (2006). Observational Analysis of the 27 May 1997 Central Texas Tornadic Event. Part I: Prestorm Environment and Storm Maintenance/Propagation. Journal of Monthly Weather Review.

Ishihara, T., Oh, S. and Tokuyama, Y. (2011). Numerical study on flow fields of tornado-like vortices using the LES turbulence model. Journal of Wind Engineering and Industrial Aerodynamics.

Ishihara, T., and Liu, Z. (2014). Numerical study on dynamics of a tornado-like vortex with touching down by using the LES turbulent model. Journal of Wind and Structures.

Jedlovec, G.J., Nair, U., Haines, S. L. (2006). Detection of storm damage tracks with EOS data. Journal of Weather and Forecasting.

Jischke, M.C. and Light, B.D. (1979). Laboratory simulation of tornadic wind loads on a cylindrical structure. Sixth International Conference on Wind Engineering.

Jischke, M.C., and Light, B.D. (1983). Laboratory simulation of tornadic wind loads on a rectangular model structure. Journal of Wind Engineering and Industrial Aerodynamics.

Jischke, M.C., Parang, M. (1979). Properties of simulated tornado-like vortices. Journal of Atmospheric Sciences.

Karstens, C.D., Gallus, W.G., Lee, B.D., Finely, C.A. (2013). Analysis of Tornado-Induced Tree Fall Using Aerial Photography from the Joplin, Missouri, and Tuscaloosa–Birmingham, Alabama, Tornadoes of 2011. Journal of Applied Meteorology and Climatology.

Karstens, C.D., Samaras, T.M., Gallus, W.A., Finely, C.A., Lee, B.D. (2010). Analysis of near-surface wind flow in close proximity to tornadoes.

Kasal, B., Leichti, R. (1992). Nonlinear Finite-Element Model for Light-Frame Stud Walls, Journal of Structural Engineering.

Kilty, K. (2005). Steady-state tornado vortex models.

Kim, J., Hangan, H. (2007). Numerical simulations of impinging jets with application to downbursts. Journal of Wind Engineering and Industrial Aerodynamics.

Klimowski, B.A., Hjelmfelt, M.R., Bunkers, M.J., Sedlacek, D. and Johnson, L.R. (1998). Hailstorm damage observed from the GOES-8 satellite: The 5–6 July 1996 Butte–Meade storm. Journal of Monthly Weather Review.

Kopp, G.A., Wu, C.H. (2017). A framework for the aerodynamics of low-rise buildings in tornadoes: Can boundary layer wind tunnels give us everything we need? The 13th Americas Conference on Wind Engineering (13ACWE) Gainesville, Florida USA, 2017.

Kopp, G.A., Morrison, M.J. (2016). Discussions and closures, Discussion of “Tornado-Induced Wind Loads on a Low-Rise Building” by F. L. Haan Jr., Vasanth Kumar Balaramudu, and P. P. Sarkar. Journal of Structural Engineering.

Kosiba, K., Wurman, J. (2010). Notes and correspondence, the Three-Dimensional Axisymmetric Wind Field Structure of the Spencer, South Dakota, 1998 Tornado. Journal of the Atmospheric Sciences.

Kosiba, K., Wurman, J. (2013). The Three-Dimensional Structure and Evolution of a Tornado Boundary Layer. Journal of Weather and Forecasting.

Kuai, L., Haan, F. L., Gallus, W.A., Sarkar, P. (2008). CFD simulations of the flow field of a laboratory-simulated tornado for parameter sensitivity studies and comparison with field measurements. Journal of Wind and Structures.

Kumar, N. (2008). Stress analysis of wood frames low rise buildings under wind loads due to tornados. Master’s thesis, Iowa State University, 2008.

Lee, W.C. (1999). Tropical Cyclone Kinematic Structure Retrieved from Single-Doppler Radar Observations. Part I: Interpretation of Doppler Velocity Patterns and the GBVTD Technique. Journal of Monthly Weather Review.

Lewellen, D.C., Gong, B., Lewellen, W.S. (2008). Effects of Finescale Debris on Near-Surface Tornado Dynamics. Journal of the Atmospheric Sciences.

Lewellen, W.S. (1976). Theoretical models of the tornado vortex. Journal of Assessment of Knowledge and Implications for Man: proceedings of the symposium on tornados, Texas Tech University, 1976.

Lewellen, W.S., Lewellen, D.C. (1997). Large Eddy simulation of a tornado’s interaction with the surface. Journal of the Atmospheric Sciences.

Lewellen, W.S., Lewellen, D.C., Sykes, R.I. (1997). Large-Eddy simulation of a tornado's interaction with the surface. Journal of the Atmospheric Sciences.

Lewellen, W.S. Lewellen, D.C., Xia, J. (2000). The Influence of a Local Swirl Ratio on Tornado Intensification near the Surface. Journal of the Atmospheric Sciences.

Lee, W.C., and Wurman, J. (2005). Diagnosed three-dimensional axisymmetric structure of the Mulhall Tornado on 3 May 1999. Journal of the Atmospheric Sciences.

Liu, X., and Marshall, J.S. (2004). Blade penetration into a vortex core with and without axial core flow. Journal of Fluid Mechanics.

Liu Z., Ishihara, T. (2015). A study of tornado induced mean aerodynamic forces on a gable-roofed building by the large eddy simulations Journal of Wind Engineering and Industrial Aerodynamics.

Liu, Z., Ishihara, T. (2015). Numerical study of turbulent flow fields and the similarity of tornado vortices using large-eddy simulations. Journal of Wind Engineering and Industrial Aerodynamics.

Liu, Z., Ishihara, T. (2012). Effects of the swirl ratio on the turbulent flow fields of tornadolike vortices by using LES turbulent model. The Seventh International Colloquium on Bluff Body Aerodynamics and Applications (BBAA7) Shanghai, China, 2012.

Liu, Z., Ishihara, T. (2013). LES modeling of the effects of ground roughness and translation on tornado-like vortices. The Eighth Asia-Pacific Conference on Wind Engineering, 2013, Chennai, India.

Liu, Z., Ishihara, T. (2016). Study of the effects of translation and roughness on tornado-like vortices by large-eddy simulations. Journal of Wind Engineering and Industrial Aerodynamics.

Liu, Z., Ishihara, T., He, X., Huawei, N. (2016). LES study on the turbulent flow fields over complex terrain covered by vegetation canopy. Journal of Wind Engineering and Industrial Aerodynamics.

Maruyama, T. (2009). A numerically generated tornado-like vortex by large eddy simulation. The Seventh Asia-Pacific Conference on Wind Engineering, 2009, Taipei, Taiwan.

Matsui, M., Tamura, Y. (2005). Characteristics of tornado-like flow as functions of swirl ratio and surface roughness. (Japanese).

Matsui, M., Tamura, Y. (2009). Influence of swirl ratio and incident flow conditions on generation of tornado-like vortex.

McCarthy, D. (2003). NWS tornado surveys and the impact on the national tornado database. NWS storm prediction center. The fifth EA Computational Wind Engineering, Florence, Italy, 2009.

McDonald, J.R., Forbes, G.S., Marshall, T. P. (2004). The Enhanced Fujita (EF) Scale. Texas Tech University.

McDonald, J.R., Selvam, R.P. (1985). Tornado forces on building using the boundary element method. Fifth U.S. National Conference on Wind Engineering, Texas Tech University, Lubbock, TX, USA.

Mishra A.R., James, D.L., Letchford, C.W. (2008). Physical simulation of a single-celled tornado-like vortex, Part A: Flow field characterization. Journal of Wind Engineering and Industrial Aerodynamics.

Mishra, A.R., James, D.L., Letchford, C.W. (2008). Physical simulation of a single-celled tornado-like vortex, Part B: Wind loading on a cubical model. Journal of Wind Engineering and Industrial Aerodynamics.

Mitsuta, Y., Monji, N. (1984). Development of a laboratory simulator for small scale atmospheric vortices. Journal of Natural Disaster Science.

Moller, A.R. (1979). The climatology and synoptic meteorology of southern plains' tornado outbreaks. Master's Thesis, University of of Oklahoma, Norman, OK.

Moller, A.R., Doswell, C., McGinley, J., Tegtmeier, S., Zipser, R. (1974). Field observations of the Union City tornado in Oklahoma. Weatherwise Journal.

Molthan, A.L., Bell, J.R., Cole, T.A., Burks, J.E. (2014). Satellite-based identification of tornado damage tracks from the 27 April 2011 severe weather outbreak. Journal of Operational Meteorology.

Monji, N. (1985). A laboratory investigation of the structure of multiple vortices. Journal of Meteorological Society of Japan.

Natarajan, D., Hangan H. (2009). Numerical study on the effects of surface roughness on tornado-like flows. 11th Americas conference on wind engineering, San Juan, Puerto Rico, 2009.

Natarajan, D., Hangan, H. (2012). Large Eddy simulations of translation and surface roughness effects on tornado-like vortices, Journal of Wind Engineering and Industrial Aerodynamics.

NOAA (2012). National Oceanic and Atmospheric Administration. Retrieved from www.noaa.gov.

Nolan, D.S. (2005). A new scaling for tornado-like vortices. Journal of the Atmospheric Sciences.

Nolan D.S. (2013). On the use of Doppler-radar-derived wind fields to diagnose the secondary circulation of tornadoes. Journal of the Atmospheric Sciences.

Nolan, D.S., Farrell, B.F. (1999), The Structure and Dynamics of Tornado-Like Vortices, Journal of the Atmospheric Sciences.

NWS (2011). Tuscaloosa-Birmingham Tornado. Retrieved from http://www.srh.noaa.gov/bmx/?n=event_04272011tuscbirm.

Neale, A., Derome, D., Blocken, B., Carmeliet, J. (2006). CFD calculation of convective heat transfer coefficients and validation–Part 2: Turbulent flow, 2006.

Ortega, K., Burgess, D., Garfield, G., Karstens, C., LaDue, J., Marshal, T., Meyer, T., Smith, B., Smith, R., Speheger, D., Stumpf, G. (2014). Damage Survey and Analysis of the 20 May 2013 Newcastle-Moore EF-5 Tornado.

Pham, V., Tsuyoshi, N., Kojiro, N., Hirotoshi, K. (2012). A numerical study of the effects of moving tornado-like vortex on a cube, The Seventh International Colloquium on Bluff Body Aerodynamics and Applications (BBAA7), Shanghai, China, 2012.

Phuc, P.V., Nozu, T., Nozawa, K., Kikuchi, H. (2012). A Numerical Study of the Effects of Moving Tornado-Like Vortex on a Cube. The Seventh International Colloquium on Bluff Body Aerodynamics and Applications (BBAA7) Shanghai, China, 2012.

Razavi, A., Sarkar, P. (2016). Laboratory investigation of the effect of tornado translation on its near-ground flow field. 8th International Colloquium on Bluff Body Aerodynamics and Applications Northeastern University, Boston, Massachusetts, USA, 2016.

Refan, M. (2014). Physical Simulation of Tornado-Like Vortices. PhD Thesis. Department of Mechanical and Materials Engineering, The university of Western Ontario.

Refan, M., Hangan, H. (2016). Characterization of tornado-like flow fields in a new model scale wind testing chamber. Journal of Wind Engineering and Industrial Aerodynamics.

Refan, M., Hangan, H., Wurman, J. (2014). Reproducing tornados in laboratory using proper scaling. Journal of Wind Engineering and Industrial Aerodynamics.

Refan, M., Hangan, H., Wurman, J., Kosiba, K. (2017). Doppler radar-derived wind field of five tornado events with application to engineering simulations.

Rotunno, R. (1977). Numerical simulation of a laboratory vortex. Journal of the Atmospheric Sciences.

Rotunno, R. (1979). A study in tornado-like vortex dynamics. Journal of the Atmospheric Sciences.

Roueche, D., Prevatt, D., Haan, F. , Datin, P. (2015). An estimate of tornado loads on a wood-frame building using database-assisted design methodology, Journal of Wind Engineering and Industrial Aerodynamics.

Sabareesh, G.R., Matsui, M., Yoshida, A., Tamura, Y. (2009). Pressure acting on a cubic model in boundary-layer and tornado-like flow fields. 11th Americas conference on wind engineering, San Juan, Puerto Rico, 2009.

Sarkar, P., Haan, F., Gallus, W., Le, J.K., Wurman, J. (2005). Velocity measurements in a laboratory tornado simulator and their comparison with numerical and full scale data. In: Proceedings of the 37th Joint Meeting Panel on Wind and Seismic Effects, Tsukuba, Japan, 2005.

Selvam, R.P. (1992). Computation of pressures on Texas Tech building. Journal of Wind Engineering and Industrial Aerodynamics.

Selvam, R.P. (1993). Computer modeling of tornado forces on buildings. 7th US National Conference on Wind Engineering, Los Angeles, CA.

Selvam, R.P. (1997). Computation of pressure on Texas Tech University Building using large eddy simulation. Journal of wind Engineering and Industrial Aerodynamics.

Selvam, R.P., and Millett, P.C. (2003). Computer modeling of tornado forces on buildings. Journal of Wind and Structures.

Selvam, R.P., and Millet, P.C. (2002). Computer modeling of the tornado structure interaction: investigation of structural loading on cubic building. In K. Kumar (Ed), Wind Engineering (pp. 895-902). New Delhi, India: Phoenix Publishing House.

Selvam, R.P., and Millett, P.C. (2005). Large eddy simulation of the tornado-structure interaction to determine structural loadings. Wind and Structures, 8, 49-60.

Selvam, R.P., and Gorecki, P. (2012). Effect of tornado size on forces on thin 2D cylinder. 3rd American Association for Wind Engineering Workshop Hyannis, Massachusetts, USA, 2012.

Selvam, R.P., Ragan, Q.S. (2012). Mitigation of tornado effects-a study of the shielding effects of hills. 3rd American Association for Wind Engineering Workshop, Hyannis, Massachusetts, USA.

Selvam, R.P., Roy, U.K., Jung, Y., Mehta, K.C. (2002). Investigation of tornado forces on a 2D cylinder using computer modeling. In K. Kumar (Ed), Wind Engineering, New Delhi, India: Phoenix Publishing House.

Sengupta, A., Haan, F.L., Sarkar, P., Balaramodu, V. (2008). Transient loads on buildings in microburst and tornado winds. Journal of Wind Engineering and Industrial Aerodynamics.

Sengupta, A., Sarkar, P. (2006). Physical and numerical simulation of microburst-like wind: a study of flow characteristics and surface pressures on a cube. In: Proceedings of Third Indian National Conference on Wind Engineering, Kolkata, India.

Smith D.R. (1987). Effect of boundary conditions on numerically simulated tornado-like vortices. Journal of the Atmospheric Sciences.

Snow, J.T., Lund, D.E. (1988). A second generation tornado vortex chamber at Purdue University, in Prepints, 15th conference on Severe local storms. American Meteorological Society, Boston, Massachusetts, USA.

Stein, L.R., Harlow, F.H. (1974). Numerical solution of the flow structure in tornado-like vortices. Los Alamos scientific laboratory of the University of California, USA.

Strasser, M. (2015). The aerodynamic and dynamic loading of a slender structure by an impacting tornado-like vortex: the influence of relative vortex-to-structure size on structural loading. PhD dissertation, University of Arkansas, USA.

Strasser, M., Selvam, R.P. (2015). Selection of a realistic viscous vortex tangential velocity profile for computer simulation of vortex-structure interaction. Journal of the Arkansas Academy of Science.

Strasser, M., Yousef, M., Selvam, R.P. (2016). Defining the vortex loading period and application to assess dynamic amplification of tornado-like wind loading. Journal of Fluids and Structures.

Strong, C.A., and Zubrick, S.M. (2004). Overview and synoptic assessment of the 28 April 2002 La Plata, MD tornado. Pre-prints, 22nd Conference on Severe Local Storms, Hyannis, MA, American Meteorological Society.

Sun, Y., Tamura, Y., Quan, Y., Matsui, M., Xu, S. (2008). The interference effect of surrounding buildings on wind loads of low-rise buildings. BBAA VI International Colloquium on: Bluff Bodies Aerodynamics & Applications, Milano, Italy, 2008.

Tang, Z., Feng, C.,Wu, L., Zuo, D., James, D. (2016). Simulations of tornado-like vortices in a large-scale Ward-type tornado simulator. 8th International Colloquium on Bluff Body Aerodynamics and Applications Northeastern University, Boston, Massachusetts, USA, 2016.

Tang, Z., Wu, L., Feng, C., Zuo, D., James, D. (2017). Effects of aspect ratio on tornado-like vortices simulated in a large-scale tornado simulator. The 13th Americas Conference on Wind Engineering (13ACWE) Gainesville, Florida USA, 2017.

Tao Tao, Tamura, T., Kawai, H. (2017). WRF Simulation of Strong Wind Gust Induced by Tornado-genesis Storm. The 13th Americas Conference on Wind Engineering (13ACWE) Gainesville, Florida USA, 2017.

Tapia, X.P. (2009). Modelling of wind flow over complex terrain using OpenFoam. Master's thesis. Department of Technology and Built Environment, University of Gavle, Sweden.

Tari, P.H., Gurka, R., Hangan, H. (2010). Experimental investigation of tornado-like vortex dynamics with swirl ratio: The mean and turbulent flow fields. Journal of Wind Engineering and Industrial Aerodynamics.

Tecson, J.J., Fujita, T.T., Abbey, R.F. (1979). Statistics of U.S. tornadoes based on the DAPPLE (Damage Area Per Path LEngth) tornado tape. Preprints, Eleventh Conference on Severe Local Storms, Kansas City, MO, American Meteorological Society.

Thampi, H., Dayal, V. and Sarkar, P.P. (2011). Finite element analysis of interaction of tornados with a low-rise timber building. Journal of Wind Engineering and Industrial Aerodynamics.

Thampi, H., Dayal, V., and Sarkar, P.P. (2010). Finite element modeling of interaction of tornado with a low-rise timber building. Fifth International Symposium on Computational Wind Engineering, Chapel Hill, North Carolina, USA.

Varistas G.H. (1989). Analysis of fine particle concentrations in a confined vortex. Journal of Hydraulic Research.

Varistas G.H. (1991). A simpler model for concentrated vortices. Journal of Experiments in Fluids.

Wakimoto, R.M., Atkins, N.T., Butler, K.M., Bluestein, H.B., Thiem, K., Synder, J.C., Houser, J., Kosiba, K, Wurman, J. (2016). Aerial damage survey of the 2013 El Reno tornado combined with mobile radar data. American Meteorological Society.

Wakimoto, R.M., Atkins, N.T., Butler, K.M. (2015). Photogrammetric analysis of the 2013 El Reno tornado combined with Mobile X-Band Polarimetric Radar Data. Journal of Monthly Weather Review.

Wakimoto, R.M., Atkins, N., Wurman, J. (2011). The LaGrange Tornado during VORTEX2. Part I: Photogrammetric Analysis of the Tornado Combined with Single-Doppler Radar Data. Journal of Monthly Weather Review

Wakimoto, R.M., Stauffer, P., Lee, W.C. (2012). Finescale structure of the LaGrange, Wyoming, Tornado during VORTEX2: GBVTD and Photogrammetric Analyses. Journal of Monthly Weather Review.

Wang, H. (2002). Fluid-structure interaction of a tornado-like vortex with low-rise structures. Master's thesis, Texas Tech University.

Ward, N.B. (1972). The exploration of certain features of tornado dynamics using a laboratory model. Journal of the Atmospheric Sciences.

Wen, Y. (1975). Dynamic tornadic wind loads on tall buildings. Journal of the Structural Division, 101, 169-185.

Wilson, T. (1977). Tornado structure interaction: a numerical simulation, Report: UCRL-52207, Distribution Category: UC-11, 80, Lawrence Livermore Laboratory, University of California, Livermore.

Walter H., Hoecker, J.R. (1960). Wind speed and air flow patterns in the Dallas Tornado of April 2, 1957. Journal of Monthly Weather Review.

Whipple, A.B. (1982). Storm. New York: Time-Life Books.

Wilson, T., and Rotunno, R. (1986). Numerical simulation of a laminar end-wall vortex and boundary layer. Journal of the Physics of Fluids.

Wood, V., and Brown, R.A. (2011). Simulated tornadic vortex signatures of tornado-like vortices having one-and double-celled structures. Journal of Applied Meteorology and Climatology.

Wurman, J. (2002). The multiple vortex structure of a tornado. Journal of Weather and Forecasting.

Wurman, J., Alexander, C.R. (2005). The 30 May 1998 Spencer, South Dakota, Storm. Part II: Comparison of observed damage and radar-derived winds in the tornadoes. Journal of Monthly Weather Review.

Wurman, J., Alexander, C.R., Robinson, P., Richardson, Y. (2007). Low-level winds in tornadoes and potential catastrophic tornado impacts in urban areas. American meteorological society.

Wurman, J., and Gill, S. (2000). Finescale radar observations of the Dimmitt, Texas (2 June 1995), Tornado. Journal of Monthly Weather Review.

Wurman, J., Straka, J. (1997). Notes and correspondence, design and deployment of a portable, pencil-beam, pulsed, 3-cm Doppler Radar. Journal of Atmospheric and Oceanic Technology.

Wurman, J., Straka, J.M., Rasmussen, E.N. (1996). Fine-scale Doppler radar observations of tornadoes. Journal of Science.

Wurman, J., Kosiba, K., Robinson, P. (2013). In situ, Doppler radar and video observations of the interior structure of a tornado and the wind-damage relationship. Bulletin of the American Meteorological Society.

Wurman, J., Kosiba, K., Robinson, P., Marshal, T. (2013). The role of multiple-vortex tornado structure in causing storm researcher fatalities. American meteorological society.

Xu, Z., Hangan, H. (2009). An inviscid solution for modeling of tornado-like vortices. ASME Journal of Mechanics.

Yang, Z., Sarkar, P.P., Hu, H. (2011). An experimental study of a high-rise building model in tornado-like winds. Journal of Fluid and Structures.

Yuan, F., Yan, G., Honerkamp, R., Isaac, K.M. (2017). Modelling translating tornado-like wind flow using CFD simulations, The 13th Americas Conference on Wind Engineering (13ACWE) Gainesville, Florida USA, 2017.

Yousef, M. (2017). A comparison of force and pressure coefficients on Dome, Cubic and Prism shaped buildings due to straight and tornadic wind using three dimensional computational fluids dynamic model for different tornado translational speeds. PhD dissertation, University of Arkansas, USA.

Zhang, W., and Sarkar, P.P. (2012). Near-ground tornado-like vortex structure resolved by Particle Image Velocimetry (PIV). Journal of Experiments in Fluids.

Zhao, Y., Yan, G., Feng, R. (2017). Improvement of tornado simulation by adjusting boundary conditions. The 13th Americas Conference on Wind Engineering (13ACWE) Gainesville, Florida USA, 2017.

Zhou, Q., Cao, S., Liao, H., Li, M., Huang, G. (2016). Experimental study on the flow structures of tornado-like vortices with different swirl ratios. The 2016 world congress on advances in civil, environmental, and materials research (ACEM16), Korea, 2016.